# On the coupling between lower and upper atmosphere of the Sun

A thesis
submitted for the degree of

**Doctor of Philosophy**

in

The Department of Physics,
Pondicherry University,
Puducherry - 605 014, India

by

**Tanmoy Samanta**
Indian Institute of Astrophysics,
Bangalore - 560 034, India

January 2017

# On the coupling between lower and upper atmosphere of the Sun

Tanmoy Samanta
*Indian Institute of Astrophysics*

Indian Institute of Astrophysics
Bangalore - 560 034, India

Title of the thesis : **On the coupling between lower and upper atmosphere of the Sun**

Name of the author : **Tanmoy Samanta**
Address : Indian Institute of Astrophysics
II Block, Koramangala
Bangalore - 560 034, India
Email : tsamanta@iiap.res.in

Name of the supervisor : **Prof. Dipankar Banerjee**
Address : Indian Institute of Astrophysics
II Block, Koramangala
Bangalore - 560 034, India
Email : dipu@iiap.res.in

# Declaration of Authorship

I hereby declare that the matter contained in this thesis is the result of the investigations carried out by me at the Indian Institute of Astrophysics, Bangalore, under the supervision of Prof. Dipankar Banerjee. This work has not been submitted for the award of any other degree, diploma, associateship, fellowship, etc. of any other university or institute.

Signed:

Date:

# Certificate

This is to certify that the thesis entitled **'On the coupling between lower and upper atmosphere of the Sun'** submitted to the Pondicherry University by Mr. Tanmoy Samanta for the award of the degree of Doctor of Philosophy, is based on the results of the investigations carried out by him under my supervision and guidance, at the Indian Institute of Astrophysics. This thesis has not been submitted for the award of any other degree, diploma, associateship, fellowship, etc. of any other university or institute.

Signed: ____________________________________________

Date: ____________________________________________

# List of Publications

1. **Samanta, T.**, Banerjee, D., Tian, H., 2015, "Quasi-periodic oscillation of a coronal bright point", *The Astrophysical Journal*, 806, 172
2. **Samanta, T.**, Pant, V., Banerjee, D., 2015, "Propagating disturbances in the solar corona and spicular connection", *The Astrophysical Journal Letters*, 815, L16
3. **Samanta, T.**, Henriques, V. M. J., Banerjee, D., Krishna Prasad, S., Mathioudakis, M., Jess, D., Pant, V., 2016, "The effects of transients on photospheric and chromospheric power distributions", *The Astrophysical Journal*, 828, 23
4. **Samanta, T.**, Singh, J., Sindhuja, G., Banerjee, D., 2016, "Detection of high-frequency oscillations and damping from multi-slit spectroscopic observations of the corona", *Solar Physics*, 291, 155
5. **Samanta, T.**, Tian, H., Banerjee, D., Schanche, N., 2017, "Dynamics of subarcsecond bright dots in the transition region above sunspots and their relation to penumbral micro-jets", *The Astrophysical Journal Letters*, 835, L19
6. Mandal, S., **Samanta, T.**, Banerjee, D., Krishna Prasad, S., Teriaca, L., 2015, "Propagating disturbances along fan-like coronal loops in an active region", *Research in Astronomy and Astrophysics*, 15, 1832
7. Mandal, S., Hegde, M., **Samanta, T.**, Hazra, G., Banerjee, D., Ravindra, B., 2017, "Kodaikanal digitized white-light data archive [1921-2011]: Analysis of various solar cycle features", *Astronomy & Astrophysics*, Accepted for publication, arXiv:1608.04665

# Presentations

1. Oral presentation in the *IRIS-6: The Chromosphere meeting* held at the Stockholm University, Stockholm, Sweden, during 20-23 June 2016.
2. Oral presentation in the *IBUKS meeting* held at the KU Leuven, Belgium, during 13-19 June 2016.
3. Oral presentation in the *Dynamic Sun I: MHD Waves and Confined Transients in the Magnetised Atmosphere* held at the Indian Institute of Technology, Varanasi, India, during 22-26 February 2016.
4. Oral presentation in the *3rd Asia-Pacific Solar Physics Meeting* held at the Seoul National University, Seoul, South Korea, during 3-6 November 2015.
5. Oral presentation in the *Astronomical Society of India meeting 2016 (ASI:2016)* held at the Kashmir University, Kashmir, India, during 5-10 May 2016.
6. Poster presentation in the *Hinode-10 meeting* held at the Nagoya University, Nagoya, Japan, during 5-9 September 2016.
7. Poster presentation in the *Hinode-9 meeting* held at the Queens University, Belfast, Northern Ireland, UK, during 10-14 November 2015.
8. Poster presentation in the international conference on the *Coupling and Dynamics of the Solar Atmosphere* held at the IUCAA, Pune, India, during 10-14 November 2014.
9. Poster presentation in the *India-UK Seminar on Plasma Processes in the Solar and Space Plasma at Diverse Spatio-temporal Scales* held at the ARIES, Nainital, India, during 26-28 March 2014.
10. Poster presentation in the *Astronomical Society of India meeting 2013 (ASI:2013)* held at Thiruvananthapuram, Kerala, India, during 20-22 February 2013.
11. Poster presentation in the *Astronomical Society of India meeting 2014 (ASI:2014)* held at the IISER, Mohali, India, during 20-22 March 2014.
12. Poster presentation in the *Astronomical Society of India meeting 2015 (ASI:2015)* held at the NCRA, Pune, India, during 17-20 February 2015.

# *Acknowledgements*

Completion of this doctoral dissertation was possible with the support of several people. I would like to express my sincere gratitude to all of them. First of all, I would like to thank Dipu da, my supervisor, for his guidance, constant encouragement and unconditional support during my PhD. It was all my pleasure to work with him.

I am thankful to IIA for providing me an excellent academic environment and the necessary facilities for my research work during my tenure. I wish to express my thanks to all the IIA members for their help.

I would like to thank all of my collaborators for their valuable guidance and encouragement. I would also like to thank Dipu da's research group members including my seniors for their valuable input in the research and kind support.

I would like to thank my doctoral committee members and the staff at the Pondicherry University for their timely help and relevant suggestions.

My special thanks to Vaibhav and Sudip for reading the proof of my thesis and providing valuable suggestions.

I also thank all my friends and fellow students at the IIA for their constant support and encouragement.

In the last, I would like to thank my parents, my sister, my extended family and my teachers for being a continuous source of support for pursuing a research career.

# *Data usage*

Data from various space and ground-based facilities are used in the studies presented in the thesis. I duly acknowledge the usage of the data from these facilities, and I thank the respective instrument team members for providing the data in the public domain.

SDO Data supplied courtesy of the SDO/HMI and SDO/AIA consortia. SDO is the first mission to be launched for NASA's Living With a Star (LWS) Program.

IRIS is a NASA small explorer mission developed and operated by LMSAL with mission operations executed at NASA Ames Research center and major contributions to downlink communications funded by ESA and Norwegian Space Centre.

Hinode is a Japanese mission developed and launched by ISAS/JAXA, with NAOJ as domestic partner and NASA and STFC (UK) as international partners. It is operated by these agencies in co-operation with ESA and NSC (Norway).

The Swedish 1-m Solar Telescope (SST) is operated on the island of La Palma by the Institute for Solar Physics (ISP) of Stockholm University in the Spanish Observatorio del Roque de los Muchachos of the Instituto de Astrofsica de Canarias.

I like to thank Prof. Jagdev Singh and his team for conducting the multi-slit experiment (supported by IIA) at the Easter Island. I would like to thank them all for providing me the data and helping me with the data analysis. My special thanks to Prof. Jagdev Singh for his guidance and providing me valuable insights during the data analysis process. I like to thank V. Natarajan for his help in making the schematic diagram of the optical layout of the experiment.

*Dedicated to*

*my*

*family and friends...*

# Abstract

The thesis is focused on the study of the small-scale transients and waves as seen in the different layers of the solar atmosphere and the coupling between the different layers. The unique high-resolution data obtained by the newly launched Interface Region Imaging Spectrograph (IRIS) is used to study the highly dynamic, less understood, chromosphere and transition region and their dynamical connection with the corona. The Atmospheric Imaging Assembly (AIA) images onboard the Solar Dynamics Observatory (SDO) cover a broad range of temperature in the corona. The Helioseismic and Magnetic Imager magnetogram (HMI) onboard the SDO has helped us to study the evolution of the magnetic field at the photosphere. The high-resolution data from the the Swedish 1-m Solar Telescope (SST) equipped with the CRISP Imaging SpectroPolarimeter is used to study the photosphere and the chromosphere. The chromospheric data obtained from the Solar Optical Telescope (SOT) onboard Hinode is also used. High spatial resolution, high time cadence, simultaneous imaging and spectroscopic coordinated observational data as recorded from these instruments are used to study the dynamics of different fine-structures, small-scale transients events and their responses in the different layers of the solar atmosphere. The interaction between magnetohydrodynamics (MHD) waves and inclined magnetic fields is explored in a quiet-Sun region. Small-scale transient like mottles, Rapid Blueshifted Excursions (RBEs), and Rapid Redshifted Excursions (RREs) in the chromosphere are studied and their coupling through the photosphere to upper chromosphere is also studied. Small-scale chromospheric and transition regions jets, e.g., Type I and Type II spicules, are ubiquitously found in the solar atmosphere. In this thesis we explored the connection between these jets and the dynamical changes observed in the coronal structures, e.g., coronal bright points and, coronal plumes. The fine-structure dynamics above the sunspot are also explored. The relation between the subarcsecond bright dots in the transition region and the micro-jets in the chromosphere are explored to find their formation mechanism. We have also studied the “high-frequency oscillations” in the coronal structure as observed during a total solar eclipse from the Easter Island, Chile. The characterization of these “high-frequency waves”, their importance in the coronal heating and the damping mechanisms are explored. Thus, through the dynamical study of various transients, the coupling between the different layers of the solar atmosphere is studied while using high spatial and temporal resolution data in multi wavelengths as recorded from different space based and ground based imaging and spectroscopic instruments.

# Contents

# List of Figures

# List of Tables

# Abbreviations

| | |
|---|---|
| **NASA** | **N**ational **A**eronautics and **S**pace **A**dministration |
| **SOHO** | **SO**lar and **H**eliospheric **O**bservatory |
| **EIT** | **E**xtreme ultraviolet **I**maging **T**elescope |
| **MDI** | **M**ichelson **D**oppler **I**mager |
| **TRACE** | **T**ransition **R**egion and **C**oronal **E**xplorer |
| **SOT** | **S**olar **O**ptical **T**elescope |
| **SST** | **S**wedish **S**olar **T**elescope |
| **CRISP** | **CR**isp **I**maging **S**pectro**P**olarimeter |
| **SDO** | **S**olar **D**ynamics **O**bservatory |
| **AIA** | **A**tmospheric **I**maging **A**ssembly |
| **HMI** | **H**elioseismic and **M**agnetic **I**mager |
| **IRIS** | **I**nterface **R**egion **I**maging **S**pectrograph |
| **DOT** | **D**utch **O**pen **T**elescope |
| **MHD** | **M**agneto**H**ydro**D**ynamics |
| **CCD** | **C**harge **C**oupled **D**evice |
| **EUV** | **E**xtreme **U**ltra**V**iolet |
| **UT** | **U**niversal **T**ime |
| **TR** | **T**ransition **R**egion |
| $\mathbf{R}_\odot$ | Solar **R**adius |

# Chapter 1

# Introduction

The Sun at the heart of our solar system is a very common star in our galaxy. It was born about 4.6 billion years ago from a giant rotating cloud of gas and dust. Though there are hundreds of billion of stars in our galaxy, the Sun is very special to us as it supplies the energy to sustain life on the Earth. It is also the most important astronomical object for humankind with solar activity driving the space weather and having profound effects on our climate and communications. Solar storms which carry vast amounts of magnetized plasma into space can disrupt satellite operations, telecommunications, electric power grids, oil-pipelines in high-latitude countries and air-traffic on polar routes. All these potential impacts indicate the importance of studying such activities and the energy transfer from the solar interior to the outer atmosphere and beyond.

The Sun is a self-luminous ball of hot gas which is powered by thermonuclear fusion in its core. The energy, generated at the core, gets transported upto 0.7 $R_\odot$ by the process of radiation and from there to the visible solar surface by the convection. These two layers of the Sun's interior are termed as the radiative zone and the convective zone. The names are given based on the energy transportation processes

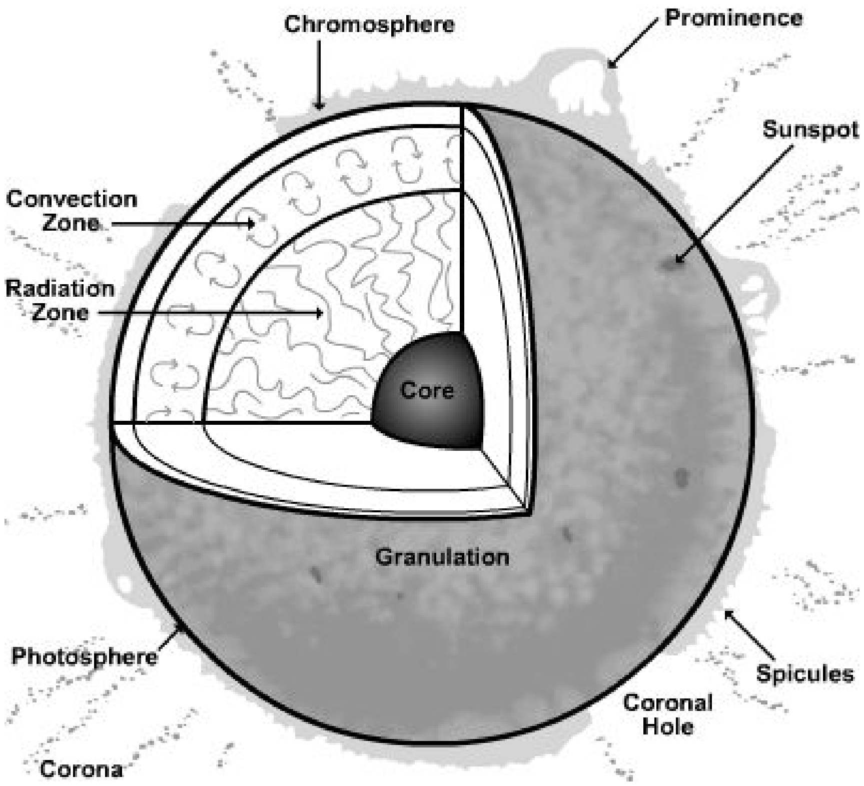

FIGURE 1.1: A schematic diagram showing the different layers of the Sun from the central core to outer corona. *Image credit:* `//http://yeslk.com/sun-structure-diagram/`

through these layers. The different layers of the Sun are shown in Figure 1.1. A brief description of the solar atmosphere is given below.

## 1.1 The Solar Atmosphere

The atmosphere of the Sun consists of hot plasma and extends over millions of kilometers from its surface. It is usually divided into different layers, starting from the photosphere at the bottom, moving up through the chromosphere and transition region (TR) to the corona. Different layers of the solar atmosphere are shown in the Figure 1.1. All these layers have different temperature, density and velocity structure. Though the temperature at the core of the Sun does

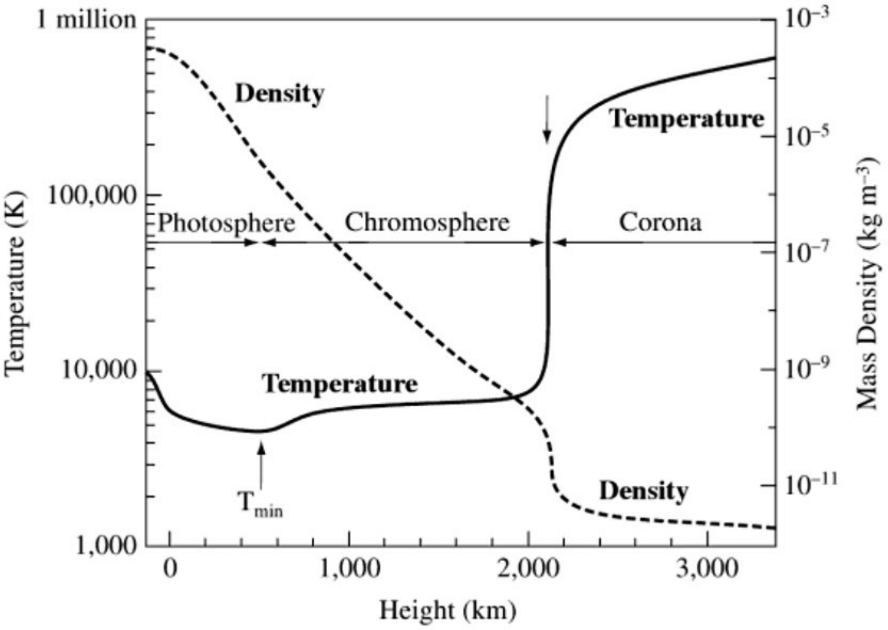

FIGURE 1.2: A schematic of the mean variation of temperature and density with height in the solar atmosphere. Reproduced from the VAL (Vernazza-Avrett-Loeset) solar atmospheric model. *Courtesy of* Eugene Avrett.

reach 14 million degrees, it drops to a mere 5700 degrees at the surface known as the photosphere. After that, the temperature decreases over a few hundred kilometers and reaches a minimum value. The temperature starts rising again through the chromosphere and then sharply increases to million of degrees in the corona through the thin TR layer. The temperature variation through these layers is shown in the Figure 1.2. Note the temperature variation shown here is derived from the VAL model (Vernazza *et al.* 1981) which shows a representative variation but the actual heights of these layers may vary in different regions and structures of the solar atmosphere. The rise of the temperature from the chromosphere to the corona is not generally expected and is known as the coronal heating problem. What causes this rapid increase in temperature is still one of the big mysteries. Soon after the discovery, theoreticians came up with reasonable mathematical models that tried to explain this apparently controversial feature. Popular theories which attempt to explain the coronal heating can be broadly grouped into two categories. One that demands a large number of magnetic reconnections and other, that argues the heating is dominated by the damping of magnetohydrodynamic

(MHD) waves. It is now recognized that the solar atmosphere is highly structured in the presence of magnetic fields and it is likely that different heating mechanisms may operate in different solar atmospheric structures. It is also possible that different heating mechanisms work simultaneously.

The solar atmospheric hot plasma is controlled by magnetic fields where a wide variety of structures ranging from small-scale to large-scale are observed. A few examples of large structures, e.g., prominences, sunspots, coronal hole and small-scale structures, e.g., spicules are shown in the Figure 1.1. Observations of the solar atmosphere over centuries have revealed that it is inhomogeneous at almost all spatial scales and highly dynamic at nearly all the timescales. The dynamical interaction of magnetic flux with convection in the solar interior and the solar surface produces complex magnetic structures which determine the energetics of the solar atmosphere. The granular motions constantly buffet the small-scale magnetic flux at the photosphere that help in generating waves. Furthermore, large-scale as well as small-scale reconnections also take places at different locations and different heights which generate local heating, jets, and also perturb the medium and produce various kind of MHD waves in the solar atmosphere. All these processes are generally coupled throughout the different layers of the solar atmosphere. The chromosphere and the transition region is known as interface region and it plays a significant role in understanding the coupling between the relatively cool photospheric plasma and the hot multi-million-degree corona. Most of the mechanical energy that governs the solar activity and solar atmospheric heating is converted into heat and radiation within this interface region, though a small amount of energy escapes through this region that heat the corona and drive the solar wind. The interface region remains highly complex where the plasma $\beta$, the ratio between the gas pressure and the magnetic pressure, changes its value suddenly from high to low moving from the photosphere to corona. The density also drops by six orders of magnitude, and the temperature rapidly increases from few tens of thousands to million degrees. This has a variety of impacts on waves, such as wave propagation, mode coupling, refraction, and reflection. This interface region is still a poorly understood layer where waves, flows, and shocks manifest in the presence of magnetic fields to form an often nonlinear magnetohydrodynamic system and play a critical role in the coupling. Understanding the chromosphere and TR is a fundamental requirement for explaining the coronal and heliospheric activity.

## 1.2 Motivation for the Current Studies

Understanding the Sun and its variation has been the primary goal of many space missions over four decades, yielding an ever-clearer picture of the physics behind a wide range of active and quiescent phenomena observed on the Sun. It is now understood that the dynamics of the chromosphere, transition region and corona are governed by the magnetic fields, which are rooted in the photosphere and generated in the convection zone. Though the Sun's atmosphere has been observed over centuries, its fine structures and their counterparts in the different solar atmospheric layers are being studied more recently with the advancement of the high-resolution and multi-wavelength observations. For imaging and spectroscopic observations, the biggest challenge has been an inadequate temperature resolution, spectral resolution, cadence and the field of view of the telescopes. As the spatial resolution in observations improved over time, more and more finer structures were discovered in the solar atmosphere. Despite the well-known large-scale structures, e.g., sunspots, complex active regions, coronal loops and coronal holes; the fine structures in the sunspot, mottles, spicules, X-ray, and EUV bright points are observed in greater details. Over the past few decades several space solar missions, such as the Solar and Heliospheric Observatory (SOHO), Transition Region and Coronal Explorer (TRACE), Hinode, etc., and various ground-based observatories have provided a wealth of observational data that has revealed finer details of the solar atmosphere. Simultaneous observations of the different atmospheric layers including the magnetogram at photosphere show the link between the coronal and chromospheric structures/events to photospheric magnetic fields. Magnetic field concentration at the photosphere generally shows strong brightenings in various imaging bands including UV, EUV to X-ray. These observations over the time are broadening our understanding of the coupling of the magnetic field through the solar atmosphere.

It is now acknowledged that the coupling is vital to understand the dynamical changes observed in different layers of the Sun. The coupling of the large scale structures is known and being studied since a long time. But, to understand the coupling of very small-scale events and high-frequency phenomena, one requires very high-resolution observations. The higher-spatial-resolution can not alone solve the problem as smaller structures and the dynamics associated with them will have shorter lifetimes. Though observations with the SOHO, TRACE, etc., have gathered stunning and detailed information about the solar atmosphere, paradoxically, they leave us with a incomplete understanding of these fundamental elements and indicates the requirement of even higher cadence and higher resolution observations. The technological advancement, especially the development of the new generation cameras allowing us to conduct high-cadence observations. With the launch of the successful mission like the Solar Dynamics Observatory (SDO), Interface Region Imaging Spectrograph (IRIS), that has provided us unique high-resolution, high-cadence data to study the photospheric evolution of magnetic structures and their dynamical connection with the upper solar atmospheric layers. A comparison of the resolution and cadence between the solar space instruments launched in 1990's and 2010's is shown in the Table 1.1. One can see that the cadence of the observations has increased significantly in the recent era.

Thus, our understanding of the fine-scale dynamics in the solar atmosphere is advancing with the recent advent of instruments with high spatial, temporal, and

Table 1.1: Comparision between few instruments launched in 1990's and 2010's. The region of atmosphere observed by these instruments including their spatial resolution and cadence are given.

| Time | Name of the Instrument | Primary Region coverage | Spatial Resolution | Typical Cadence |
|---|---|---|---|---|
| 1990's | SOHO/EIT (1995) | Corona | $5.2''$ | $\sim$ few minutes |
| | SOHO/MDI(1995) | Photosphere | $1.2''$ | $\sim$1 minute |
| | TRACE (1998) | Corona, TR | $1''$ | $\sim$1 minute |
| 2010's | SDO/AIA (2010) | Corona | $1.2''$ | 12 sec |
| | SDO/HMI (2010) | Photosphere | $1''$ | 45 sec |
| | IRIS (2013) | Chromosphere, TR | $0.33''$ | $\sim$few to tens of sec |

spectral resolutions, but at the same time such observations are bringing new problems into light. The key goal of the thesis is to understand the small-scale dynamics and coupling of the solar atmosphere at different structures. High spatial resolution, high cadence, simultaneous imaging and spectroscopic coordinated observational data from the recent instruments are revealing finer details of small-scale transients like mottles, Rapid Blueshifted Excursions (RBEs), and Rapid Redshifted Excursions (RREs). Their dynamical effects on the chromospheric power distribution were unknown earlier. Small-scale chromospheric and transition regions jets, e.g., Type I and Type II spicules, are ubiquitously found in the solar atmosphere. More and more details on their dynamical behavior are being explored using multi-wavelength high-resolution observations. The connection between small-scale jets and the dynamical changes observed in the coronal structures, e.g., coronal bright points, coronal plumes, is yet to be explored. The fine-structure dynamics above the sunspot are also explored in different atmospheric heights, whereas the relation between these fine-structures and their coupling remains to be investigated. The high cadence observations may help in understanding the behavior of high-frequency waves and their role in coronal heating.

A few such problems motivated the studies presented in this thesis. At the beginning of the each chapter, a short introduction will provide the current understanding of a particular phenomenon. Moreover, it will also introduce the requirement of further studies of the related phenomenon. Over the thesis, we will show how the high-cadence and high-resolution observation have broadened and improved our current understanding of the small-scale dynamics and the coupling.

## 1.3 Outline of the Thesis

The thesis is a compilation of different high-resolution, high-cadence imaging and spectroscopic studies carried out in the solar atmosphere using data from ground and space based observatories. Broadly, the small-scale transients and waves in the solar atmosphere and their coupling between the different atmospheric layers are studied using high-resolutions spectroscopic and imaging observations. A summary of each chapter of the thesis is outlined here.

In Chapter 1, the solar atmosphere and its general properties are already introduced. Some of the long-standing issues related to corona such as the coronal heating problem and the coupling of the solar atmosphere are discussed here. A few other relevant issues which motivated the present study are also discussed.

Chapter 2 will provide the description of imaging and spectroscopic instruments both from the ground and space based facilities, which have been used in this thesis work. A brief description of the instrument, different modes of operation, and other useful details for each instrument are presented here.

In Chapter 3, the coupling of the waves and small-scale transients through the different layers of the lower solar atmosphere is studied. High-resolution, high-cadence, multi-layer observation of a quiet-Sun region with the Swedish 1-m Solar Telescope (SST) is used to observe the solar atmosphere. H$\alpha$ line scanning images were taken to observe different layers of the atmosphere from the photosphere to upper chromosphere. We study the distribution of power in different period bands at various heights. Powermaps of the upper photosphere and the lower chromosphere show suppressed power surrounding the magnetic network elements, known as magnetic shadows. These also show enhanced power close to the photosphere, traditionally referred to as power halos. The interaction between acoustic waves and inclined magnetic fields is generally believed to be responsible for these two effects. In this study, we explore whether small-scale transients can influence the distribution of power at different heights. We show that the presence of transients, like mottles, Rapid Blueshifted Excursions (RBEs), and Rapid Redshifted Excursions (RREs), can strongly influence the powermaps. The short and finite lifetime of these events strongly affects all powermaps, potentially affecting the observed power distribution. We show that Doppler-shifted transients like RBEs and RREs that occur ubiquitously can have a dominant effect on the formation of the power halos in the quiet Sun. For magnetic shadows, transients like mottles do not seem to have a significant effect on the power suppression around 3 minutes, and wave interaction may play a key role here. Our high-cadence observations reveal that flows, waves, and shocks manifest in the presence of magnetic fields to form a nonlinear magnetohydrodynamic system.

In Chapter 4, the source of the quasi-periodic brightenings in a coronal bright point (BP) is explored. Coronal bright points are small-scale luminous features seen in the solar corona. They originate from the small scale bipolar magnetic flux concentrations at the boundaries of supergranular cells. They are characterized by locally enhanced emission in X-ray, EUV, radio wavelengths and generally associated with the underlying bipolar magnetic field. They generally live for a few hours to a few days and have sizes less than $50''$. With recent high-resolution EUV images, it is clear that a BP is not a point or simple loop-like structure but looks like a little active region with multiple magnetic poles with several connectivities. Quasi-periodic brightenings are frequently observed in the BPs. Several studies have been carried out to understand the periodic nature, but their origin remains inconclusive. We explore the dynamics of a BP seen in the coronal hole using the

EUV images from the Atmospheric Imaging Assembly (AIA) and the magnetic field information from the Helioseismic and Magnetic Imager (HMI) instruments. We also use spectroscopic data from the newly launched Interface Region Imaging Spectrograph (IRIS). The detailed analysis shows that the BP evolves throughout our observing period along with changes in underlying photospheric magnetic flux and shows periodic brightenings in different EUV and far-UV images. With the highest possible spectral and spatial resolution of IRIS, we attempted to identify the sources of these oscillations. IRIS spectroscopic observation provided a unique opportunity to study the time evolution of one footpoint of the BP as the slit position crossed it. Our analysis indicates that small-scale magnetic reconnections produce local heating. It also has a tendency to occur repetitively with an almost equal time interval. Observed periodic intensity changes of BP are likely originating from repetitive reconnection which produces local heating and intensity enhancement.

In Chapter 5, we studied the relation between the spicules and the quasi-periodic propagating intensity disturbances in the coronal loops. Spicules are small, hairy-like structures seen at the solar limb, mainly at chromospheric and transition region lines. They generally live for 3 - 10 minutes. We study these spicules in a south polar region of the Sun with coordinated observations using the IRIS and the AIA instruments. Propagating disturbances (PDs) are observed everywhere in the polar off-limb regions of the Sun at coronal heights. From these simultaneous observations, we show that the spicules and the PDs may have originated through a common process. From spacetime maps, we find that the start of the trajectory of PDs is almost cotemporal with the time of the rise of the spicular envelope as seen by IRIS slit-jaw images at 2796 and 1400 Å. During the return of spicular material, brightenings are observed in AIA 171 and 193 Å images. The quasi-periodic nature of the spicular activity, as revealed by the IRIS spectral image sequences, and its relation to coronal PDs, as recorded by the coronal AIA channels, suggest that they share a common origin. We propose that reconnection-like processes generate the spicules and waves simultaneously. The wave escapes while the cool spicular material falls back.

In Chapter 6, fine-structure dynamics above the sunspot are studied. Recent high-resolution observation reveals that subarcsecond bright dots (BDs) with less than a minutes lifetime appears ubiquitously in the transition region (TR) above sunspot penumbra (Tian *et al.* 2014b). The presence of penumbral micro-jets (PMJs) in the chromosphere are also reported earlier (Katsukawa *et al.* 2007). It was proposed that both the PMJs and BDs are formed due to magnetic reconnection process and may play an important role in heating the penumbral materials. Using simultaneous observations of the chromosphere from the Solar Optical Telescope (SOT) and the transition region from the IRIS we study the dynamics of BDs and their relation with PMJs. Bright dots are clearly seen in the IRIS 1400 slit-jaw images (dominated by the TR temperature) above sunspot penumbra. They generally appear elongated along the bright filamentary structures of penumbra and show an apparent movement both inward and outward direction from the center of the sunspot. On the other hand, PMJs with less than a minute lifetime are also observed to move outward in the SOT Ca II H images (capture primarily chromospheric emission). Using combined observation, we compare these two features and try to identify if they have a common origin. We find two types of BDs, one is related to PMJs and the other do not show any visible dynamics in the SOT Ca II H images. From a statistical analysis, we show that these two types have different properties. We find that the BDs which are related to PMJs always appears at the end point of the PMJ and show inward motion (opposite to the jet direction). This behavior is puzzling and can not be explained by a simple reconnection model. In this work, we explore the relationship and propose a new picture for formation of BDs and their relation to PMJs.

Chapter 7 deals with the observation of the high-frequency oscillations their damping in the coronal structure. During the total solar eclipse of 11 July 2010, multi-slit spectroscopic observations of the solar corona were performed from Easter Island, Chile. To search for the high-frequency waves, observations were taken at a high cadence in the green line at 5303 Å that is due to [Fe XIV] and the red line at 6374 Å that is due to [Fe X]. The data were analyzed to study the periodic variations in intensity, Doppler velocity, and line width using wavelet analysis. The data with high spectral and temporal resolution enabled us to explore the rapid dynamical changes within coronal structures. We find that at certain locations, each parameter shows significant oscillation with periods ranging from 6 - 25 s. For the first time, we were able to detect damping of high-frequency oscillations with periods of about 10 s. If the observed damped oscillations are due to MHD waves, then they can contribute significantly to the heating of the corona. From a statistical study, we try to characterize the nature of the observed oscillations while considering the distribution of power in different line parameters.

Chapter 8 contains the summary of entire thesis work. The key findings from various studies are outlined here. Some of the possible future prospects of these studies are also discussed.

# Chapter 2

# Instruments

In this chapter, the instruments that are used to study the solar atmosphere are introduced briefly. Most of these instruments are operated and maintained by the instrument team members, although a broad scientific community uses the data. The details of the instruments are available online. The data reduction details of these instruments are provided by the team and also available online. A brief description of these instruments is given below. The data reduction methods are described in the respective chapters where the data from a particular instrument is used.

## 2.1 Swedish 1-meter Solar Telescope (SST)

The Swedish 1-m Solar Telescope (SST; Scharmer *et al.* 2003a) is one of the biggest solar telescopes in the world. The telescope is owned and operated by the Institute for Solar Physics of the Royal Swedish Academy of Sciences. It is located at the Roque de los Muchachos Observatory in the island of La Palma, Spain, which is

Figure 2.1: The Swedish 1-meter Solar Telescope (SST) at La Palma, Spain. The visible tower hides a vacuum tube over which the primary of 1-meter fused silica lens is placed which converges the solar light at the base and form an image. *Image credit:* https://www.mn.uio.no

one of the best location for optical and infrared astronomy. The SST is a vacuum telescope, meaning that air is evacuated from the telescope to avoid disruption of the image from the air due to heating. Its excellent location combined with high optical quality, adaptive optics, and advanced image restoration techniques allow us to study the solar structures with unprecedented details.

The SST can operate in two modes. One is a spectrograph mode, known as the TRI-Port Polarimetric Echelle-Littrow (TRIPPEL) spectrograph. The other mode is an imaging mode, called CRisp Imaging SpectroPolarimeter (CRISP). The CRISP instrument is described below, since the data from only this instrument is used in this thesis work.

### 2.1.1 CRisp Imaging SpectroPolarimeter (CRISP)

CRISP is an imaging spectropolarimeter. It is based on a dual Fabry-Perot interferometer (FPI) system similar to that described by Scharmer (2006); Scharmer *et al.* (2008). The image from the telescope is split up in a red and a blue beam by a dichroic beam-splitter. The red beam goes through the tunable FPI which is known as the CRISP. It operates from 5100 to 8600 Å and is capable of measuring the polarization with the help of a liquid crystal modulation combined with a polarizing beamsplitter. The total system consists of three 1k×1k Sarnoff CCDs; two are used for direct observations, and the third is used for the Multi-Object Multi-Frame Blind Deconvolution (MOMFBD) image reconstruction method.

## 2.2 Interface Region Imaging Spectrograph (IRIS)

The Interface Region Imaging Spectrograph (IRIS; De Pontieu *et al.* 2014) is a NASA Small Explorer Mission to study the solar atmosphere. It was launched into a Sun-synchronous orbit on 27 June 2013 using a Pegasus-XL rocket. The primary aim of this instrument is to study the chromosphere and the transition region of the Sun. It is consists of a 19-cm UV telescope which feeds light into a slit-based dual-bandpass imaging spectrograph. It is capable of obtaining UV spectra and images with high resolution in space (0.33 - 0.4″) and time (1 - 2 s). The spectra in passbands from 1332 - 1358 Å , 1389 - 1407 Å , and 2783 - 2834 Å , including strong spectral lines formed in the chromosphere (Mg II h 2803 Å and Mg II k 2796 Å) and transition region (C II 1334/1335 Å and Si IV 1394/1403 Å) can be capture by three CCD cameras. Slit-jaw images can be taken simultaneously in four different passbands (C II 1330, Si IV 1400, Mg II k 2796, and Mg II wing at 2830 Å). It can also obtain spectral rasters with a sample regions up to 130″×175″ at a variety

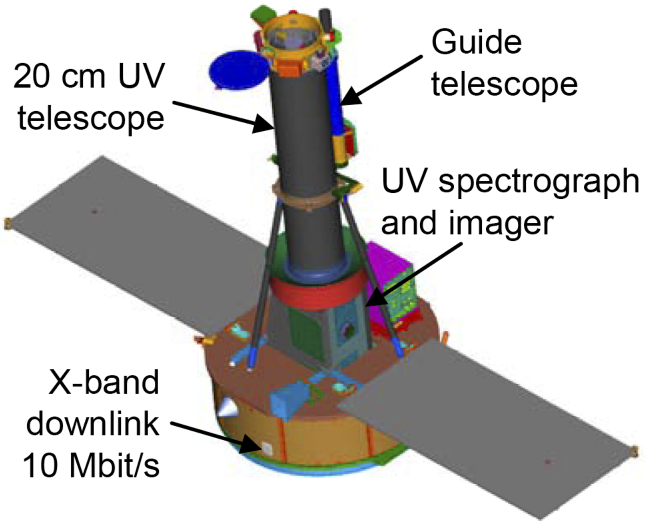

FIGURE 2.2: A schematic of the IRIS spacecraft. *Image credit:* http://iris.lmsal.com

of spatial samplings (from 0.33″ and up). The instrument can operate in many modes while changing the exposure, cadence, FOV, etc.

## 2.3 Solar Dynamics Observatory (SDO)

Solar Dynamics Observatory (SDO; Pesnell *et al.* 2012) is the first space-weather mission launched under NASA's Living With a Star (LWS) program which is designed to understand the causes of solar variability and its impacts on Earth. It was launched on February 11, 2010 from Kennedy Space Centre in Florida. The main goal of the SDO is to understand the Sun's influence on the life on Earth and technological systems by monitoring the solar interior and different layers of its atmosphere with high spatial and temporal coverage and in many wavelengths simultaneously and make predictive capability of Space-weather. The satellite is placed in a geosynchronous orbit inclined by 28.5° which allows the contact with a single dedicated ground station. The orbit provides a nearly continuous view of the Sun, apart from two eclipse seasons (due to the shadow of Earth) and three Lunar

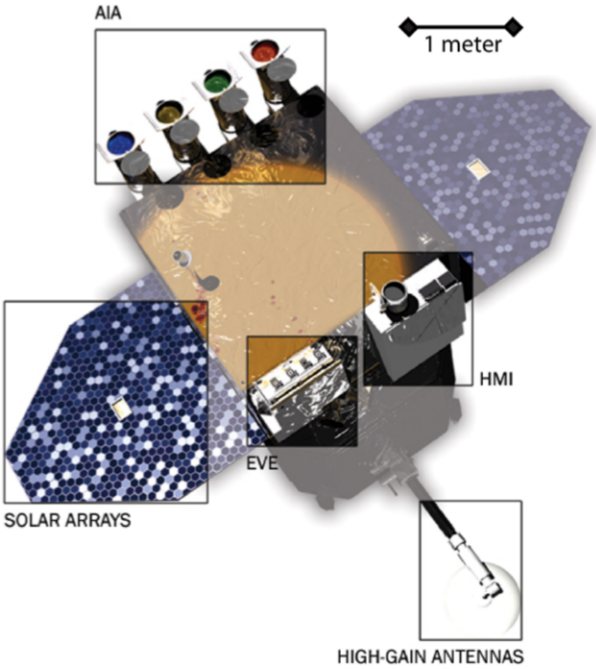

FIGURE 2.3: The SDO spacecraft with all the three instruments onboard highlighted. The high-gain antennas and the solar arrays can also be seen in this figure. *Image credit:* Pesnell *et al.* (2012)

transit per year during which there will be daily interruptions in the observations. The high spatial and temporal coverage produces a large volume of data, which is continuously downlinked at the SDO-dedicated ground station in New Mexico.

There are three instruments onboard SDO; the Atmospheric Imaging Assembly (AIA) which is prepared in partnership with the Lockheed Martin Solar & Astrophysics Laboratory (LMSAL), the Helioseismic and Magnetic Imager (HMI) developed in collaboration with Stanford University, and the Extreme Ultraviolet Variability Explorer (EVE) build in partnership with the University of Colorado at Boulder's Laboratory for Atmospheric and Space Physics (LASP). Figure 2.3 shows the SDO spacecraft with different instruments onboard highlighted. This observatory started its science operations on May 1, 2010. The AIA and HMI instruments are described in details below, since the data from these two instruments are used in this thesis work.

### 2.3.1 Atmospheric Imaging Assembly (AIA)

Atmospheric Imaging Assembly (AIA; Lemen *et al.* 2012) is an array of four telescopes that observe the solar atmosphere in 10 different wavelength bands nearly simultaneously. Figure 2.3 shows the AIA instrument where four telescopes with their individual guide telescopes mounted on the spacecraft can be seen. With a primary aperture of 20 cm, each telescope captures the full disk image on a 4k×4k CCD at a spatial resolution of $\approx 0.6''$ per pixel. The circular field of view (FOV) of diameter 41 arcmin allows the observations of the solar atmosphere up to 0.28 $R_\odot$ above the limb. Ten different wavelength bands that include seven extreme ultraviolet, two ultraviolet, and one visible-light band to reveal new perspectives of the solar corona. The wavelength bands can diagnose the solar atmosphere over the range of 6000 K to 20 MK. The cadence at which images are captured in the standard observing mode is 12 s. The instrument calibration, wavelength responses, and other related information can be found in Boerner *et al.* (2012).

### 2.3.2 Helioseismic and Magnetic Imager (HMI)

The Helioseismic and Magnetic Imager (HMI; Schou *et al.* 2012) can study the solar interior using helioseismic techniques as well as the magnetic field near the solar surface. It uses the principal of the Zeeman effect of the Fe I 6173 Å line, to measure the Stokes parameters required to make the longitudinal and vector magnetograms of the entire visible disk of the Sun at a resolution of $0.5''$ per pixel. It also measures the intensity and creates Dopplergrams of the full disk every 45 s at the same resolution using the Doppler shift measured from the same spectral line.

## 2.4 Hinode

Hinode, formerly known as Solar-B (Kosugi *et al.* 2007), is a space-based solar mission developed, launched, and operated by the Institute of Space and Astronautical Science (ISAS) – a division of the Japanese Aerospace Exploration Agency (JAXA), in collaboration with several space agency partners from the United Kingdom and the United States. It was successfully launched from Uchinoura Space Centre at Uchinoura Kagoshima, Japan on 23 September 2006. After the launch, the Solar-B spacecraft was named Hinode which means *Sunrise* in Japanese. It was kept in a Sun-synchronous circular dawn/dusk orbit with an altitude of 600 km and an inclination of 97.9°. This orbit keeps the instruments in a nearly continuous sunlight, with no day/night cycling for nine months each year. The aim of the mission was to observe the response of the chromosphere and corona to changes in the magnetic and velocity fields of the photospheric and sub-photospheric layers of the Sun.

It has three instruments onboard, the Solar Optical Telescope (SOT), the Extreme ultraviolet Imaging Spectrometer (EIS) and the X-Ray Telescope (XRT) that observe the Sun in optical, EUV and X-ray wavelengths respectively. Figure 2.4 shows a cartoon image of the Hinode spacecraft with the three instruments onboard. Detailed information on the spacecraft design, its operations, and scientific objectives, can be found in Kosugi *et al.* (2007). In the following section, the SOT is described in detail, since the data obtained from it is a part of this thesis.

### 2.4.1 Solar Optical Telescope (SOT)

The Solar Optical Telescope (SOT; Tsuneta *et al.* 2008) on board Hinode is the largest aperture solar telescope flown in space. It is designed and developed by the

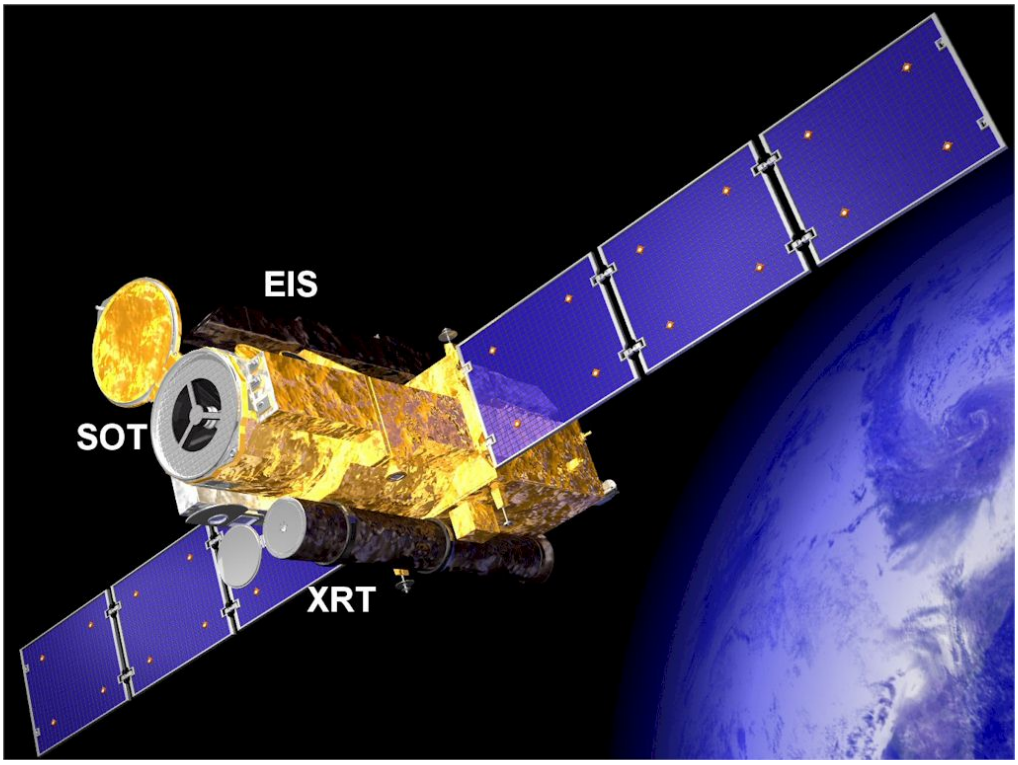

FIGURE 2.4: Hinode spacecraft with the positions of the instruments SOT, EIS and XRT. *Image credit:* JAXA

international collaboration between National Astronomical Observatory of Japan (NAOJ), Lockheed Martin Advanced Technology Center (LM), Mitsubishi Electric Corporation (MELCO), NCAR High Altitude Observatory (HAO), NASA MSFC, and JAXA. It is consists of a 50-cm aperture primary within the Optical Telescope Assembly (OTA) and the camera system within the Focal-Plane Package (FPP). The FPP consists of three optical instruments at the SOT focal plane, the Broadband Filter Imager (BFI), the Narrowband Filter Imager (NFI), and the SpectroPolarimeter (SP). It provides diffraction limited images ($\sim 0.2''$ resolution) of the photosphere and chromosphere The ability to make continuous, seeing-free, diffraction limited observations with enhanced stability using active image stabilization, is the highlight of SOT. The combined SOT system is optimized for measurement of the vector magnetic field in the photosphere and to study the dynamics of both the photosphere and chromosphere. The FG camera suddenly developed an electrical short circuit on 2016 February 25, after 9.4 years of operation on-orbit, and it is now permanently switched off, but other two cameras are unaffected, and continuing observations. Hinode and SOT are continuing a full schedule observations, including Hinode Observing Programs (HOPs) and frequent coordination with the IRIS and other observatories.

## 2.5 Multi-slit spectrograph for observation of the corona during total solar eclipse

High-cadence observation of the corona is difficult from space as there are limitations in data downlink but can be achieved during the total solar eclipse from the ground. The observations during total solar eclipses have the advantage that coronal emission line profiles are free from photospheric light scattered by the sky and provide ideal opportunities to study the corona. During the total solar eclipse of 11 July 2010, a team from the Indian Institute of Astrophysics, Bangalore have performed a Multi-slit spectroscopic observation of the solar corona at Easter Island, Chile, at latitude S $27^\circ\,09'$ and longitude W $109^\circ\,26'$. High-resolution spectroscopic observations of the corona in the green emission line [Fe XIV] at 5303 Å and the red line [Fe X] at 6374 Å were carried out during the total solar eclipse. A schematic diagram of the experimental set-up is shown in Figure 2.5. A two-mirror (M1 and M2) coelostat system was used to track the Sun and to direct the sunlight continuously to the spectrograph through an objective lens (Obj). The alignment of coelostat and tracking speed was selected to achieve negligible movement of the image on the slits of the spectrograph. Using an enlarged image of the Sun, we found that the drift of the image due to small misalignment and tracking speed over a period of 20 minutes was less than $5''$. This implies that the drift of the image was less than $1''$ during the totality phase of the eclipse, which is much less than the width of the slits ($20.5''$). An objective lens (Obj) of 10 cm diameter

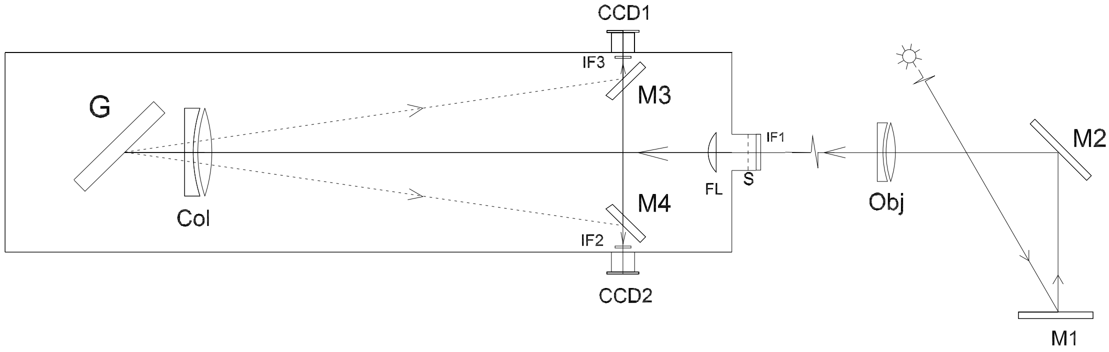

FIGURE 2.5: Schematic diagram of the optical layout used to obtain spectra around the red and green emission lines of the solar corona. M1 and M2 = flat mirrors of the coelostat system. Obj = objective lens of 10 cm diameter and of 100 cm focal length. IF1 = interference filter with transmission in the wavelength between 5000 - 7000 Å, S = four slits separated by 5 mm each, FL = field lens to focus objective on the collimator, Col = collimator and camera lens of the spectrograph, G = grating with 600 lines mm$^{-1}$ blazed at 2.2 $\mu$m, M3 and M4 = Flat mirrors to divert the spectral beams, IF2 and IF3 = narrow-band interference filters with a FWHM of 4 Å, CCD1 and CCD2 = detectors to record the spectra.

and 100 cm focal length formed a 9.3 mm size image of the Sun on the four slits (S) of the spectrograph. An interference filter (IF1) with a passband of about 5000 - 7000 Å was mounted in front of the slits to block other light due to higher and lower orders. The “slit-width” of each slit was 100 micron (which corresponds to $20.5''$ on the Sun), and they were separated by 5 mm from the adjacent slit. This separation was mutually compatible for both the dispersion of the spectra and passband of narrow-band filters. Each slit with a length of 25 mm permits the recording of spectra up to 2.5 $R_\odot$, but the detector size limited the spectra up to about 1.7 $R_\odot$. A field lens (FL) just behind the slits avoided spilling of the beam outside of the collimator (Col). A grating (G) of 600 lines mm$^{-1}$ blazed at 2.2 $\mu$m and a lens (Col) of 140 cm focal length in Littrow mode provided the spectra. The third-order 6374 Å wavelength and fourth-order 5303 Å wavelength regions were selected for observations as it was easy to focus by the same collimator lens (Col). The final configuration provided a dispersion of 3.3 Å mm$^{-1}$ and 2.3 Å mm$^{-1}$ around the third-order order red and fourth-order green emission line, respectively. We could not mount the CCD detectors (CCD1 and CCD2) directly on the focused spectral region because there was too little space. Therefore, we used 75 mm flat mirrors (M3 and M4) to divert the red and green wavelength regions of the spectrum, as shown in Figure 2.5, and mounted two CCD detectors. Two narrow-band interference filter (IF2 and IF3) with passband of 4 Å centered on 6374 Å for the red line and on 5303 Å for the green line were installed in front of the detector (CCD1 and CCD2) to avoid the overlap of spectra due to the two adjacent slits.

A 13 μm pixel size of the CCD detector was capable of providing a resolution of 0.043 Å in the third-order of the red line, but the slit width of 100 μm limited the spectral resolution to 0.33 Å. The pixel resolution along the slit is $2.64''$ for the red line spectra. The EM-CCD camera of ANDOR of 1k x 1k format with 14–bit read out at 10 MHz was used in the frame transfer mode for taking the spectra around the red emission line with a cadence of 1.013 s (exposure time of 1 s and 0.013 s for frame transfer). The gains of the EM-CCD camera was set at 200 to enhance the signal to a reasonable level. The electron multiplication (EM) detector magnifies the week signals with some increase in the noise. The net result is that it provides the possibility of studying the week signals with very high temporal resolution. We had only one CCD camera that could be operated in frame-transfer mode, but had another detector without EM facility. We therefore used another CCD camera (ANDOR) of 2k×2k format with a 13.5 μm pixel$^{-1}$ size to record the spectra in the green line. The read-out speed was lower, 2 MHz with 16–bit data. The chip was binned 2×2 to decrease the read time by a factor of two, and the region was also reduced to 75 % to decrease the read-out time even more. The binned detector had a pixel resolution of 0.062 Å, but the slit width restricted the spectral resolution to 0.23 Å in the green channel. The green line spectra have a $5.52''$ pixel resolution along the slit. The spectra in the green emission line were recorded with a cadence of 3.64 s (exposure time of 3 s and read-out time of 0.64 s including shutter operation). It may be noted that the estimate of the exposure times in both cases was obtained by making the observations during the period of a full moon at night while testing the experimental set-up. The dark signal

Table 2.1: The list of imaging channels and spectral lines used in the thesis. The region of atmosphere that observed by different instruments including the primary ion(s) observed and their characteristic temperatures are given.

| Primary region coverage of the atmosphere | Instrument | Imaging Channels/ Spectral Lines | Primary ion(s) | Char. log(T) |
|---|---|---|---|---|
| Photosphere | CRISP | Wide-Band | H$\alpha$ continuum | $\sim$3.7 |
| | CRISP | Stokes V | Fe 6301 Å | $\sim$3.7 |
| | AIA | 1700 Å | continuum | $\sim$3.7 |
| | HMI | Stokes V | Fe I 6173 Å | $\sim$3.7 |
| | IRIS | 1401 Å (Spectra) | S I | $\sim$3.7 |
| Chromosphere & TR | CRISP | 6563 Å | H$\alpha$ core | 4.3 |
| | AIA | 304 Å | He II | 4.7 |
| | AIA | 1600 Å | C IV+cont. | 5.0 |
| | SOT | 3969 Å | Ca II H | 4.0 |
| | IRIS | 1330 Å | C II | 3.7 – 7.0 |
| | IRIS | 2796 Å | Mg II h/k | 3.7 – 4.2 |
| | IRIS | 1400 Å | Si IV | 3.7 – 5.2 |
| | IRIS | 1394 Å (Spectra) | Si IV | 4.9 |
| Corona | AIA | 171 Å | Fe IX | 5.8 |
| | AIA | 193 Å | Fe XII, XXIV | 6.2, 7.3 |
| | AIA | 211 Å | Fe XIV | 6.3 |
| | AIA | 335 Å | Fe XVI | 6.4 |
| | AIA | 94 Å | Fe XVIII | 6.8 |
| | Eclipse obs. | 6374 Å (Spectra) | Fe X | 6.3 |
| | Eclipse obs. | 5303 Å (Spectra) | Fe XIV | 6.1 |

was obtained for calibration by closing the slits of the spectrograph and recording data under the same conditions. The solar disc spectra were also obtained during a period of clear sky to convert the observed coronal intensity to the absolute units. The 27 mm size of the detector permitted us to record the spectra up to $\sim$ 3 $R_\odot$ in the green channel. The short exposure time did not allow obtaining spectra with fourth slit because of a decrease in the emission line intensity, which was too far above the solar limb. At the location of the third slit, it appears that the intensity of the emission corona was not sufficient to make a distinct impression of the emission component over the continuum background. Finally, we obtained spectra with two slits, which are shown in the Figure 7.1. The data reduction methods and the results obtained from this experiment are presented in the Chapter 7.

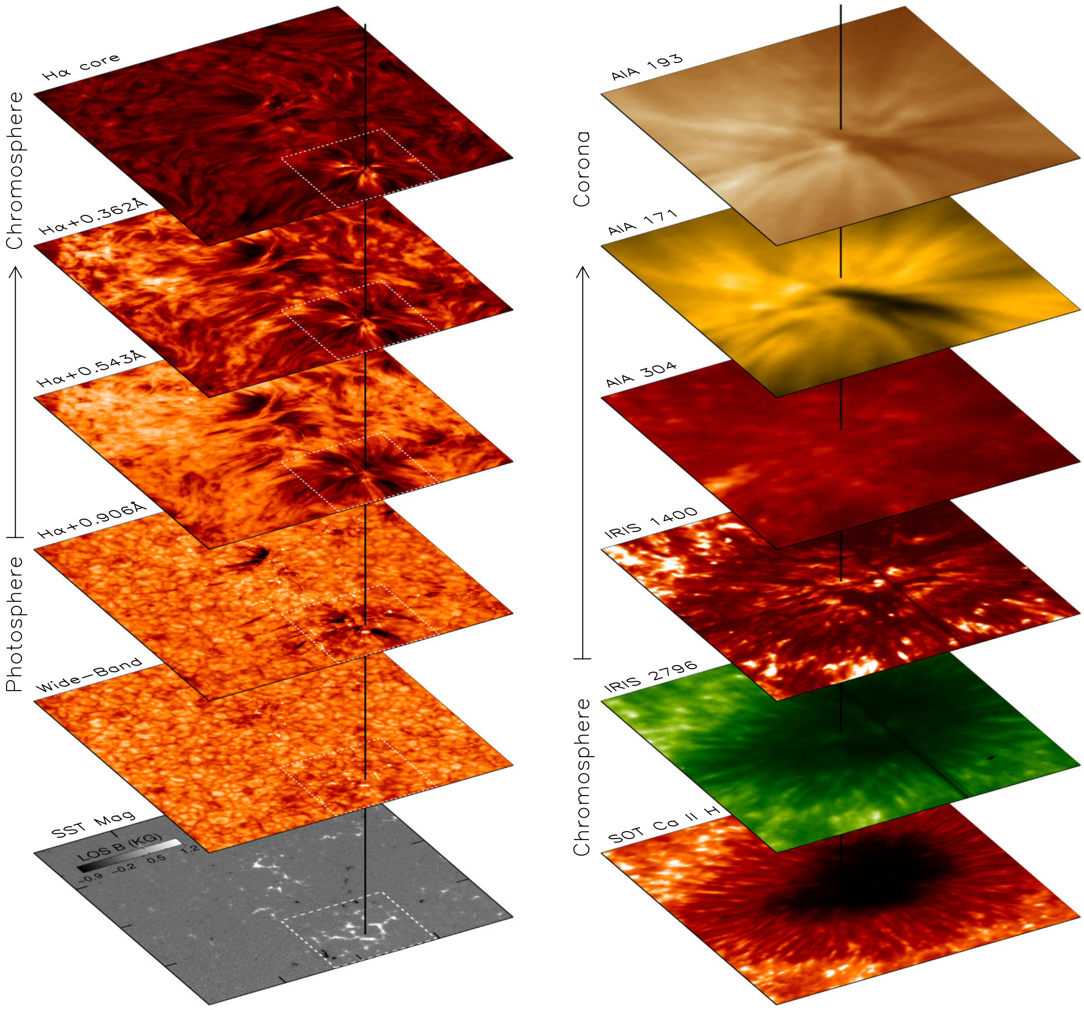

FIGURE 2.6: *Left:* Images of a quiet-Sun region as seen in different layers of the solar atmosphere along with the corresponding magnetogram from photosphere at the bottom. The observation is taken with the CRISP/SST. *Right:* Images of a sunspot as obtained from a coordinated multi-layer observation from the SOT, IRIS and AIA instruments to cover from the chromosphere to the corona.

Table 2.1 shows the list of imaging channels and spectral lines used to study the coupling through the atmosphere. When observed through filters of different wavelength, images corresponding to different atmospheric layers can be obtained since the different filters are sensitive to different temperatures. Using many such imaging filters, one can study the different layers of the solar atmosphere simultaneously. Two representative examples of multi-layers observation are shown in the Figure 2.6. The left image shows the view of a quit-Sun network region from the photosphere to Chromosphere. H$\alpha$ line scanning images were taken to observe different layers of the solar atmosphere from the photosphere to upper chromosphere with the SST/CHRISP instruments. The images corresponding to the right panel show a sunspot region as seen by the Hinode/SOT, IRIS, and SDO/AIA instruments. A broad temperature region from the chromosphere, transition region to corona is covered from a simultaneous observation with these instruments. Note that a particular instrument generally covers a specific temperature of the atmosphere. Hence, to understand coupling and dynamical connections between different layers, one requires simultaneous observations from various instruments.

# Chapter 3

# Waves and transients in the lower solar atmosphere and their effects on the power distributions[†]

## 3.1 Introduction

Waves in the solar atmosphere are studied with great interest as they carry mechanical energy and also provide insight into the physical parameters through seismology (Roberts 2000; Banerjee *et al.* 2007; Zaqarashvili and Erdélyi 2009; De Moortel and Nakariakov 2012; Jess *et al.* 2015). Oscillations are observed ubiquitously throughout the solar atmosphere and are often interpreted in terms of various magnetohydrodynamic (MHD) modes. Acoustic waves ($p$-modes), which are generated inside the Sun, are generally trapped inside it. These waves can

---

[†] Results of this work are published in Samanta *et al.* (2016a).

All the animations that are referred to in this chapter are available at `http://dx.doi.org/10.3847/0004-637X/828/1/23` freely propagate from the surface into the atmosphere if they have periods shorter than 3.2 minutes (5.2 mHz), which is known as the acoustic cut-off period. The longer periods generally do not propagate to greater heights and are, instead, evanescent. There is substantial observational evidence for the presence of long period oscillations (Vecchio *et al.* 2007; Kontogiannis *et al.* 2010a, 2014; Bostancı *et al.* 2014) in the chromosphere around network magnetic elements. Small-scale magnetic flux concentrations at the boundaries of supergranular cells extend upwards into the chromosphere. These flux tubes expand into funnel-like structures with height due to a decrease in the ambient gas pressure. Some field lines locally connect within the photosphere and produce a canopy-like structure in the chromosphere and some of them reach the corona. It appears that the presence of these kind of network magnetic field configuration interfere with the wave propagation (Rosenthal *et al.* 2002; Bogdan *et al.* 2003). Roberts (1983), Centeno *et al.* (2006) and Khomenko *et al.* (2008) argue that strong magnetic fields change the radiative relaxation time, which can increase the cut-off period significantly. There are also suggestions that the field inclination plays a very important role in long-period wave propagation (Carlsson and Bogdan 2006; Jess *et al.* 2013; Kontogiannis *et al.* 2014). Heggland *et al.* (2011) show that for long-period wave propagation, the field inclination is much more important than the radiative relaxation time effect. Highly inclined magnetic fields significantly increase the cut-off period and create magnetoacoustic portals (Jefferies *et al.* 2006) for the propagation of long-period waves in the chromosphere. This is commonly referred to as leakage of photospheric oscillations into the chromosphere (De Pontieu *et al.* 2004). The "leakage" of long-period photospheric oscillations takes place through magnetic network elements through restricted areas. Recent studies show that a good fraction of power is present above the cut-off period at higher layers around the quiet magnetic network elements (Judge *et al.* 2001; McIntosh *et al.* 2003; Moretti *et al.* 2007; Vecchio *et al.* 2007; Kontogiannis *et al.* 2010b). Two-dimensional powermaps of period bands around 3 minutes reveal two distinct phenomena above network and around elements. One is known as "power halos", which are upper-photospheric regions where the wave power is enhanced. The other is "magnetic shadows", which refer to the regions of the power suppression around network elements in the chromosphere.

Many researchers have suggested that the interaction between the acoustic waves and the magnetic fields is responsible for the formation of magnetic shadows and power halos (Judge *et al.* 2001; McIntosh *et al.* 2003; Moretti *et al.* 2007; Vecchio *et al.* 2007; Kontogiannis *et al.* 2010b). It was proposed that the upward propagating acoustic waves change their nature at the magnetic canopy, a layer where the gas pressure becomes equal to the magnetic pressure, and undergo mode conversion and transmission processes (Nutto *et al.* 2010). Simulations show that acoustic waves generally transfer their energy partly to the slow magnetoacoustic waves (mode transmission) and partly to the fast magnetoacoustic waves (mode conversion) at the canopy (Nutto *et al.* 2012b). Due to high velocity gradients, the fast mode undergoes reflection at the canopy and increases the oscillation power at lower heights, creating power halos (Nutto *et al.* 2012a). In contrast, the slow mode continues to propagate along the slanted magnetic field lines. Kontogiannis *et al.* (2014) argue that the key parameter in mode conversion mechanism is the attack angle (the angle between the direction of wave propagation and the magnetic field) and the period of the acoustic waves. They show that the transmission is generally favored at small attack angles and long periods, while the conversion dominates when the period is small and the attack angle is large, which causes the power halos and magnetic shadows to form around magnetic network regions.

However, most of the earlier studies that put forward the theory based on magnetoacoustic wave reflection did not consider the effect of transients nor the evolution of magnetic fields and other factors leading to changes in the visible chromospheric canopy. Earlier observations were also limited by temporal resolution that were too low to study the influence of short-lived transients in detail. With our high spatial and temporal resolution observations taken with the 1-m Swedish Solar Telescope (SST), we revisit the subject and attempt to provide an alternative interpretation for the formation of the magnetic shadow and power halo. Section 3.2 describes the observations along with data reduction procedures. It also includes the results in terms of power distribution at several heights in the chromosphere. Section 3.3 deals with possible scenarios which can explain our observations and compares with earlier interpretations. Finally, conclusions are drawn in Section 3.4.

## 3.2 Data analysis and Results

### 3.2.1 Observations and Data Processing

Observations of a quiet-Sun region were made on 2013 May 3, from 09:06 UT to 09:35 UT using the CRisp Imaging SpectroPolarimeter (CRISP; Scharmer 2006; Scharmer *et al.* 2008), at the (SST; Scharmer *et al.* 2003a). Images were taken at 7 wavelength positions scanning through the H$\alpha$ line, at -0.906, -0.543, -0.362, 0.000, 0.362, 0.543, and 0.906 Å from the line core, corresponding to a velocity range of -41 to +41 km s$^{-1}$. Adaptive optics was employed in the observations with the upgraded 85-electrode system (Scharmer *et al.* 2003b).

All the data were reconstructed using Multi-Object Multi-Frame Blind Deconvolution (MOMFBD; Löfdahl 2002; van Noort *et al.* 2005), with the 51 Karhunen-Loève modes sorted by order of atmospheric significance and 88$\times$88 pixel subfields. An early version of the pipeline described in de la Cruz Rodríguez *et al.* (2015) was used. Destretching (Shine *et al.* 1994) was used together with auxiliary wide-band objects for consistent co-alignment of different narrow-band passbands, as described in Henriques (2012). Spatial sampling is 0.058$''$ pixel$^{-1}$, and the spatial resolution reaches up to 0.16$''$ in H$\alpha$ covering a field of view (FOV) of 40$\times$40 Mm$^2$.

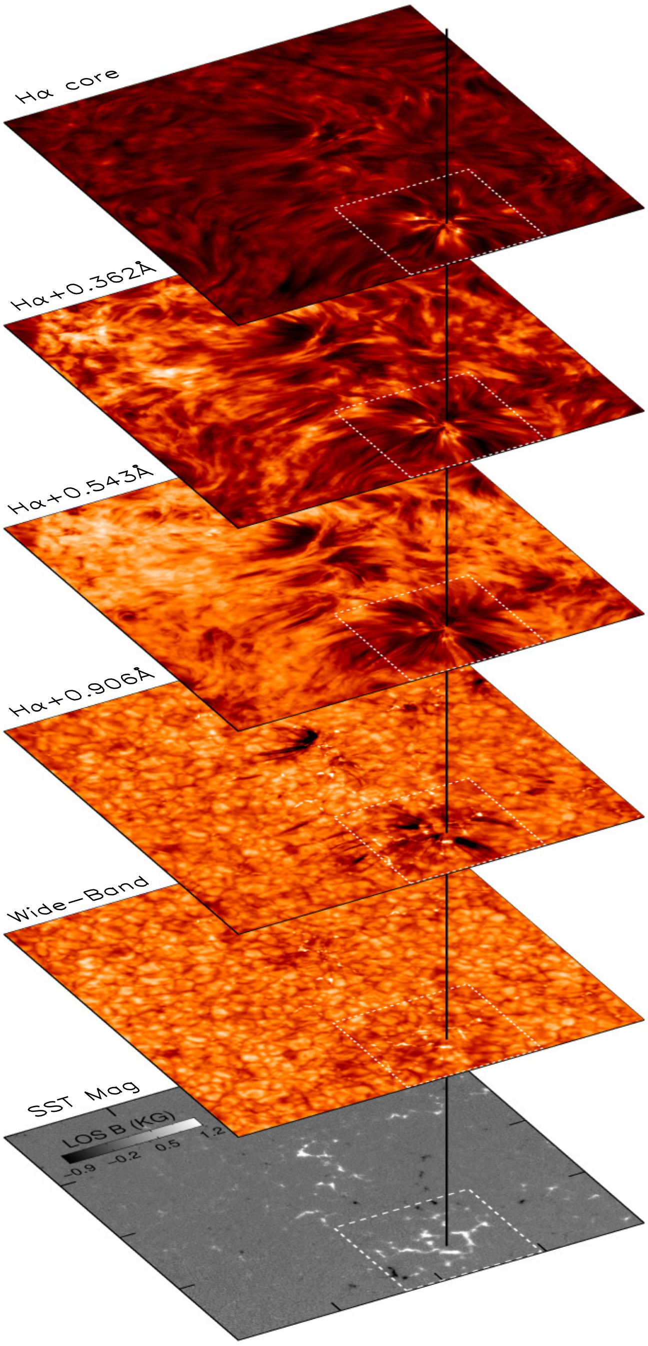

FIGURE 3.1: Images of a quiet region as seen in different layers of the solar atmosphere along with the corresponding magnetogram from photosphere at the bottom. Bottom to top: line-of-sight (LOS) magnetogram obtained by using Fe 6302 Å Stokes V profiles, visible continuum, and narrow-band filter images taken at different positions across the Hα line profile as indicated (Hα + 0.906 Å, Hα + 0.543 Å, Hα + 0.362 Å and Hα core). The long tick marks on the magnetogram represent 10 Mm intervals. The region outlined by the dotted line covers a network region is further studied in Figure 3.5, 3.6 and 3.11. An animation of this figure is available online.

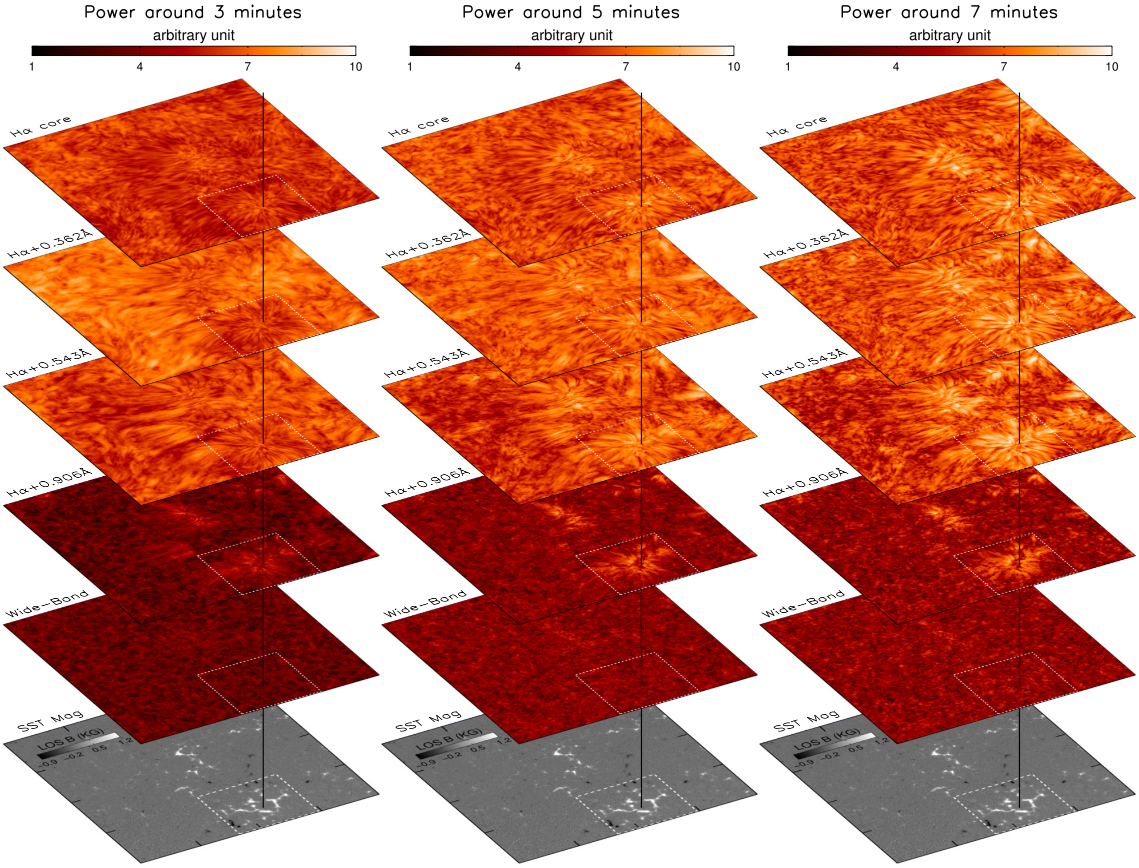

FIGURE 3.2: Powermaps in different layers in three one-minute wide period bands around 3, 5, and 7 minutes. Corresponding photospheric magnetograms are shown at the bottom. The long tick marks on the magnetogram represent 10 Mm intervals.

After reconstruction, the cadence of a full spectral scan was 1.34 s. In this work, we also made use of wide-band images obtained with the CRISP reference camera. This camera is behind the H$\alpha$ pre-filter but before the double Fabry-Pérot. The pre-filter has a 1 nm passband centered at the core of the line. The images from this camera provide the anchor channel for MOMFBD reconstruction and the reference for all post-reconstruction destretch-based techniques. The vast majority of the light contributing to the images from this camera come from the photospheric wings of the H$\alpha$ line. The cadence of the wide-band was also 1.34 s.

Line-of-sight (LOS) magnetograms were produced from the Stokes V output of Fe 6301 Å spectral scans (taken at 16 wavelength positions) using the center of gravity (COG) method (Rees and Semel 1979; Uitenbroek 2003). These scans were acquired at a cadence of ∼5 minutes over the same FOV. The same H$\alpha$ camera was used for obtaining Stokes V data. Hence there were gaps of ∼27 s at ∼5, 11, 16, and 21 minutes of observation. We have interpolated these data gaps using a spline function to obtain a regular cadence for time series analysis. Note that the treatment via spline-fitting is smoothly "bridging" intensity in the time series whereas Rapid Blueshifted Excursions (RBEs)/Rapid Redshifted Excursions (RREs) and mottles cause strong dips in the intensity. Further details on the observations and data reduction are given in Kuridze *et al.* (2015) and Henriques *et al.* (2016).

H$\alpha$ core maps were produced using Doppler compensation. For this, at first, we increased the line profile sampling by a factor of 10 times more than the original using spline interpolation, then the minimum value of the profile is calculated at each pixel to produce the Doppler-compensated H$\alpha$ core maps. This procedure minimizes the effects of strong flows that might shift the position of the line core, and thus best represents the emission coming from the line-forming region (see, e.g., Jess *et al.* (2010)). The LOS Doppler velocity maps were determined by the COG method.

The H$\alpha$ line core forms at the chromosphere and the wings form at lower atmospheric heights (Leenaarts *et al.* 2006, 2012). Filtergram images taken at different positions of the H$\alpha$ line sample, on average, different atmospheric layers and are shown in Figure 3.1. A time lapse movie of this figure is also available online. The movie clearly shows the presence of transients.

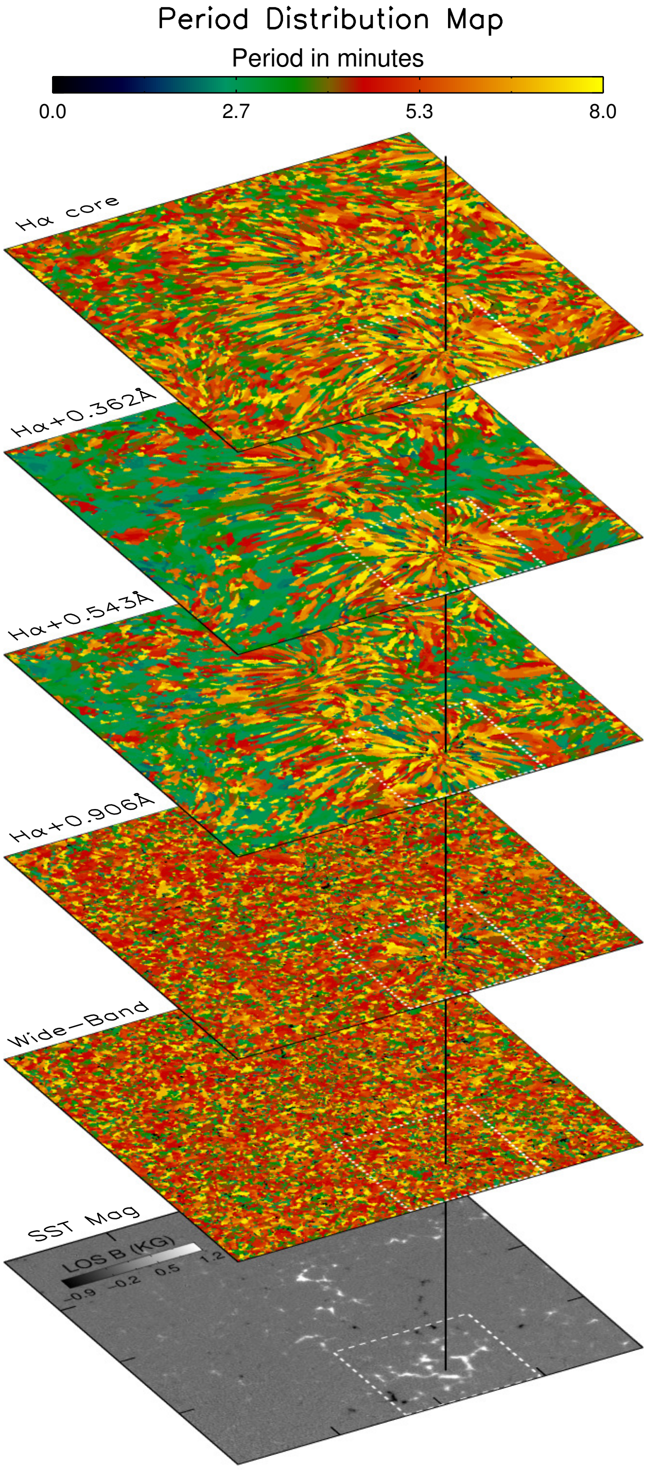

FIGURE 3.3: Distribution of dominant periods in different layers along with the corresponding magnetogram at the bottom. The green, red, and yellow colors roughly represent periods around 3, 5, and 7 minutes, respectively.

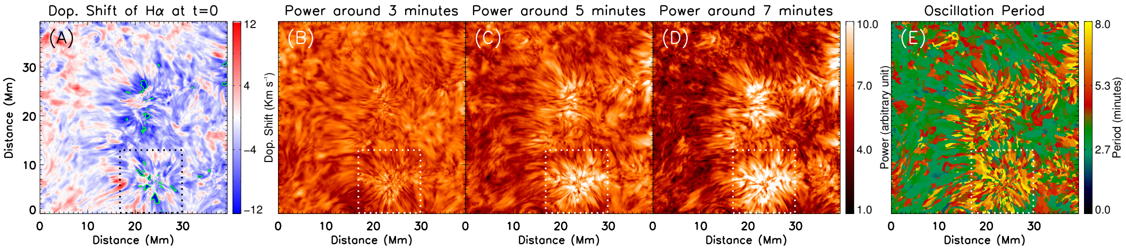

FIGURE 3.4: (A): Hα Doppler shift map (at t=0) obtained using the center-of-gravity (COG) method. The display scale is saturated to ±12 km $s^{-1}$ for better view. The value inside the green contours correspond to higher than ±12 km $s^{-1}$. The powermaps at different period bands are shown in panels (B)-(D). (E): Distribution of the dominant periods.

### 3.2.2 Spatially resolved power distributions in different period bands

We investigate the oscillation properties of the different layers by constructing powermaps. The construction of the powermaps was preceded by the removal of a background trend from each lightcurve to obtain the relative percentage intensity variations ($I_R$) given by $I_R = (I - I_{bg}) * {I_{bg}}^{-1} * 100$, where $I$ is the original intensity and $I_{bg}$ is the background trend. The background trend, $I_{bg}$, is computed from the original lightcurve over a 600 s running average, which when subtracted from the original time series allows intensity fluctuations shorter than 10 minutes to be more readily identified. The resultant lightcurves are then subjected to wavelet analysis (Torrence and Compo 1998) and the global wavelet power spectrum is calculated at each pixel. An example of the computed relative intensity variations and the corresponding wavelet analysis results at a single pixel is shown in Figure 3.5. Powermaps were constructed for 3, 5, and 7 minute periods from the global wavelet power spectrum by averaging the power in a one-minute bands around each period. Figure 3.2 displays these maps stacked in ascending order of atmospheric height for each band. A co-spatial photospheric magnetogram is also shown at the bottom panel for comparison. Figure 3.2 reveals that power is suppressed in rosettes over the network in the 3-minute band at the lower chromosphere (Hα + 0.543 and Hα + 0.362 Å) and enhanced close to the photosphere (Hα + 0.906 Å) in all the bands. These phenomena are known as magnetic shadows (Judge *et al.* 2001; McIntosh *et al.* 2003; Moretti *et al.* 2007; Vecchio *et al.* 2007; Kontogiannis *et al.* 2010b, 2014) and power halos (Kontogiannis *et al.* 2010a), respectively.

We also make period maps to study the spatial distribution of dominant periods in each layer. The period at maximum power above the 99% significance level is taken as the dominant period at each pixel to construct these maps. The significance levels are calculated assuming white noise (Torrence and Compo 1998). The period distribution maps are shown in Figure 3.3 along with the photospheric magnetogram. As in Figure 3.2 and 3.3, only the maps produced from the red wings of H$\alpha$ are displayed since the blue-wing maps look very similar. It is evident from the figure that in the layers dominated by the photosphere (wide-band and H$\alpha$ + 0.906 Å), the well-known 5-minute photospheric *p*-mode oscillation is dominant. At larger heights (H$\alpha$ + 0.543 and H$\alpha$ + 0.362 Å), the 3-minute period becomes dominant for most of the FOV, with the exception of the neighborhood of the network magnetic element where the longer (5 - 7 minutes) periods become dominant. The distribution of periods (see Figure 3.4 E) in the H$\alpha$ Doppler velocity maps show that the 3-minute oscillations cover a wider extent than that in the corresponding period-maps computed from the H$\alpha$-core intensity (see Figure 3.3). This behavior was observed earlier by De Pontieu *et al.* (2007). The velocity powermaps at different period bands are also shown in Figure 3.4 (B)-(D). It shows enhanced power in the higher period-bands around the network and suppressed power at a lower period band (3-minute) at the same region. Power/period- maps were also generated using fast Fourier transform (FFT) techniques. No significant differences were found when compared to our wavelet results, and hence to avoid duplication we do not include these figures here.

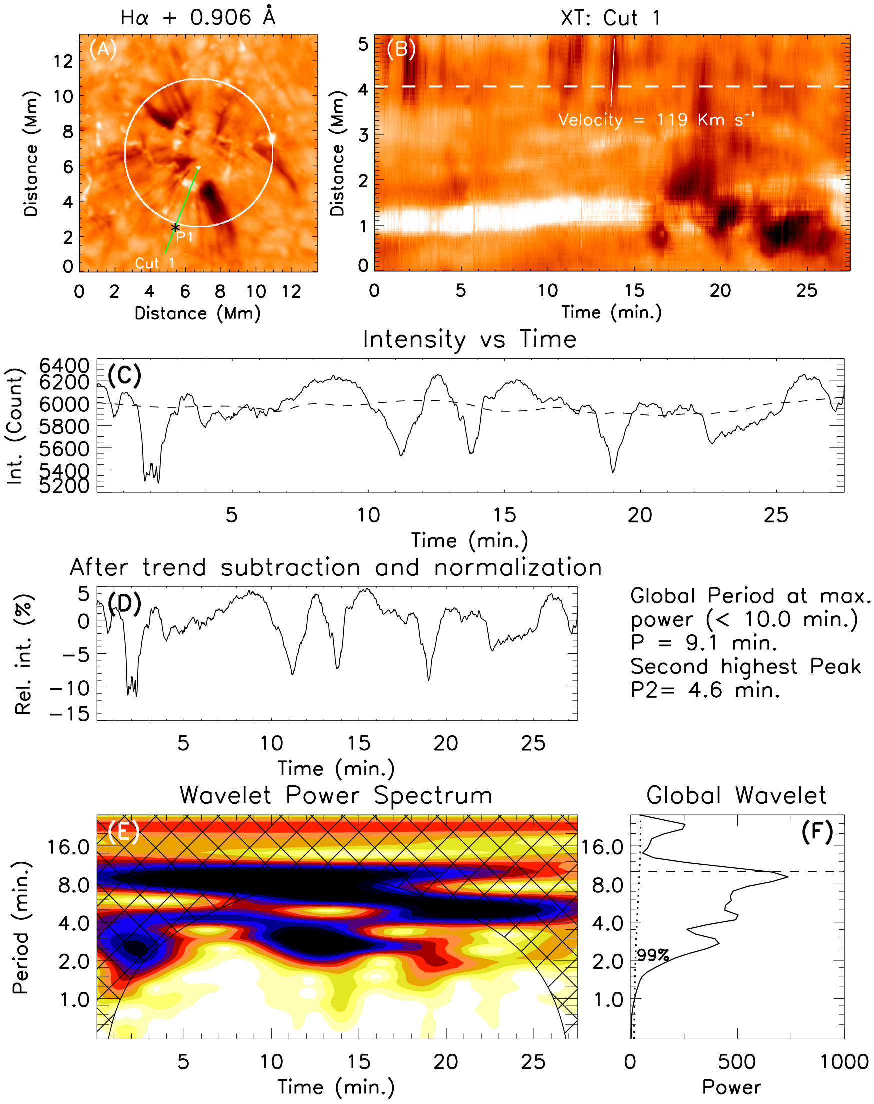

FIGURE 3.5: (A): Hα + 0.906 Å image. A cut along the green line is taken to produce the space-time map shown in (B). The white dot represents the starting point. (B): Temporal evolution along the green line shown in (A). The dashed line corresponds to the position P1 marked by an asterisk in (A). The slanted solid line indicates the track used for measuring the propagation speed. (C): The intensity variation along the dashed line in (B). The overplotted dashed line represents the background trend. (D): Relative intensity variation after trend subtraction and normalization. (E): The wavelet power spectrum of the normalized time series. The overplotted cross-hatched region is the cone-of-influence (COI) with darker color representing higher power. (F): Global wavelet power spectrum. The maximum measurable period, 10 minutes (due to COI), is shown by a horizontal dashed line. The dotted curve shows the 99% significance level. The two most significant periods identified from the global wavelet power spectrum are printed on top of the global wavelet plot. An animation of panel (A) for a bigger field-of-view and also for Hα blue wing (Hα - 0.906 Å) is available online.

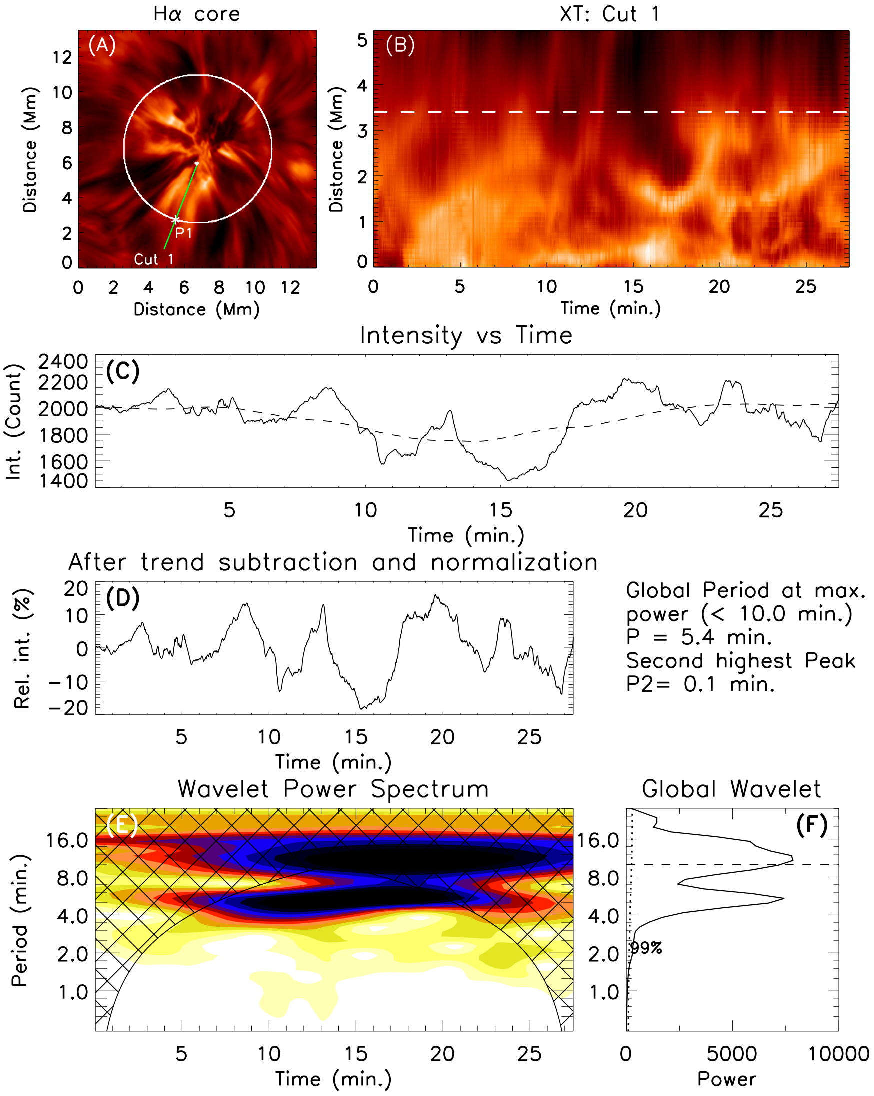

FIGURE 3.6: (A) Hα core image. Other panels are similar to those in Figure 3.5.

### 3.2.3 Space-Time Plots and Wavelet Analysis

We have generated space-time plots to study if the compressible periodic disturbances are propagating along the elongated structures in the network region. Artificial slits are placed radially outward from the center of the rosette structure as shown by a green solid line over the Hα + 0.906 Å image in Figure 3.5A. The corresponding space-time plot is displayed in Figure 3.5B and shows a few alternating dark ridges at the top. The propagation speeds calculated from the slope of one of the ridges is around 120 km $s^{-1}$. These ridges correspond to transient events like RBEs and RREs which are on-disk absorption features generally seen in the red and blue wings of chromospheric lines (Langangen *et al.* 2008; Rouppe van der Voort *et al.* 2009). Using the same data set, RBEs and RREs from this region have already been studied by Kuridze *et al.* (2015). These events have the appearance of high speed jets or blobs and are generally directed outward from a magnetic network bright point with speeds of 50 - 150 km $s^{-1}$. They can be heated up to transition region (or even coronal) temperatures with a lifetime of 10 - 120 s and are believed to be the on-disk counterparts of Type II spicules (Pereira *et al.* 2014; Kuridze *et al.* 2015; Rouppe van der Voort *et al.* 2015; Henriques *et al.* 2016). We select many locations around the network concentrations and find clear signatures of RBEs and RREs repeatedly appearing around the same place. Within $\sim$28 minutes of our observations they occur 1 - 15 times (intensity decreases $\gtrsim 1\sigma$) at the same location, with an average of 3 - 5 times. A closer inspection of the online movie shows the clear presence of such transients.

The results of the wavelet analysis for the lightcurve from the row marked by a dashed line in Figure 3.5B, corresponding to position P1 marked in panel (A), are shown in panels (C) to (F) of Figure 3.5. Panel (C) displays the original light curve (solid line) and the background trend (dashed line), while panel (D) displays the relative intensity as defined in Section 3.2.2. Panels (E) and (F) display the wavelet and global wavelet power spectra. The cross-hatched region in the wavelet plot corresponds to the Cone Of Influence (COI) where the periods identified are not reliable due to the finite length of the time series. The dotted line in the global wavelet plot corresponds to the 99 % significance level assuming a white noise (Torrence and Compo 1998). The top two periods identified are also listed in the figure. Peaks are found at 9, 4.5, and 2.5 minutes in the global wavelet power. Similar analysis performed over this region in the H$\alpha$ core shows a peak in power at 5.4 minutes (Figure 3.6). Figures 3.5 and 3.6 indicate the presence of quasi-periodic fluctuations in intensity. The fluctuations in the H$\alpha$ core are probably caused by the longer lifetime of mottles (3 - 15 minutes, Tsiropoula *et al.* (2012)).

We emphasize that we placed several slits in this region (both in the H$\alpha$ core and H$\alpha$+ 0.362 Å scan positions), and our analysis detects oscillation periods around 3 - 9 minutes. However, the nature of the ridges is not, generally, periodic but rather quasi-periodic. The dark ridges generally show high intensity drops compared to the background, which could be attributed to the outward motion of the mottles.

### 3.2.4 Standard Deviation

We also measure the standard deviation of the intensity at each pixel and construct normalized percentage standard deviation maps. The normalized percentage standard deviation (S) is estimated at each pixel by following S $= I_{std} * {I_{avg}}^{-1} * 100$, where $I_{std}$ and $I_{avg}$ are the standard deviation and average intensity, respectively. The constructed maps are shown in Figure 3.7 for different layers. It is clear that close to network regions where we observe transients like dark mottles and RBEs, the normalized percentage standard deviation is quite high. A continuous periodic oscillation of 10% amplitude (with any period) gives a standard deviation of 7%. In the figure, the green contours outline the regions with a normalized percentage standard deviation of 10 % or more.

### 3.2.5 Artificially Generated Time Series and Their Wavelet Analysis

In this subsection we explore the signatures that will be produced in the power spectrum of a bursty signal. Suppose the observed variations in intensity are due to transient phenomena like RREs and mottles. We find that RREs lower the intensity by 5 - 30 % below the background and have a lifetime of 10 to 120 s. Chromospheric mottles live for 3 - 15 minutes (Tsiropoula *et al.* 2012)

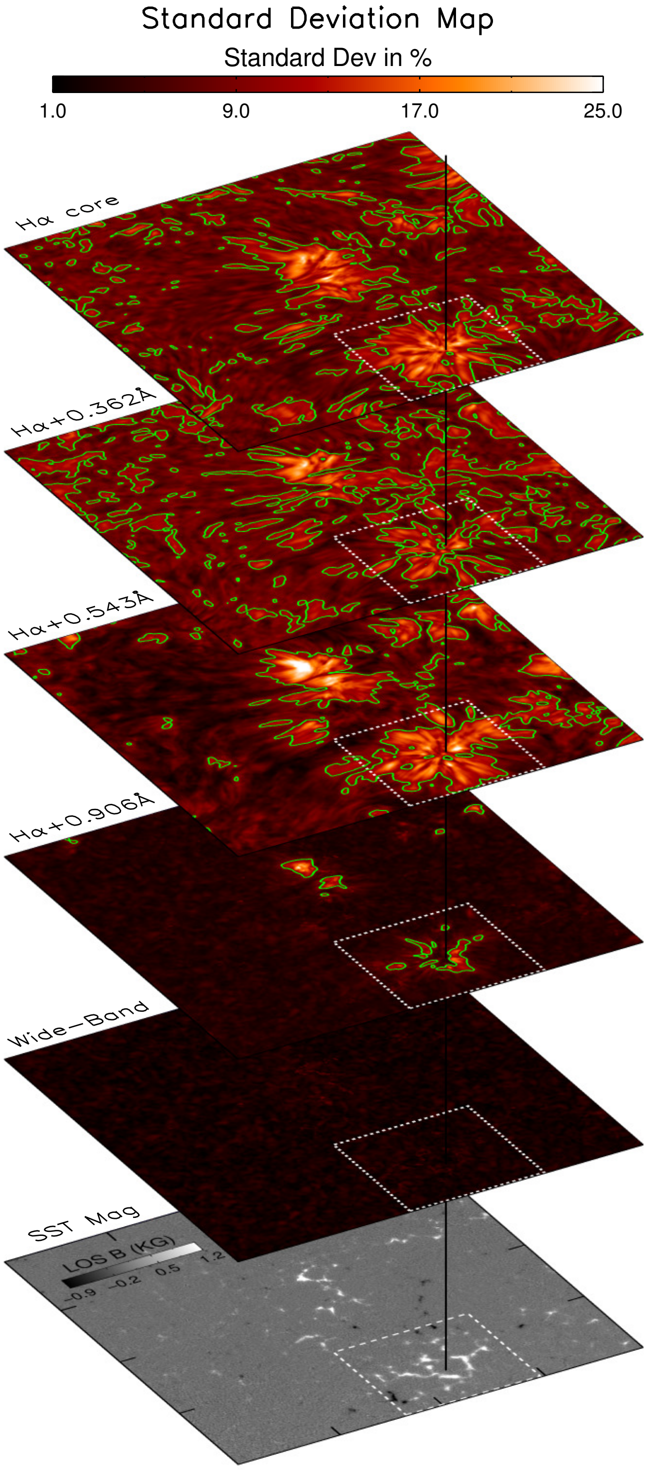

FIGURE 3.7: Standard deviation maps in different layers constructed from the normalized percentage standard deviation of the intensity time series at each pixel. The corresponding magnetogram is also shown at the bottom. The green contours enclose regions with a standard deviation of 10% or more.

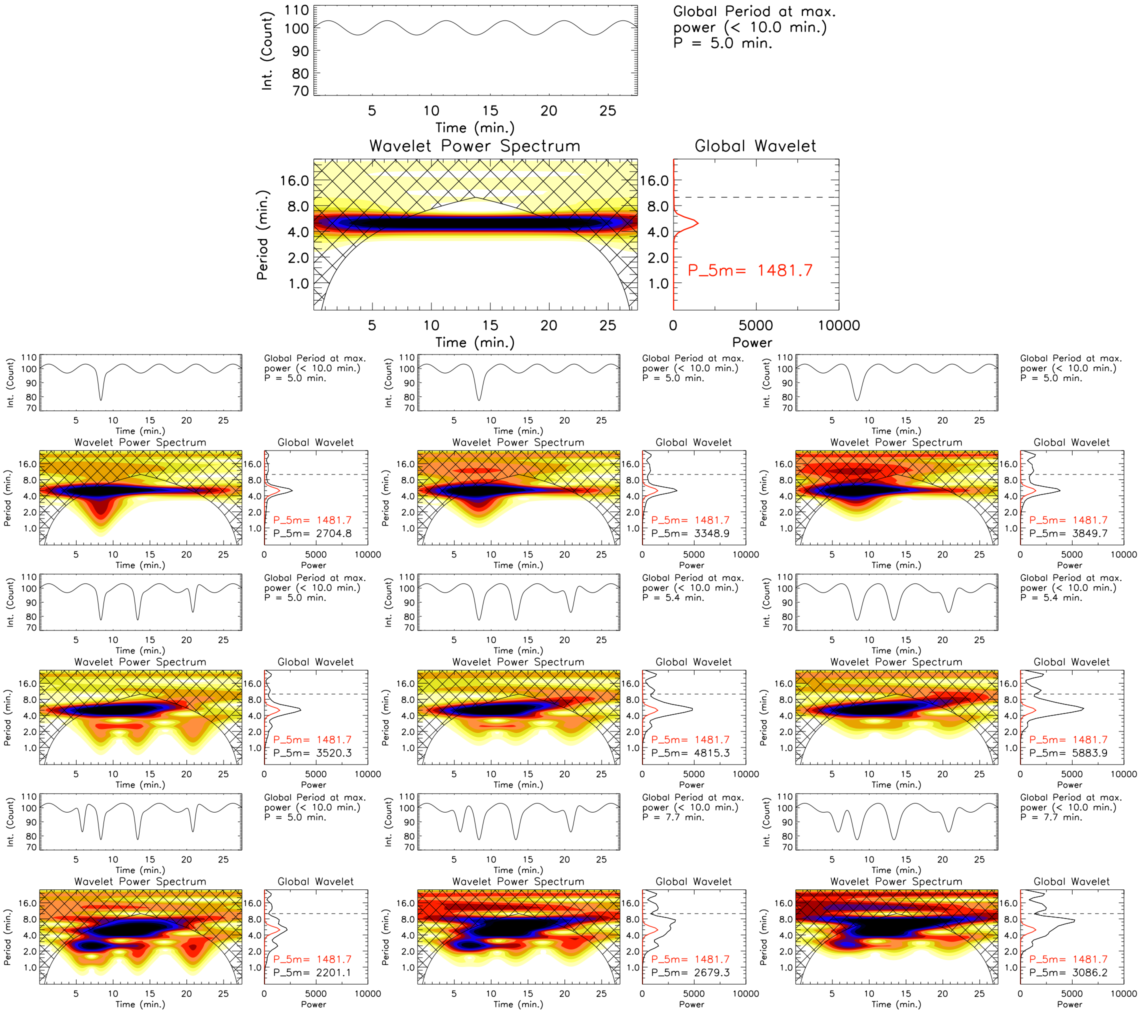

FIGURE 3.8: Results of the wavelet analysis for the artificially generated ligthcurves. Description of different panels is similar to that in Figure 3.5. Top panel: wavelet analysis results for a lightcurve with a periodic sinusoidal signal of 5 minutes. Other panels: wavelet analysis results for several ligthcurves artificially generated by convolving Gaussian-shaped dips in intensity with the periodic signal shown in the top panel. The convolved dips are randomly separated in time with the repetition times of 1, 3, and 4 across different rows. The FWHM of the dips has been kept at 40, 60, and 80 s across the three columns. The amplitudes of the sinusoidal wave and the Gaussian dips are kept at 3.2 % and 20%, respectively, to a constant background.

and cause a decrease in intensity of 10 - 50 %. Here, we have generated artificial time series to investigate the affect of non-periodic signals superimposed upon background oscillatory phenomena (e.g., as captured in our observation). Our main motivation is to compare the oscillation power between the network regions (where RBEs, RREs, and mottles are present) and the internetwork regions. We have considered two different cases: the first case models the effects of transients on the power of photospheric wavelength channels, whereas the second case models the impact of transients on the power obtained from chromospheric channels.

Case-1 (photospheric channels): first, we have generated an artificial time series using a sinusoidal signal with a 5-minute period, which we found to be the dominant period in the photosphere (it is also well known). We found that the average normalized percentage standard deviation in the photospheric internetwork regions is ∼2.25 % (see Figure 3.7). In order to match with the observed normalized percentage standard deviation, we have selected the amplitude of the sinusoidal periodic signal to be 3.2 % with respect to a constant background (ignoring all the noise and other high- and low-frequency fluctuations). We then performed wavelet analysis on this artificial signal to compute the global wavelet power spectrum as a reference, which is shown in the top panel in the Figure 3.8. This was followed by introducing random fluctuations in the same 5 minute periodic signal. The repetition and the amplitudes of the random fluctuations were selected such that they can mimic the observed lightcurves (an example of the observed lightcurve is shown in Figure 3.5). We find that many of the RREs show intensity drops between 10 and 25% compared to the background intensity whereas some of the weak and strong RREs have intensity, drops of less than 5% and more than 30%, respectively. They generally occur repeatedly at the same location (close to the network) with an average of 3 - 5 times in ∼28 minutes. Keeping in mind the observed distribution of the transients (RREs), we have produced lightcurves while introducing sudden fluctuations (Gaussian-shaped dips) with random repetitions (1 - 5 times) in the same 5-minute periodic signal. We generated 45 lightcurves while changing the amplitudes (10%, 20%, and 30%) and temporal width (FWHM of 20, 40, 60, and 80 s) of the Gaussian-shaped dips. We then subjected these modified lightcurves to wavelet analysis for computing the power spectra. Some representative examples (only for the Gaussian dips of intensity amplitudes drops of 20% with 1, 3, and 4 time repetitions and FWHM of 40, 60 and 80 s) are shown in the Figure 3.8. We compare the power of 5 minutes oscillation of the reference periodic signal (P_5m in red) with the power of the same signal with fluctuations (P_5m in black). Our analysis shows that the power of the 5-minute period is enhanced 1.1 - 6.8 times due to the presence of RBE-like random fluctuations in the intensity and lifetime. The enhancement in power is dependent on the amplitude, temporal width, repetition, and also on the temporal location (phase) of the Gaussian dips. We should point out that we have compared the observed 3-minute power between the regions of enhanced power (network) and internetwork regions in H$\alpha$ + 0.906 Å and find that the the enhancements in power is around 2 - 5 times compared to the internetwork regions. Additionally, we find that the power in the period band of 2 - 9 minutes is enhanced which is similar to the observed power distribution.

Case-2 (chromospheric channels): similarly to the first case, we have generated an artificial time series with a periodic sinusoidal signal of period 3 minutes. Here we selected the period of the oscillation to be 3 minutes as the chromospheric internetwork regions (H$\alpha$ + 0.362 Å) are dominated by a 3-minute period. As before, to compare with the observations, we have selected the amplitude of the sinusoid to be 10% (we find the average normalized percentage standard deviation is $\sim$ 7.4% in the internetwork regions of H$\alpha$ + 0.362 Å layer) with respect to the background. We find that the intensity drops in the H$\alpha$ + 0.362 Å due to the presence of mottles is around 10 - 50%. We have produced twenty seven lightcurves while introducing random fluctuations (1 - 3 Gaussian dips distributed along the whole time series) by changing the amplitudes (20, 30, and 40%) and temporal width (FWHM of 3, 5 and 7 minutes) followed by wavelet analysis to

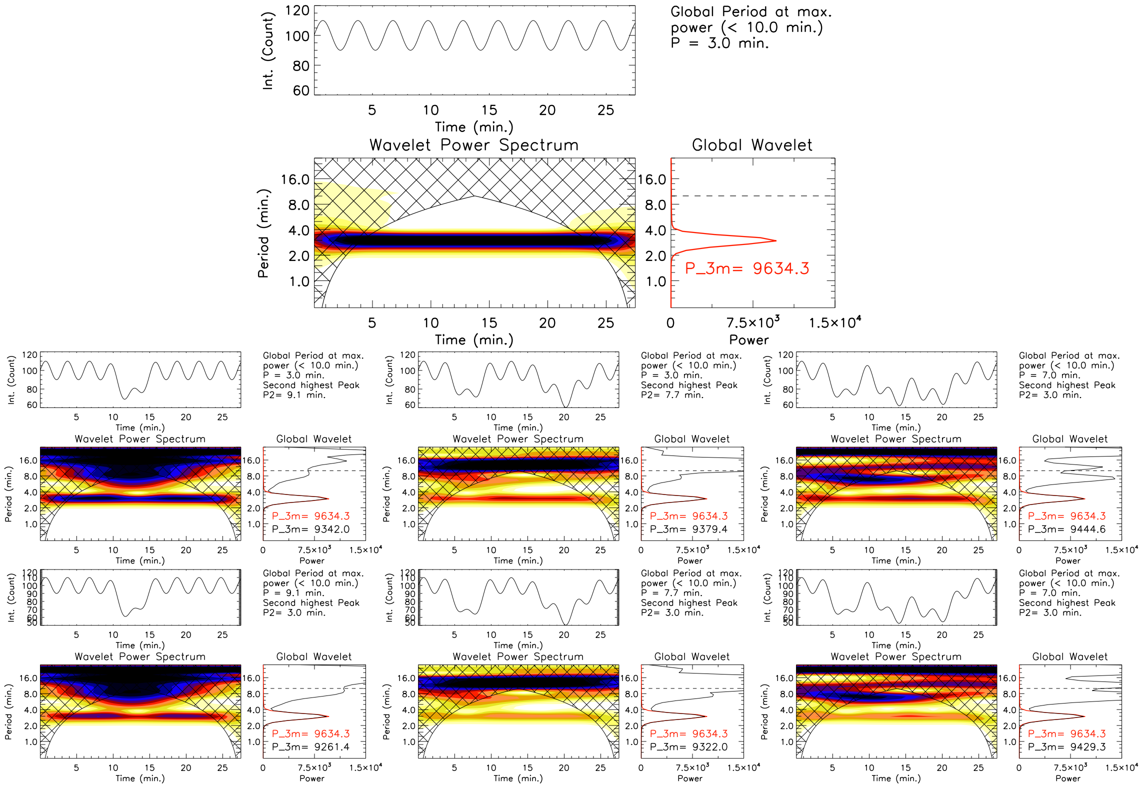

FIGURE 3.9: Results of the wavelet analysis for the artificially generated ligthcurves. Description of different panels is similar to that in Figure 3.5. Top panel: wavelet analysis results for a lightcurve with a periodic sinusoidal signal of period 3 minutes. Middle panels: wavelet analysis results for several artificially generated lightcurves made by convolving Gaussian-shaped dips of FWHM 3 minutes; 3 and 5 minutes; 3, 5, and 7 minutes, with the periodic signal shown in the top panel. The amplitudes of the sinusoidal signal and the Gaussian-shaped dips are kept at 10 % and 30 % with respect to the background, respectively. Bottom panels: same as the middle panels but for a 40 % amplitude of the Gaussian-shaped dips with respect to the background.

compute the power. A few examples (for the Gaussian dips with amplitude of 30 and 40% only) are shown in Figure 3.9. We compare the power of the 3-minute oscillation of the pure periodic signal (P_3m in red) with the power of the same signal with fluctuations (P_3m in black). Our analysis shows that the power of the 3 minute period gets suppressed 2 - 6% (though the observed magnetic shadow region show around a 60 - 70% decrease in the power of the 3-minute oscillation compared to internetwork regions) due to the presence of random fluctuations like mottles. We also noticed that the power in the period band of 5 - 9 minutes is generally enhanced due to this kind of sudden fluctuation. Hence, a sudden drop

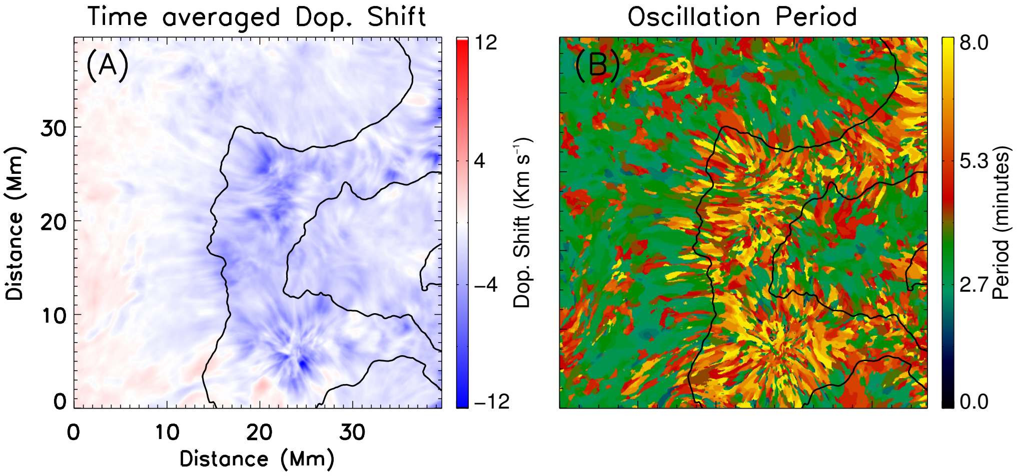

FIGURE 3.10: (A): Time-averaged Doppler velocity map of H$\alpha$ line. (B): Distribution of dominant periods in Doppler velocity oscillations. Contours on both plots represent a dominant period level of 4.5 minutes. The contours are calculated after smoothing the image in panel (B).

in intensity with a random distribution in time can lead to significant power at different periods. One important thing to note here is that the periods mainly depend on the distribution of the intensity drops and they are generally longer than their FWHM. We should point out that sometimes the power gets enhanced depending on the phase of the Gaussian dips with respect to the continuous 3-minute periodic sinusoid.

### 3.2.6 Time-Averaged Doppler Shift and Material Outflows.

The time-averaged Doppler velocity provides very important information on the statistical properties of the dynamics. Figure 3.10A shows the time-averaged Doppler velocity map of the whole FOV. The overplotted contours outline a region with a dominant periodicity of 4.5 minutes as shown in the period-distribution map (Figure 3.10B). It can be seen that within this region, above the network, the average Doppler velocity is blue shifted ($\sim$ 5 km s$^{-1}$).

The evolution of a portion of the network region is shown in Figure 3.11. The white

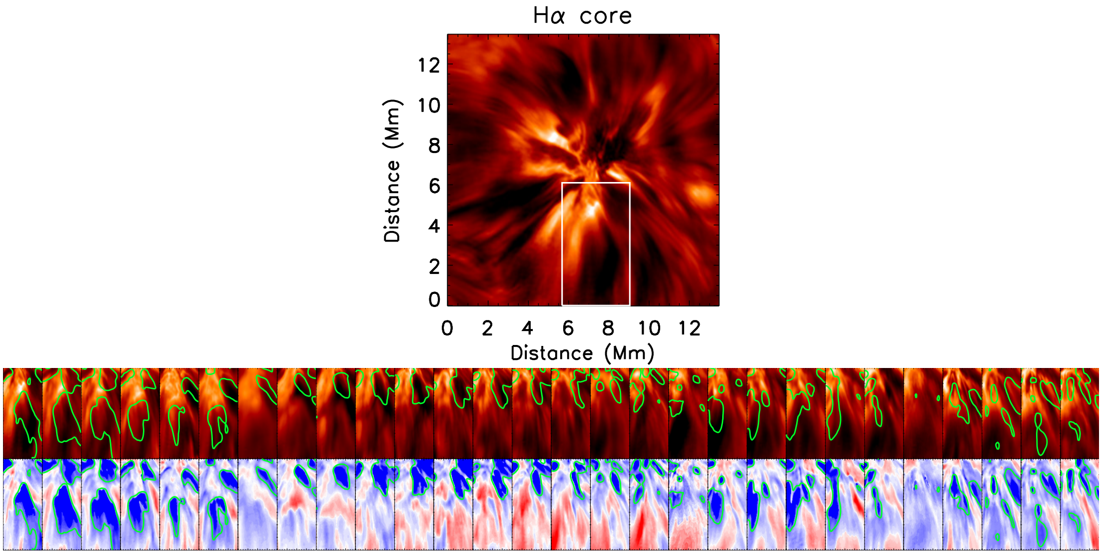

Figure 3.11: Top panel: the white rectangular box marks our region of interest. Bottom panels show the time evolution of the portion inside the white rectangular box covering a few dark mottles. The top and bottom rows display the intensity and Doppler velocity in H$\alpha$ core. Each frame is separated by a 1 minute interval. Green contours on the intensity correspond to -6 km s$^{-1}$ Doppler velocity.

box marked in the left panel is our region of interest for temporal variations. The upper panels display the intensity and the bottom panels display the Doppler velocity as captured in one-minute intervals. This figure shows that when dark mottles first start appearing, they are blueshifted but with time the mottles evolve and become bright and redshifted. It is possible that mottles are nothing but strong material outflows like Type I spicules. They appear similar to Type I spicular flows following parabolic paths. The material moves outward, causing a blueshift which turns to redshift when the material falls back on the solar surface.

## 3.3 Discussion

As pointed out in the introduction, the interaction between acoustic waves and the magnetic field are responsible for the formation of magnetic shadows and power halos (Judge *et al.* 2001; McIntosh *et al.* 2003; Moretti *et al.* 2007; Vecchio *et al.* 2007; Kontogiannis *et al.* 2010b, 2014). Using Dutch Open Telescope H$\alpha$ observations with a cadence of 30 s, Kontogiannis *et al.* (2010a,b) pointed out that there is a strong possibility that power at longer time periods ($\sim$7 minutes) may be enhanced as a result of the lifetimes of the mottles. Furthermore, Kontogiannis *et al.* (2010a) also highlighted that the observed power enhancements, at both photospheric and chromospheric heights, may be closely related to the temporal dynamics of such transients and their lifetimes. In this paper we have explored if transients can influence the power distribution at different heights. The high-cadence (1.34 s) observations presented here allow us to identify and study the dynamics of transient phenomena in greater detail, which was previously not possible due to lower cadence ($\sim$30 s).

The quiet chromosphere is generally dominated by numerous elongated dark structures seen in H$\alpha$. These include rapidly changing hair-like structures known as mottles and extreme Doppler-shifted events such as RBEs and RREs (for details see the review of Rutten (2012); Tsiropoula *et al.* (2012)). Figure 3.1 and its associated movie (available online) reveal that these structures are associated with the regions of network magnetic fields which appear at the edges of granular cells (Nordlund *et al.* 2009). It is now generally believed that the dark mottles are the disk counterparts of Type I spicules (Tsiropoula *et al.* 1994b,a; Tsiropoula and Schmieder 1997; Christopoulou *et al.* 2001) and the RBEs are the disk counterparts of Type II spicules (Langangen *et al.* 2008; De Pontieu *et al.* 2011; Pereira *et al.* 2012; Kuridze *et al.* 2015). The mottles seen in the H$\alpha$ line have mean velocities of the order of 20 - 40 km s$^{-1}$ and lifetimes of 3 - 15 minutes (Tsiropoula *et al.* 2012). On the other hand, the transients like RBEs and RREs generally exhibit upward motion and rapidly fade away without any signature of downward motion. They have shorter lifetimes (10 - 120 s), high apparent velocities (50 - 150 km s$^{-1}$), and smaller widths (150 and 700 km) (Kuridze *et al.* 2015).

Tziotziou *et al.* (2003) found that mottles arise at the network boundaries as bursts of material and propagate upward with a velocity around 25 km $s^{-1}$. They also show a tendency to occur several times at the same place with a typical duration of around 5 minutes. Our analysis also indicates that the mottles are jet-like features originating in the network region that propagate upward. Figure 3.11 shows that the footpoints of mottles display strong blue-ward shift when they originate, but with time they fade away and small redshifts are observed that likely correspond to material falling back along the magnetic-canopy structures are observed. The average blueshift above the network (see Figure 3.10) indicates that material outflows are present in that region. These outflows are not as strong as they are in individual time frames (see Figure 3.4), suggesting that outflows are not continuous but rather quasi-periodic in nature. The normalized percentage standard deviation in the photosphere, where 5-minute $p$-modes dominate, is low (around 2.25 %) but above the network regions where the RREs and mottles are seen, is quite high (above 10%, see Figure 3.7). Higher values of normalized percentage standard deviation cannot be explained solely by the presence of linear MHD waves (observations show that the slow waves generally have an amplitude of less than 5 % (Wang 2011)). Numerical models show that the dark mottles observed in H$\alpha$ are due to material density enhancement (Leenaarts *et al.* 2006, 2012). So, the fluctuations caused by the rise and fall of material in the form of transients may be responsible for the observed high standard deviation.

Power halos (across all period bands) manifesting in the predominantly photospheric bandpass (H$\alpha$ + 0.906 Å) can be explained due to the occurrence of Doppler-shifted transients like RBEs and RREs. The associated online movies clearly show the presence of these transients, particularly in the neighborhood of the network field concentrations. Although not strictly periodic, they occur repeatedly (3 - 15 times in 28 minutes) at the same location and have a lifetime of 10 - 120 s. Hence, the lifetime and distribution of Doppler-shifted RBEs (see Figure 4 of Sekse *et al.* (2013)) can produce sufficient power enhancement in different periods, as shown from the artificial lightcurves that corresponds to "case-1" from Subsection 3.2.5 as demonstrated in Figure 3.8.

Imaging data from a passband centered at 0.7 Å from the H$\alpha$ line core was used to produce the powermaps where quiet-Sun "power halos" were positively identified (Kontogiannis *et al.* 2010a,b, 2014). This is closer to the H$\alpha$ line core when compared to the predominantly photospheric bandpass at +0.9 Å. Thus, we believe that these previous power-halo detections were more affected by Doppler-shifted transients than our observations and simulations, firmly setting Doppler-shifted transients as the source of the observed halos in the quiet Sun. Note that in our wide-band powermaps we do not find significant power enhancement at the regions of halos as observed in the H$\alpha$ + 0.906 Å. This confirms the earlier report by Vecchio *et al.* (2007) who also did not find signatures of power enhancements in the photospheric broadband continuum band (centered at 710 nm) close to network regions. There is no reason that power-halos should not be observable in wide-band data as they are photospheric. There should be no difference between narrow-band observations at purely photospheric wavelengths and wide-band observations with respect to wave detection. The effective difference we find between the two is the impact of the Doppler-shifted chromospheric transients.

Similarly, we believe that power from random transients could affect the light curves and influence the power distribution. More generally, the presence of transients can leave a two-dimensional signature visible in powermaps obtained in a similar fashion. One such example is "network aureoles", a structure similar to the power halos in the upper photosphere/lower chromosphere as reported in Krijger *et al.* (2001) . This effect by transients should be present in the active region power halos as well even though it may be less important in a more stable canopy and stronger wave signal. The powermaps are strongly affected close to the network regions where jets are occur ubiquitously. In the context of EUV coronal bright points, Samanta *et al.* (2015a) have demonstrated that the quasi-periodic oscillation in transition regions and corona above a network regions are due to repeated occurrences of jets around the network regions.

Similarly to the power halos, the magnetic shadow seen closer to the line core (H$\alpha$ + 0.543 and H$\alpha$ + 0.362 Å) in the 3-minute power band can be affected by the lifetime and distribution of the mottles. It is generally seen that, close to network regions, power above 5 minutes dominates whereas in the internetwork regions, the dominant period is 3 minutes (Dame *et al.* 1984; Deubner and Fleck 1990; Bocchialini *et al.* 1994; Cauzzi *et al.* 2000; Krijger *et al.* 2001; Tsiropoula *et al.* 2009; Gupta *et al.* 2013; Bostancı *et al.* 2014). The H$\alpha$ core-intensity signal (see Figure 3.3) is mostly dominated by $\geq$5-minute oscillations over the entire FOV, whereas the Doppler velocity signal (see Figure 3.4) shows a $\geq$5 minute dominant period very close to the network region and 3-minute in the internetwork region. Similar behavior was also found by De Pontieu *et al.* (2007). The reason for this could be that, close to the network center, when the mottles travel upward, we observe blueshifts from material flowing toward the observer, but when these reach the magnetic canopy region, we will not be able to observe any LOS Doppler shifts as the material is flowing horizontally with a quasi-periodicity (the intensity fluctuations can still be observed). Rather, the 3-minute shocks (Carlsson and Stein 1992, 1997), buffeting the canopy from below in the internetwork region, are observed in the Doppler signal. Hence, the lifetime of mottles will not affect the Doppler power map. The high intensity fluctuations produced by the appearance and disappearance of mottles cause greater power at longer periods, instead of at 3 minutes. We should point out that Kontogiannis *et al.* (2014) conjectured that the nature of the 7-minute power at the chromospheric heights is not acoustic in nature. Using our simplistic model we tried to mimic the chromospheric power distribution and we find that the suppression of power in the 3-minute period band due to sudden fluctuations (like mottles) is only a few percent (2 - 6%) whereas the same fluctuations can highly influence longer-period (5 - 9 minutes) power. Our analysis indicates that the observed long-period oscillation in the H$\alpha$ core and close to the network in H$\alpha$ + 0.362 and H$\alpha$ + 0.543 Å (see Figure 3.3) arises due to the longer lifetime of the mottles in the quiet-Sun network regions. From our observations we find that the magnetic shadow regions (network) show 60 - 70% power reduction compared to the internetwork regions. So, we conclude that although the power can be affected by the lifetime of the mottles, the power suppression due to mottles may not be significant in the 3-minute period. Hence, we conjecture that wave mode conversion may play a key role in forming magnetic shadows in the 3-minute power-band. The slow waves may transfer part of their energy upon reaching the canopy layer and convert to fast magnetoacoustic modes. Due to high velocity gradients, the fast mode generally reflects back and forms magnetic shadow (Khomenko and Collados 2006; Schunker and Cally 2006). In addition to this process, Rijs *et al.* (2016) found that fast-to-Alfvén wave mode conversion may play an important role in this process and the the fast wave energy can be converted to transverse Alfvén waves along the field lines. We should also point out that most of the theoretical work on the magnetic portals have not included the non-LTE effects, which may play an important role in the coupled chromosphere where radiation effects are also important.

## 3.4 Conclusions

We studied the oscillatory behavior of the quiet Sun using H$\alpha$ observation encompassing network bright points. The powermaps at different layers display the well-known “magnetic shadow” and “power halo” features. Previously, these phenomena were interpreted in terms of acoustic waves interacting with inclined magnetic fields. We show that powermaps in general can be strongly affected by the lifetimes of these transients. We propose that transients like RBEs, which occur ubiquitously in the solar atmosphere, can have a major effect on the formation of power halos in the quiet Sun. For magnetic shadows in the 3 minute band, the mode conversion seems to be most effective, whereas the power at longer periods is highly influenced by the presence of mottles. We should point out that the shorter time length of the time series will also have some effect on the power analysis. A very long time series should ideally be used for such purposes but high quality ground-based observations are rarely available for prolonged periods. Most of the previous low cadence observations and numerical simulations have ignored the effects of small-scale transients while explaining the magnetic portal. Our high-cadence observations reveal clear presence of these transients and thus waves and transients may simultaneously be present within these structures and can collectively cause the power enhancements and suppression. It will be very difficult to isolate and decouple these effects, although the dominant source for the formation of power halos appears to be the transients from our observation. We hope to quantify the contributions from these two sources in our future work, while studying the phase relation between intensity and velocity at different layers. With high spatial and temporal resolution observations we find that the quite-Sun chromosphere is highly dynamic, where flows, waves, and shocks manifest in the presence of the magnetic field to form an often nonlinear MHD system and future simulations should include all these effects.

# Chapter 4

# Source of quasi-periodic oscillations in coronal bright points[†]

## 4.1 Introduction

Coronal bright points (BPs) are bright dynamical features seen in quiet-sun and coronal holes (CHs). The dynamics and evolution were studied in X-rays and EUV wavelengths (Vaiana *et al.* 1973; Golub *et al.* 1974, 1976a,b; Habbal and Withbroe 1981; Zhang *et al.* 2001; Tian *et al.* 2008a; Zhang *et al.* 2012; Li *et al.* 2013). They generally live for a few hours to a few days and have sizes less than $50''$. BPs are believed to be composed of loops connected locally with the photospheric bipolar magnetic fields (Golub *et al.* 1976b; Sheeley and Golub 1979). With recent

---

[†] Results of this work are published in Samanta *et al.* (2015a).

All the animations that are referred to in this chapter are available at `http://dx.doi.org/10.1088/0004-637X/806/2/172` high-resolution EUV images it is clear that a BP is not a point or simple loop-like structure but looks like a miniature active region with multiple magnetic poles with several connectivities. Moreover, depending on the emergence and cancellation of the magnetic polarities, the BPs evolve with time and show a lot of dynamics. The theoretical model argues that the interaction between two opposite polarities creates an X-point magnetic reconnection that locally heats the corona and produces BPs (Parnell *et al.* 1994; Priest *et al.* 1994). The locations of BPs appear to be related to the giant convection cells (McIntosh *et al.* 2014). Zhang *et al.* (2012, 2014) suggested that small bipolar emerging magnetic loops might reconnect with an overlying large loop or open field lines and produce brightenings. They also proposed that BPs might consist of two components: one is a long-lived smooth component due to gentle quasi-separatrix layer (QSL) reconnections, and the other is a quasi-periodic impulsive component, called as BP flashes.

Sheeley and Golub (1979) reported that the BPs evolve with a 6-minutes timescale. Several observations in X-ray and EUV show periodic variation in the intensity of BPs over a broad range of periodicity (Nolte *et al.* 1979; Sheeley and Golub 1979; Habbal and Withbroe 1981; Strong *et al.* 1992; Kumar *et al.* 2011; Tian *et al.* 2008b; Kariyappa *et al.* 2011; Chandrashekhar *et al.* 2013). Some suggested that these oscillations are caused by the leakage of acoustic waves ($p$-modes), which propagate along the magnetic flux tubes and convert into magnetoacoustic mode at higher atmosphere (Bogdan *et al.* 2003; Kuridze *et al.* 2008; Srivastava and Dwivedi 2010). Others believe that the intensity oscillations are due to repeated magnetic reconnections (Madjarska *et al.* 2003; Ugarte-Urra *et al.* 2004; Doyle *et al.* 2006).

Several studies have been carried out to understand the periodic nature, but their origin remains inconclusive. Here, we study a BP inside a CH as seen in the Atmospheric Imaging Assembly (AIA) EUV coronal images and in the Helioseismic and Magnetic Imager (HMI) magnetogram and simultaneously with the newly launched Interface Region Imaging Spectrograph (IRIS). Combining imaging and spectroscopic observations, we study the dynamical changes within this BP and its variability. We show that the time variability can be explained in terms of a repeated magnetic reconnection scenario.

## 4.2 Data analysis and Results

### 4.2.1 Observation and Data Reduction

Observational data were obtained from IRIS, AIA, and HMI instruments from 5:14 to 6:34 UT on 11 May 2014. We used AIA images centered at 335 Å, 193 Å, 171 Å and 1600 Å. AIA and HMI images have $0.6''$ pixel size and were co-aligned. IRIS data were taken in sit-and-stare mode. It was pointing toward a CH (centered at $404'', -612''$). Slit-jaw images (SJIs) were available only with the 1330 Å filter. We have used IRIS Level 2 processed data, which takes care of dark current, flat field and geometrical corrections, etc. The exposure time and cadence of 1330 Å SJIs and spectra were 8 and 9.6 s, respectively. IRIS has a pixel size of $0.166''$. AIA and HMI data were then co-aligned with IRIS data. IRIS 1330 Å and AIA 1600 Å were used for co-alignment. De-rotation was performed on all AIA and HMI images to co-align the data cubes.

Figure 4.1 (a) shows the CH in the AIA 193 Å image. The magnetogram (Figure 4.1 (g)) shows that the CH is dominated by negative-polarity magnetic field (color bar can be seen in Figure 4.2). We made a 48 hr movie with AIA 193 Å images and HMI magnetograms with 1 hr cadence. It reveals that the BP appears around 16:00 UT on 10 May 2014 with emergence of some positive flux and disappears around 17:00 UT on 12 May 2014 (with a lifetime $\sim$ 38 hr) with the complete disappearance of the positive flux. The positive flux concentration within this BP

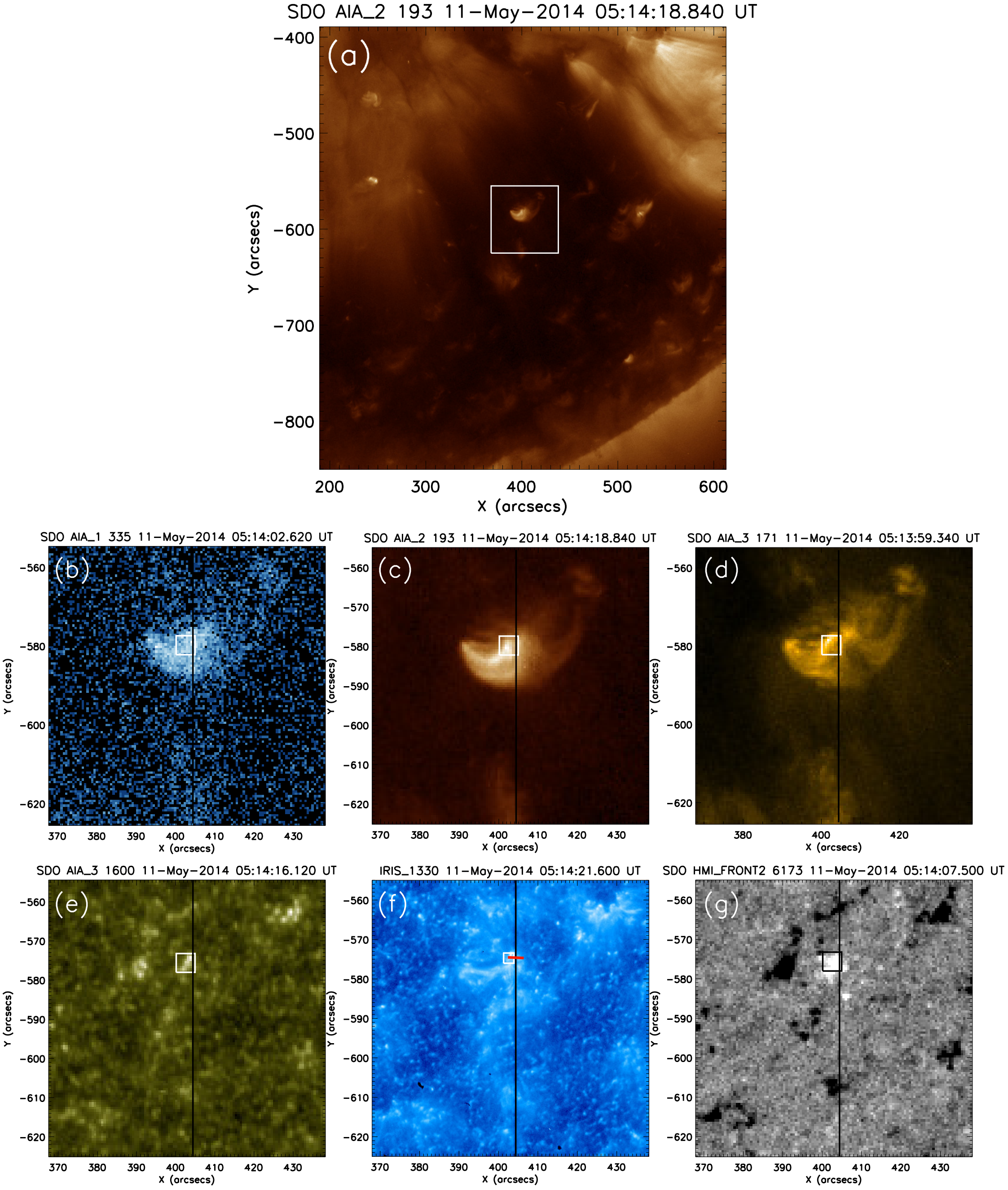

FIGURE 4.1: (a): AIA 193 Å image showing a coronal hole. The white box represents our region of interest (ROI), covering a bright point in the coronal hole. Zoomed views of the ROI as recorded by different AIA channels are shown in (b)-(e), (f) shows the IRIS 1330 Å SJI, and (g) shows the HMI line-of-sight (LOS) magnetogram. The vertical black line on each image represents the position of the IRIS slit. Intensities within the small white box of (b)-(f) are used to study oscillation properties (see Figure 4.3). The red horizontal tick marked on IRIS the 1330 Å image (f) is the location where we study the variation of different line parameters of the Si IV 1393.76 Å line (see Figure 4.4). A movie of the ROI is available online.

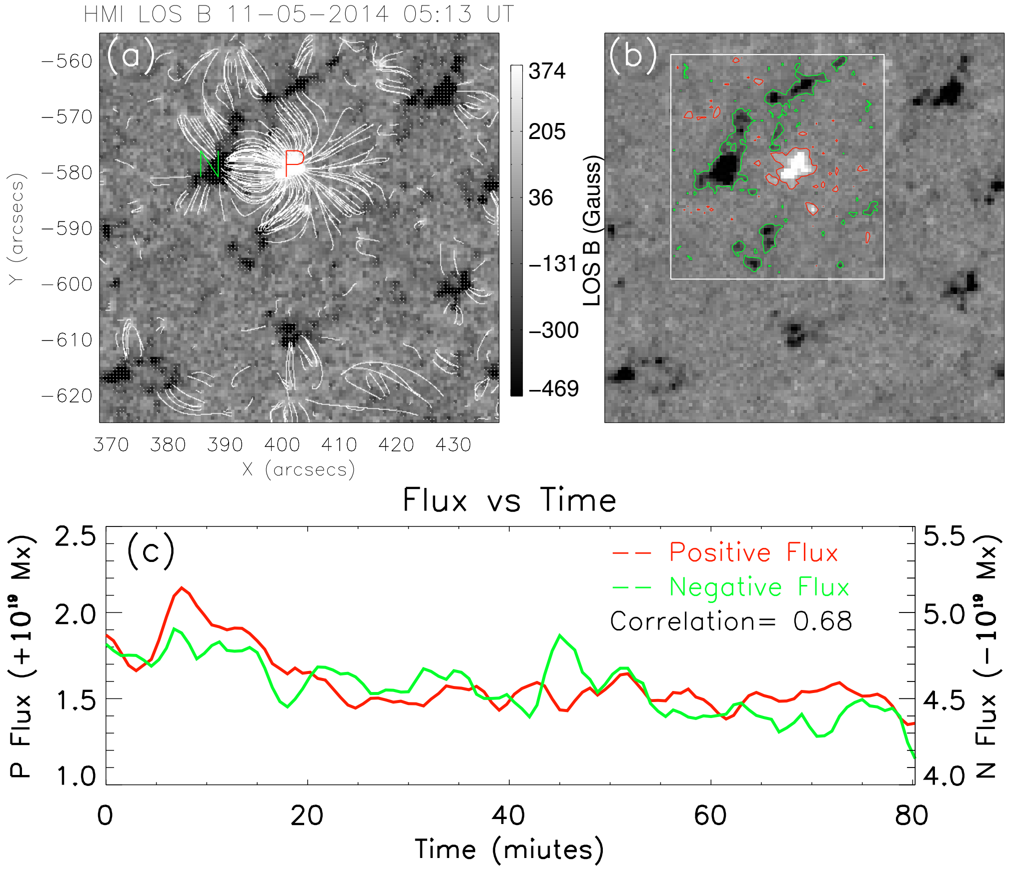

FIGURE 4.2: (a) HMI LOS magnetogram and extrapolated potential field lines (white lines). (b) On the same magnetogram the red and green contours represent the field above +20 and -20 G, respectively. The magnetic fluxes (positive and negative) are calculated within the contours (red and green, respectively) inside the rectangular white box. (c) Variation of measured positive and negative flux over time.

over the dominated background negative flux is the probable reason of the existence of the BP. Figure 4.1 shows the BP as seen in various AIA channels (b-e), IRIS 1330 Å SJI image (f), and HMI line-of-sight (LOS) magnetogram (g). The vertical black line on each image represents the position of the IRIS slit. It clearly shows that the IRIS slit is crossing one footpoint of the BP, where the magnetic field is positive.

### 4.2.2 Magnetic field evolution

Figure 4.2 (a) shows the HMI LOS magnetogram. Potential field extrapolation was performed by assuming a constant $\alpha$ force-free magnetic field (with $\alpha = 0$) (Nakagawa and Raadu 1972; Alissandrakis 1981). The white lines connecting different polarities ($\geq \pm 20$ G) represent the extrapolated field lines. Strong connectivity between primary polarity P (positive) and N (negative) can be seen. It agrees well with the intensity images as seen in IRIS SJIs and AIA images. Our ROI lies well within a CH, primarily dominated by negative flux over the entire region. Based on the main connectivity with the positive flux (P), we have selected a region marked as a white box in Figure 4.2 (b) to calculate the magnetic flux. Contours with +20 and -20 G are drawn in red and green, respectively, and fluxes are calculated within these contours. After calculating the fluxes for each time frame, smoothed over three frames, light curves (LCs) are shown in Figure 4.2 (c). There appears to be a good correlation between positive and negative flux, with a correlation coefficient (CC) of 0.68. It indicates that both positive and negative flux amplitudes vary in a similar manner. Movie 1 (available online) shows small-scale magnetic flux emergence and cancellation. It is possible that newly emerging small bipolar loops are reconnecting with the overlying preexisting large loop (P-N) as suggested by Priest *et al.* (1994) and Zhang *et al.* (2012, 2014), which could explain the good correlation. In section 4.2.4, we show signatures of reconnection and their relation with flux changes.

### 4.2.3 Imaging observations

We have focused on the dynamics of one footpoint (positive polarity P). We study the time evolution of this small region as seen with simultaneous multiwavelength images corresponding to the transition region (TR) and coronal layers. We have

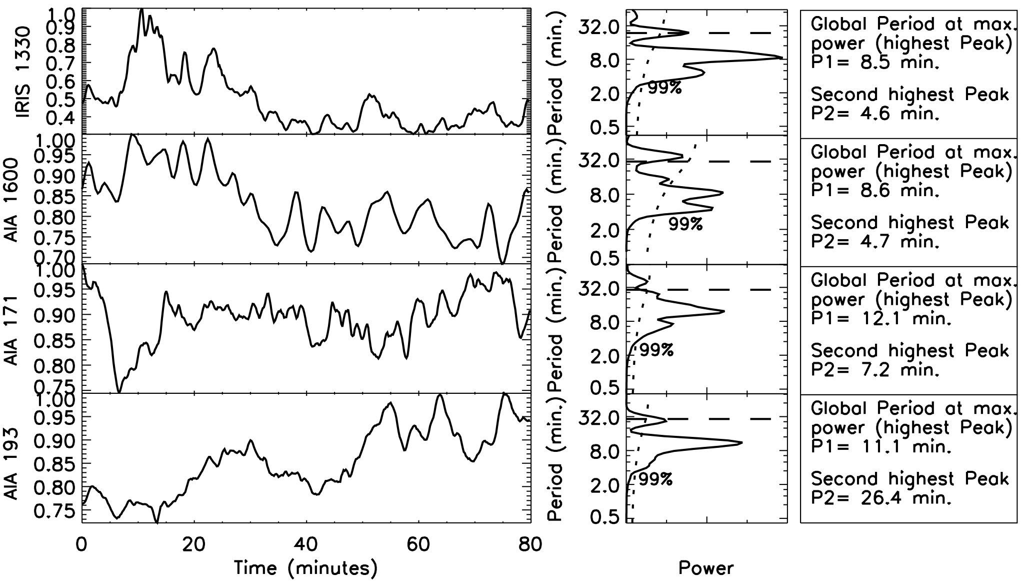

FIGURE 4.3: In each row the left panel shows the variation of intensities of different AIA and IRIS channels. The middle panel shows the global wavelet power spectrum. The confidence levels are overplotted with dashed lines. The right panels show the significant periods as measured from the global wavelet spectrum. Intensity variations of AIA images and IRIS 1330 Å SJIs are calculated from the region inside the white boxes as shown in the Figures 4.1 (b)-(f).

computed average intensities inside the small white box on top of the footpoint as shown in Figures 4.1 (b)-(f). The size of the white box in AIA was 8×8 pixel ($\sim (4.8'')^2$), and IRIS was 15×15 pixel ($\sim (2.5'')^2$). AIA box size was selected slightly larger to accommodate the loop expansion higher up and also to reduce movement effects of the loop if any. The smoothed light curves (LCs) over three time frames are shown in the Figure 4.3. Left panels show (from top to bottom) the LCs of IRIS 1330 Å and AIA 1600 Å, 171 Å and 193 Å, respectively. We have performed wavelet analysis (Torrence and Compo 1998) on each LC after removing the background trend. We use the Morlet function, a complex sine wave modulated by a Gaussian, for convolution with the time series in the wavelet transform. The global wavelet power spectra are shown in the middle panel of Figure 4.3. A confidence level of 99% is overplotted by the dotted white line. The confidence level was set by assuming white noise (Torrence and Compo 1998). Measured periods are printed in the right panels. The global wavelet power plots clearly show the presence of periodicities. A dominant period around 8 minutes is present in IRIS 1330 Å and AIA 1600 and 171 Å LCs. Though the global wavelet plots of AIA 171 Å and 193 Å show the presence of strongest peak at ∼12 minutes there is a weaker power around 8 minutes.

Now we try to explore the source of these oscillations. Several observational evidences show a positive correlation between the EUV and X-ray emission with the underlying photospheric magnetic flux (Preś  and Phillips 1999; Handy and Schrijver 2001; Ugarte-Urra *et al.* 2004; Pérez-Suárez *et al.* 2008). Preś  and Phillips (1999) have observed that X-ray and EUV emissions are temporally correlated with the photospheric magnetic flux. They also suggested the possibility of several small "network flares" occurring during the lifetime of these BPs. Chandrashekhar *et al.* (2013) have found a good temporal correlation between magnetic flux associated with the footpoints and the intensity brightening and suggested that the possibility of a repeated reconnection scenario. Note that most of these were imaging observations. In the following subsection we study the time evolution from the IRIS spectroscopic data, which provides additional information on the possible sources of these oscillations. IRIS sit-and-stare observation provides an ideal opportunity to study the time evolution of this footpoint as the slit position is crossing it.

### 4.2.4 Spectroscopic Analysis

At first, a single Gaussian fit was performed on the averaged (over all the pixels along the slit and time) profile of the photospheric S I 1401.513 Å line for absolute calibration of wavelength. Now, for our spectroscopic study, we have selected a position $(402.40'', -574.52'')$ that corresponds to one footpoint of the BP loop system. The position is marked by a red tick mark on the IRIS 1330 Å SJI in Figure 4.1 (f). An average over three pixels along the slit and a running average of three points along dispersion were applied to the spectra to improve signal-to-noise

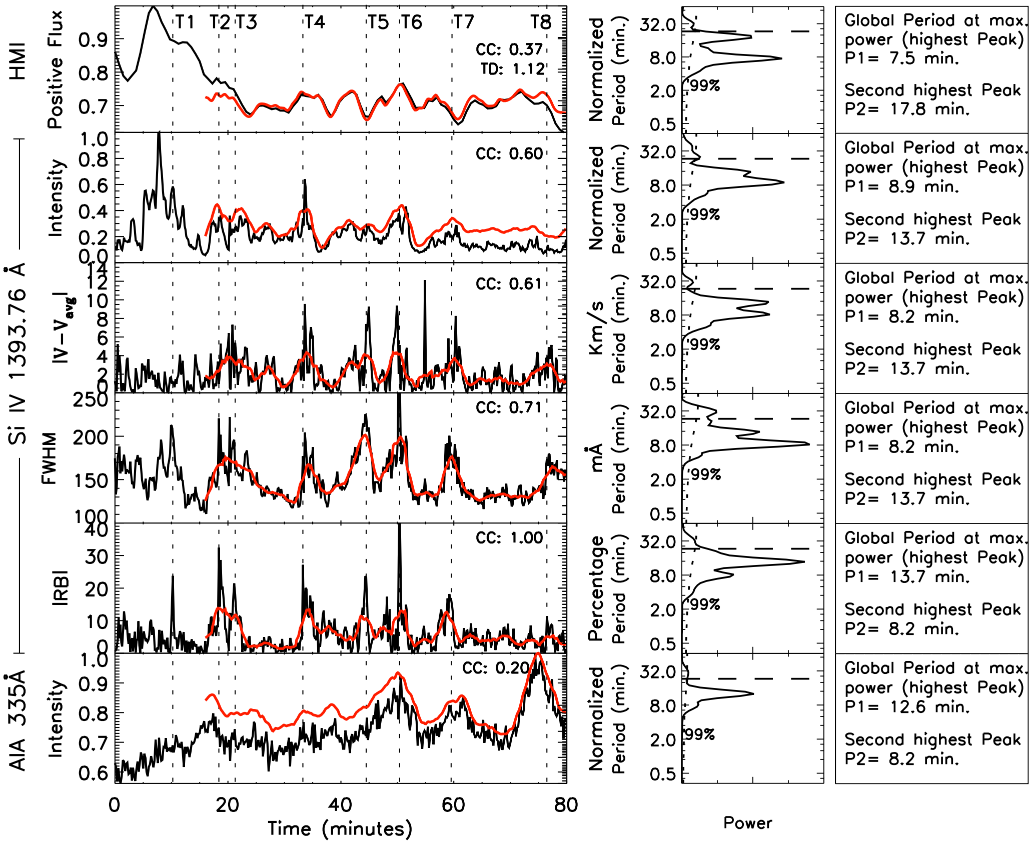

FIGURE 4.4: Similar to Figure 4.3, the top row corresponds to HMI positive flux, and the bottom row corresponds to AIA 335 Å intensity, and other rows correspond to different line parameters as calculated from the Si IV 1393.76 Å line profiles. $|RB|$ and $|V - V_{avg}|$ represent absolute RB asymmetry and the deviation from average Doppler shift, respectively, where $V_{avg}$ is the average Doppler shift. Red lines are the trend-subtracted smoothed curves for duration 16 - 80 minutes. Si IV 1393.76 Å line profiles correspond to the location as marked in Figure 4.1 (f), with the red tick mark on the IRIS 1330 Å SJI. The CC between all the LCs with the absolute RB is printed in the respective panel.

ratio. After that, a single Gaussian fit was applied to each IRIS Si IV 1393.76 Å line profile to derive line intensity, Doppler shift, and FWHM of the line. To compute the asymmetry in the line profile, we performed red-blue (RB) asymmetry analysis (De Pontieu *et al.* 2009; Tian *et al.* 2011b; Martínez-Sykora *et al.* 2011). A single Gaussian fit was performed only in the core of the profile to find the line centroid (similar to that in Tian *et al.* (2014a)). Red and blue wings were then subtracted and normalized to peak intensity to construct the RB asymmetry profile (in percentage). Finally, we have constructed the RB asymmetry LC by

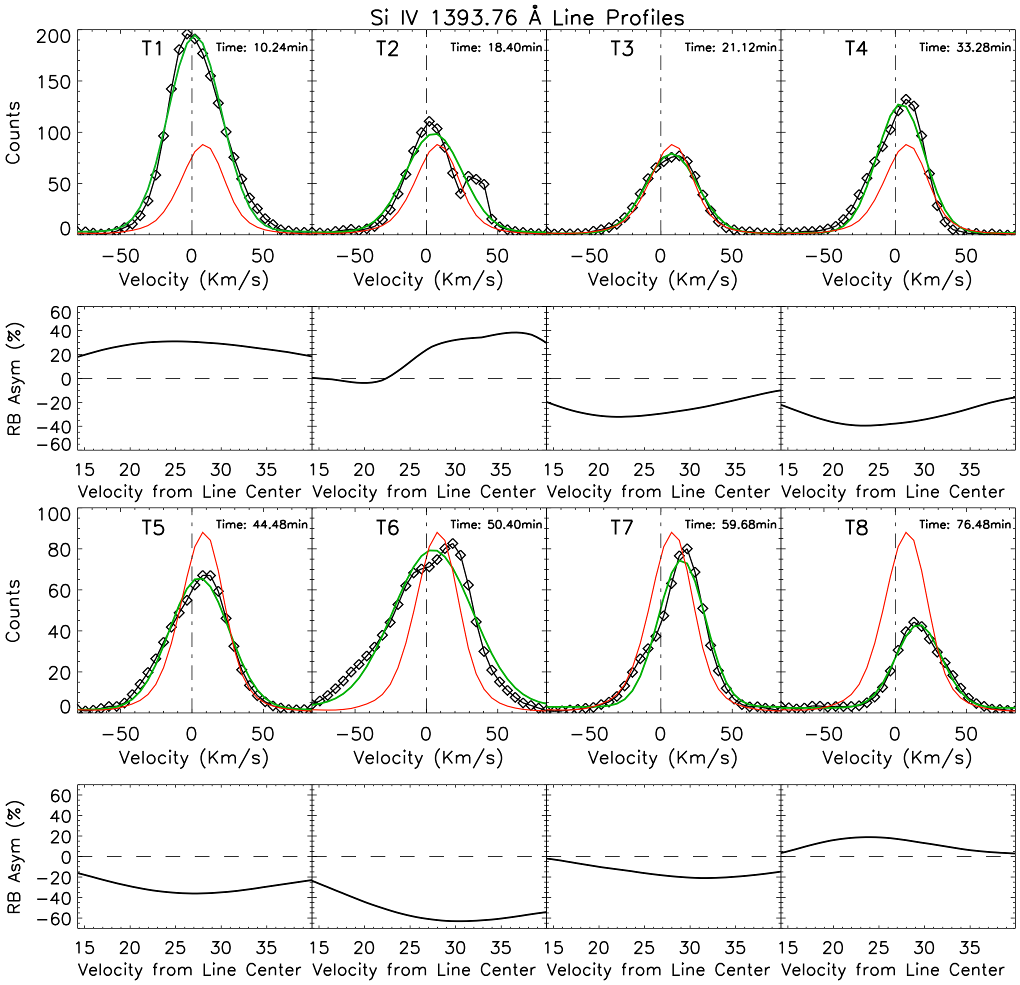

FIGURE 4.5: Line profiles of the Si IV 1393.76 Å line at various instances as labeled along with their corresponding RB asymmetry profile (from 15 to 40 Km $s^{-1}$) in the bottom. Red lines represent average line profiles over time. Green lines are the Gaussian fits. A movie (Movie 2) of the line profiles is available online.

taking the average over 15 - 40 km $s^{-1}$ velocity range for each profile. Positive and negative values represent enhancements in the red and blue wings, respectively.

Now, the variation of all the line parameters with time, along with HMI positive flux and AIA 335 Å intensity, is shown in Figure 4.4. Different rows (from top to bottom) correspond to HMI positive flux, intensity, deviation from average Doppler shift ($|V - V_{avg}|$), FWHM, absolute RB asymmetry ($|RB|$) of the Si IV 1393.76 Å line and AIA 335 Å intensity, respectively. Now for the correlation studies between different parameters and to find out the periodic nature, we have selected a time interval of 16 - 80 minutes. The initial rapid change in flux affects the power analysis, so we have omitted the first 16 minutes for this analysis. We use trend-subtracted smoothed LCs, as represented by red lines in Figure 4.4, for easier comparison. The wavelet analysis was applied over the smoothed curve to investigate the oscillation properties. Global wavelet power spectra, along with 99% confidence level, are shown in the middle panels. Observed periodicities are then printed on the right side. The power analysis on the line parameters shows the omnipresence of a strong periodicity around 8 and 13 minutes. CCs of all the line parameters with the absolute RB asymmetry are printed in each panel. We correlate different LCs with the RB asymmetry LC as the RB asymmetry provides a good measurement of the distortion in line profile from Gaussian. To investigate it further, we will focus on specific instances and will have a closer look at the variation of line profiles. We notice sudden changes in the line parameters at certain times. In Figure 4.4, horizontal grids represent the particular instances where certain changes occur. The line profiles at T1, T2, T3, T4, T5, T6, T7, and T8 time instances are shown in Figure 4.5 along with averaged (in red) and Gaussian fit (in green) profiles. The RB asymmetry profiles are shown in the lower panel. It clearly shows strong asymmetry in the profiles at those particular instances due to the existence of some secondary emission component. Movie 2 (available online) shows the evolution of the line profiles.

The correlation between intensity, FWHM, $|V - V_{avg}|$, and $|RB|$ can be easily explained in terms of sudden flows along the line of sight. In active region boundaries, all the line parameters coherently change due to quasi-periodic upflows in the medium (De Pontieu and McIntosh 2010; Tian *et al.* 2011a, 2012). In our study, we observed both red- and blueward asymmetries from time to time (see Figure 4.5) which is different from active region boundary studies, where predominantly blueward asymmetry is reported. Our observations can be explained in terms of both high-speed upflows and downflows. Transition region explosive events (EEs) could be a possible explanation (Brueckner and Bartoe 1983; Dere *et al.* 1989; Innes *et al.* 1997; Chae *et al.* 1998; Teriaca *et al.* 2004; Huang *et al.* 2014). EEs are believed to result from reconnection, which will affect the line profiles. Reconnection jets (regardless of the direction) usually lead to enhancements at the line wing (or wings), which would lead to large RB values, larger line width, and larger intensity. The presence of these additional flow components usually also leads to large perturbation of the Doppler shift. This sudden change in the line parameters is consistent with the behavior of bursty EEs. We find the periodic occurrence of EEs at one footpoint of a coronal BP. The observed periodicities at one footpoint of the BP at the different temperature channels are similar to the observed periodic changes in different line parameters, which may indicate that recurring EEs are likely producing the oscillatory signal seen in the BP.

Chae *et al.* (1998) reported that EEs happen preferentially in regions with weak and mixed-polarity magnetic fluxes. They also noticed that the majority of EEs occur during the cancellation of photospheric magnetic field. In our study, we find a correlation between RB asymmetry and underlying positive flux. We use a cross-correlation technique to find out whether the two LCs are showing a similar variation with some time delay (similar to Tian *et al.* (2012)). It shows that the $|RB|$ LC has a time delay (TD) of 1.12 minutes from the magnetic flux LC. Hence, It can be conjectured that the line profiles are strongly affected during the magnetic flux cancellation phase. It could be that the new emerging flux reconnects with the preexisting field, which cancels the local flux and creates EEs. The periodic behavior might be explained by repeated reconnection. One can also notice, while carefully looking at the variations, that the RB asymmetry do not change randomly; it changes slowly with a sharp increase around specific instances and then slowly decreases. This matches well with a slow reconnection scenario (Wang and Shi 1993). Slow magnetic reconnections occurring in the lower atmosphere could initiate fast reconnection in the TR and then decrease slowly. After some relaxation time, it repeats.

We also searched for the signature of heating due to reconnections. The AIA 335Å channel corresponds to an ionization temperature of about $2.5\times10^6$ K, with a wide temperature response. In Figure 4.4, the 335 Å LC shows an increase of intensity during the time when the line profiles show sudden changes. Due to reconnection, magnetic energy releases and heats the medium locally at the TR. This localized heating close to the reconnection point may increase the temperature at certain pockets in the TR, and AIA may see some of these emissions. Hence, depending on the heating, higher-temperature emission can enhance during the reconnection time. The AIA 335 Å LCs show similar properties. We wish to address this conjecture in our future work while looking at coronal spectral lines.

## 4.3 Conclusion

We study the dynamics of a BP within a CH using combined imaging, spectroscopic, and magnetic measurements. We focused our analysis on one footpoint of a bipolar loop structure. Throughout our observation, both positive and negative magnetic flux shows correlated variations. This may suggest that emerging flux interacts with the preexisting overlying fields, which results in reconnection and cancellation of the flux at the site of the BP. We conjecture that the periodic behavior of the positive flux may correspond to repeated reconnections which leads to a series of continuous periodic brightenings as seen in different EUV and far-UV lines. We propose that EEs are created due to X-point magnetic reconnection and resultant outflows generally affect the line profiles. The presence of the secondary component emission in the line profiles confirms that. Furthermore, we observed enhanced line profile asymmetry, enhanced line width, and a large deviation from the average Doppler shift at specific instances. The correlation between all these parameters is consistent with the scenario of repetitive alteration of the line profile by bursty reconnection outflows. We observe similar periodicities not only at different line parameters of the Si IV line but also with AIA channels, and they are concurrent in time and space and hence seem to be related. During EEs (see Fig. 4.4), we see a corresponding change in the magnetic field - this is a one-to-one correspondence and certainly indicates the close relationship between the two.

# Chapter 5

# Propagating disturbances in the solar corona and spicular connection[†]

## 5.1 Introduction

White-light and EUV emission from the polar region of the solar corona shows distinct, bright, ray-like structures known as polar plumes (van de Hulst 1950; Saito 1958, 1965; Deforest *et al.* 1997; Deforest and Gurman 1998). Quasi-periodic propagating intensity perturbations are frequently observed in the polar plumes and inter-plume regions with periods ranging from 5 to 30 minutes. The measured speed of these propagating disturbances (PDs) is around 150 km s$^{-1}$. These outward PDs are generally interpreted as slow magnetoacoustic waves propagating through the plumes and inter-plumes region because their speeds are similar to

---

[†] Results of this work are published in Samanta *et al.* (2015b).

All the animations that are referred to in this chapter are available at `http://dx.doi.org/10.1088/2041-8205/815/1/L16` the sound speed (Deforest and Gurman 1998; Ofman *et al.* 1999, 2000; Banerjee *et al.* 2000; O'Shea *et al.* 2007; Banerjee *et al.* 2009, 2011; Krishna Prasad *et al.* 2011; Gupta *et al.* 2012; Gupta 2014; Su 2014; Banerjee and Krishna Prasad 2015).

EUV observations from Solar TErrestrial RElations Observatory (STEREO), McIntosh *et al.* (2010) studied high-speed jets of plasma traveling along the plume structures with a mean velocity around 135 km $s^{-1}$. Those jets were quasi-periodic with the periodicities of 5 - 25 minutes. Tian *et al.* (2011c) also showed that high-speed repetitive outflows, which originate near magnetic network elements both in the quiet-Sun and coronal holes (CHs), propagate along plume structures with an average speed of $\sim$ 120 km $s^{-1}$. McIntosh *et al.* (2010) suggested that the PDs are nothing but these jets originating from the upper chromosphere, which propagate to higher corona and contribute to the solar wind. They further conjectured that these jets will supply adequate energy to the fast solar wind. Pucci *et al.* (2014) found radially moving radiance variations both in the plume and inter-plume regions. Comparing the apparent outflow speeds at different temperature passbands they concluded that the observed radiance variations represent the material outflows.

The quasi-periodic intensity enhancement, the Doppler shift, and the line width enhancements in coronal structures have also recently been interpreted as due to high-speed upflows from spectroscopic observations in magnetic regions of the solar atmosphere (De Pontieu *et al.* 2009; De Pontieu and McIntosh 2010; De Pontieu *et al.* 2011; Tian *et al.* 2011a,b; Martínez-Sykora *et al.* 2011; Tian *et al.* 2012; Mandal *et al.* 2015). Pant *et al.* (2015) have studied an on-disk plume as seen in by the Atmospheric Imaging Assembly (AIA) and their connection to transition region jets seen in the Interface Region Imaging Spectrograph (IRIS). They found that small-scale chromospheric jet-like features are linked with the generation of PDs within the plume. De Pontieu *et al.* (2011) found that spicules seen in AIA 304 Å channels propagate upward and fall back following parabolic paths, whereas, at the same time, they also found that enhanced emissions seen in 171 Å propagate upward into the corona with speeds of $\sim$ 100 km s$^{-1}$. It has yet to be explored whether similar behavior can been seen in the off-limb corona and thus this is the subject of the present analysis.

Recently, Jiao *et al.* (2015) claimed that the spicular activities in the solar transition region, as seen in the AIA 304 Å passband, are responsible for the generation of the PDs in the polar regions of the corona as observed in the AIA 171 Å images. However, the exact connection between spicule and PDs, as well as the nature of the PDs, still remains a mystery. Furthermore, for the solar wind studies, it is important to have a better understanding of the nature of these PDs and their origin. To find out the spicular connection to the coronal PDs, we use simultaneous IRIS data along with coronal data from AIA.

## 5.2 Data analysis and Results

### 5.2.1 Observation and Data Reduction

The data was obtained from a coordinated observations using the IRIS and the AIA instruments. Observations were performed from 11:25 UT to 12:55 UT on 21 February 2014. Slit-jaw images (SJIs) from IRIS filtergrams centered at 2796 Å and 1400 Å, dominated by Mg II k and Si IV emission lines, respectively, were analyzed. AIA filtergram images centered at 304 Å, 171 Å, and 193 Å, dominated by He II, Fe IX and Fe XII emission, respectively, were also selected for the analysis. The IRIS 2796 Å passband is sensitive to emission from plasma at temperatures of $\sim$10,000 to 15,000 K and IRIS 1400 Å is sensitive to temperatures $\sim$ 60,000 to 80,000 K. The AIA 304 Å, AIA 171 Å, and AIA 193 Å filter's response functions peak at 0.05, 0.8 and 1.25 MK respectively.

IRIS observed the south pole of the Sun in sit-and-stare mode. We used IRIS Level 2 processed data, which is corrected for dark-current, flat-field, and geometrical corrections etc. All of the IRIS SJIs were taken with an 8 s exposure time and a cadence of 19 s. The pixel size of SJIs and AIA are $0.166''$ and $0.6''$ respectively. The AIA images were taken with a 12 s cadence. The pixel size of AIA is interpolated to the match with IRIS for easier comparison. All of the AIA channels were coaligned and derotated to compensate for solar rotation. The IRIS SJIs and AIA images were coaligned using IRIS 1400 Å and AIA 1600 Å images (as described in Skogsrud *et al.* (2015)).

Figures 5.1 (a)-(e) show the south polar region of the Sun as seen from IRIS and AIA channels. We should point out here that CH was not seen clearly on the south pole during the observation, hence the the region can be characterized as a quiet-Sun. Furthermore, distinct extended plume structures were not so clearly visible from the original images. Usually, when there is a underlying deep CH present, plume structures are clearly visible.

### 5.2.2 Power Maps

PDs in the corona often repeat with a timescale of 10 - 30 minutes. To find the global behavior of PDs, we constructed powermaps in the period band of 10 - 30 minutes. We performed a wavelet analysis in the time series at each pixel location to estimate the distribution of power. A background trend is removed by subtracting a 30 minute running average of the original time series to remove periods longer than 30 minutes. Figure 5.1 (f)-(j) show the distribution of power (referred to as powermaps) within the 10 - 30 minute period band of IRIS 2796 Å, IRIS 1400 Å, AIA 304 Å, AIA 171 Å and AIA 193 Å channels. The powermaps of IRIS 2796 Å, IRIS 1400 Å and AIA 304 Å show the power in this period band is limited to lower heights (within $\sim 20''$ from the solar limb). These channels

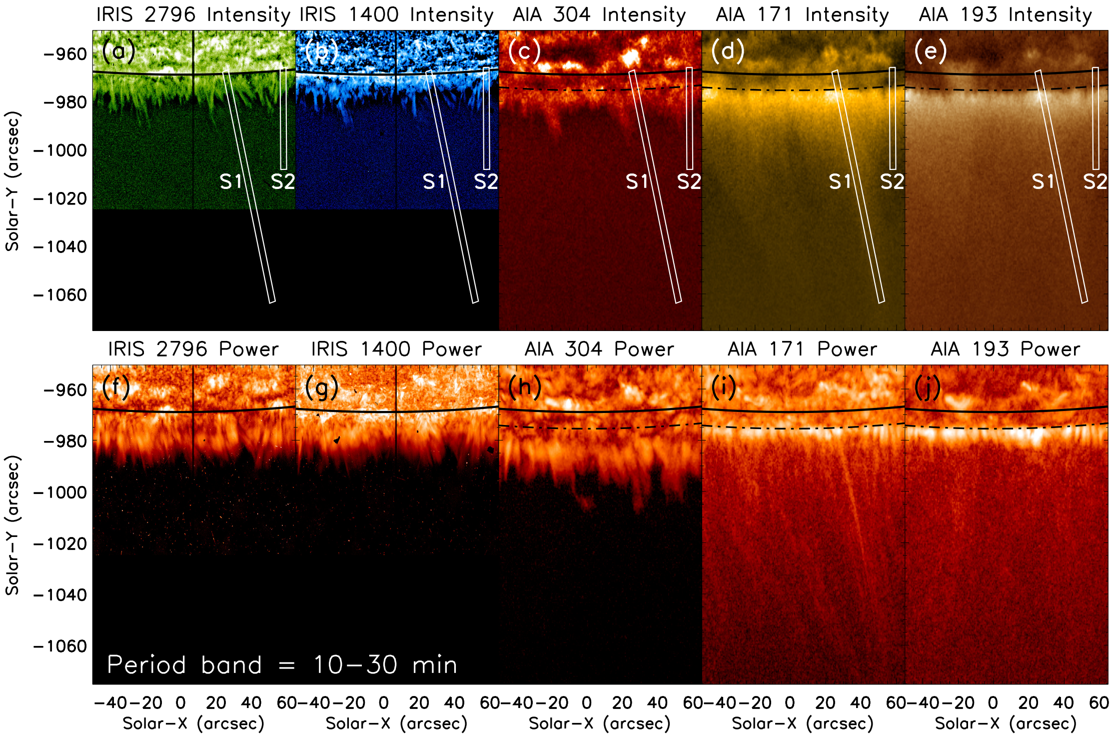

FIGURE 5.1: (a)-(e) Display a portion of the south polar region of the Sun as seen in different filtergram images taken from IRIS and SDO/AIA instruments on 21 February 2014 as marked (an animation is available online: movie1). The vertical black line on each IRIS SJIs represents the position of the IRIS slit. The solid black curve line on each image shows the location of the solar limb. The dotted-dashed black line on each AIA image displays the location of the solar limb as identified from the AIA 171 Å image. The field of view (FOV) of IRIS is smaller than the selected window of AIA images, which makes it appear dark in SJIs where IRIS FOV does not overlap with AIA. Two boxes (S1 and S2) show the location of the selected slits used to construct the space-time (XT) plot (see Figure 5.2 and 5.3). (f)-(j) Show the distribution of power (powermaps) of corresponding top panel channels. The powermaps are constructed by taking the average power of the 10 - 30 minutes period band.

are sensitive to the chromospheric and transition region temperature, which is dominated by spicular activity and the power is probably limited to lower heights due to this. At some locations, we note that the strong power is seen up to higher heights. In AIA 171 Å and AIA 193 Å powermaps, we observed two kinds of features, one reaching to larger distances (see the location of S1 slit) and the other which has comparatively higher power, but is confined to shorter distances (see the location of S2 slit). In the next subsection, we will study in detail the behavior of PDs in these regions (within S1 and S2).

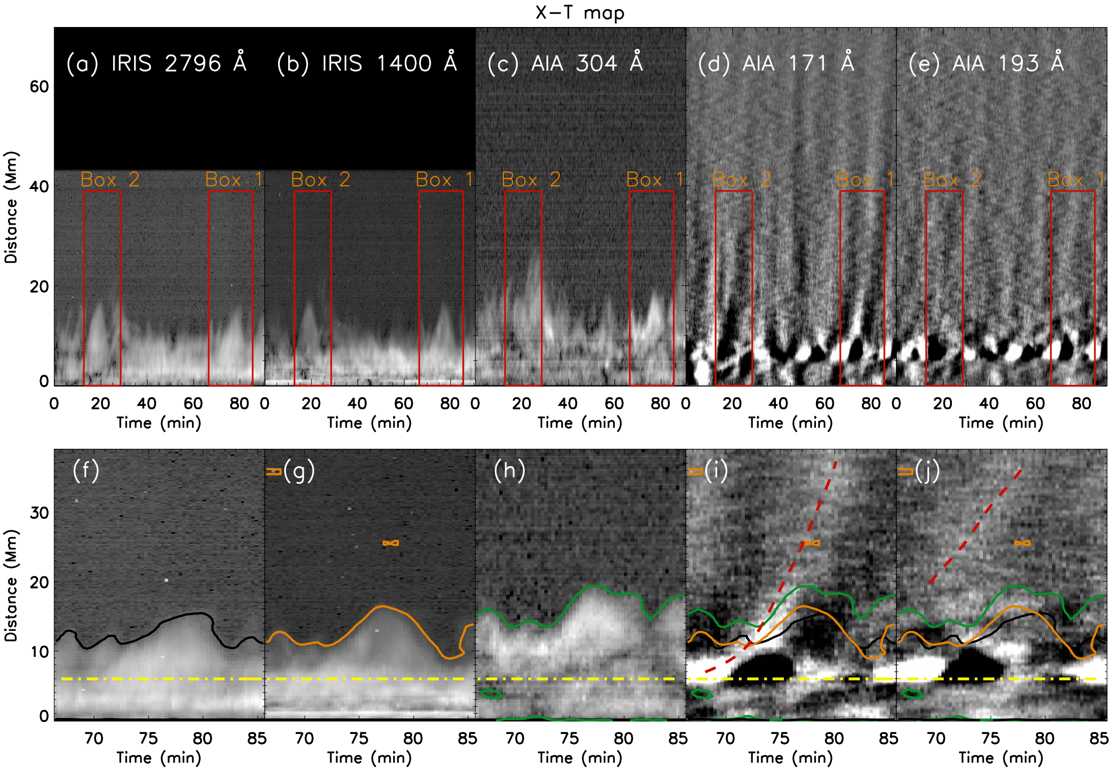

Figure 5.2: XT plots corresponding to the S1 slit and different passbands as marked. A zoomed view of the region inside the red rectangular Box 1 (marked in the upper panels) is shown in (f)-(j). Animations corresponding to Box 1 (movie2_box1) & 2 (movie3_box2) is available online. Black, orange, and green contours show the envelopes of the spicular temporal evolution as seen in the IRIS 2796 Å SJI, IRIS 1400 Å SJI and AIA 304 Å channels. These contours are overplotted in the AIA 171 Å and AIA 193 Å XT map for comparison. The dotted-dashed horizontal line in yellow represents the limb of the Sun as seen in AIA 171 and 193 Å. Dashed red curves track the PDs observed in AIA 171 and 193 Å.

### 5.2.3 Space-Time Plot

In this subsection, we focus on the plume-like structure marked by the S1 slit in Figure 5.1 for a detailed time evolution of PDs. We constructed the XT map to study the temporal evolution of the region inside the S1 slit. The signal in the AIA channels is low for off-disk features, hence, to improve the signal to noise, we have used a thick slit with a width of $3.32''$. The average intensity along the width of the slit was used to construct the XT maps of different channels. The XT map of AIA 171 and 193 Å were processed by removing a smoothed background trend

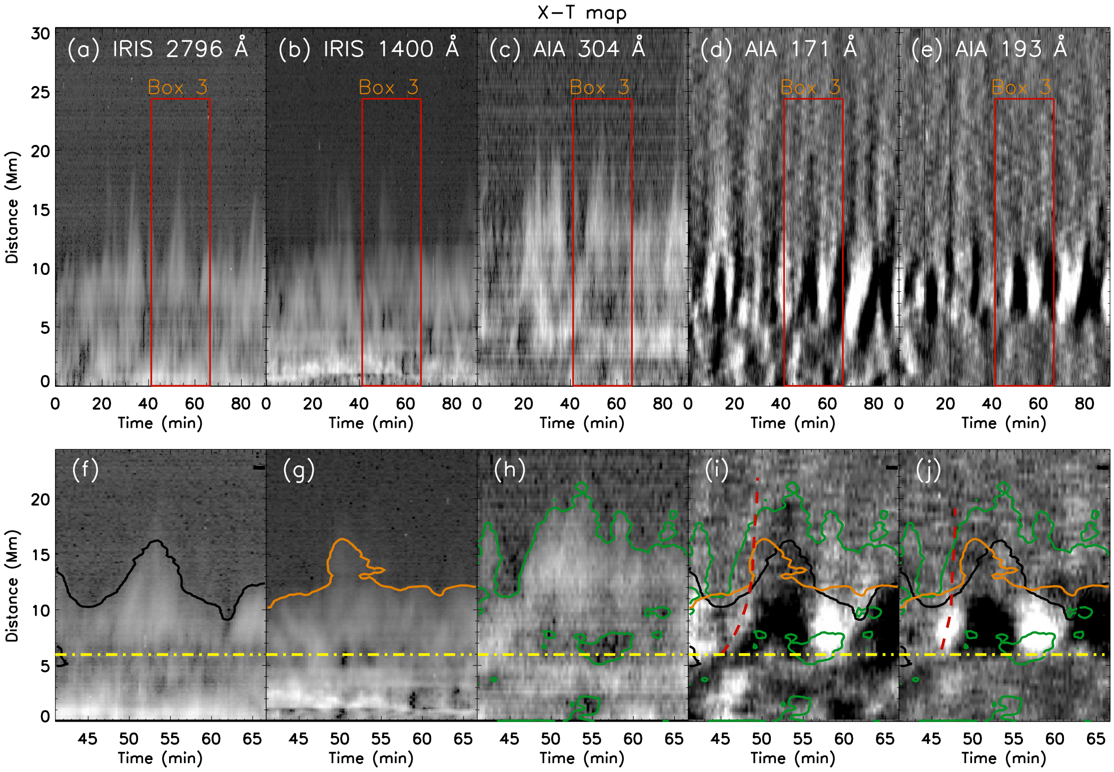

FIGURE 5.3: XT plots corresponding to the S2 slit and different passbands as marked. All panels are similar to those in Figure 5.2. Animation corresponding to Box 3 (movie4_box3) is available online.

along the time axis to enhance the visibility of the alternating ridges. The results are shown in Figure 5.2. The XT maps of the IRIS 2796 Å, IRIS 1400 Å and AIA 304 Å which are sensitive to chromospheric and transition region temperatures, show the evolution of several spicules. On the other hand, the dark and bright ridges extended over longer distances are seen in the AIA 171 and 193 Å channels. The zoomed view of a portion of the XT map is shown in the bottom panels of the same figure. The temporal evolution of spicules are seen in IRIS 2796 Å, IRIS 1400 Å and AIA 304 Å appears to have sub-structures rising and falling in all passbands. It appears that they roughly follow the parabolic path as seen in many spicules. Contours are over-plotted by choosing some intensity threshold on the IRIS 2796 Å, IRIS 1400 Å and AIA 304 Å channels, which are shown by black, orange, and green contours respectively. It covers the envelope of the spicular temporal evolution. These three contours are also overplotted in the AIA 171 and 193 Å XT maps. The trajectories of the PDs are marked by red dashed curves, as shown in the zoomed AIA 171 and 193 Å panels of Figures 5.2 and 5.3.

A similar procedure was adopted for the slit S2 analysis. The slit width of the slit S2 is the same as S1. The XT maps for different channels are shown in Figure 5.3. In the lower panels of Figures 5.2 and 5.3, we note that the start of the trajectory of PDs is almost cotemporal with the time of the rise of the spicular envelope. We also note that the falling of the spicular envelope is followed by brightenings and the generation of another PD in AIA 171 and 193 Å.

It is worth noting that PDs in Figure 5.2 (following a plume-like structure) are propagating to higher heights (65 Mm), as compared to PDs in Figure 5.3, which seem to propagate roughly about 30 Mm. Thus, power was confined to lower heights at the slit S2 location.

### 5.2.4 Measurements of the propagating speed of the PDs

To follow the PDs and its connection with rapidly evolving spicular activities, we produce a composite XT plot (Figure 5.4). The IRIS channels corresponding to the bottom part of the maps (as marked) allow us to identify the spicules and their temporal evolution whereas the AIA channels corresponding to the upper part of the maps allow us to identify the PDs quite clearly. In order to see the alternating ridges clearly, we enhance the contrast by subtracting the smooth background in XT maps. This procedure is followed for AIA channels (i.e, the upper part of the maps in Figure 5.4). For the IRIS channel (the lower part of the maps), no background subtraction is performed because no enhancement in the lower part of XT maps is needed. This further demonstrates that when a spicule is observed by the chromospheric channel of IRIS, a PD seems to be generated and/or amplified in the AIA coronal channels. This also confirms that the PDs seem to be quasi-periodic with a periodicity that is governed by the repetition time scale of

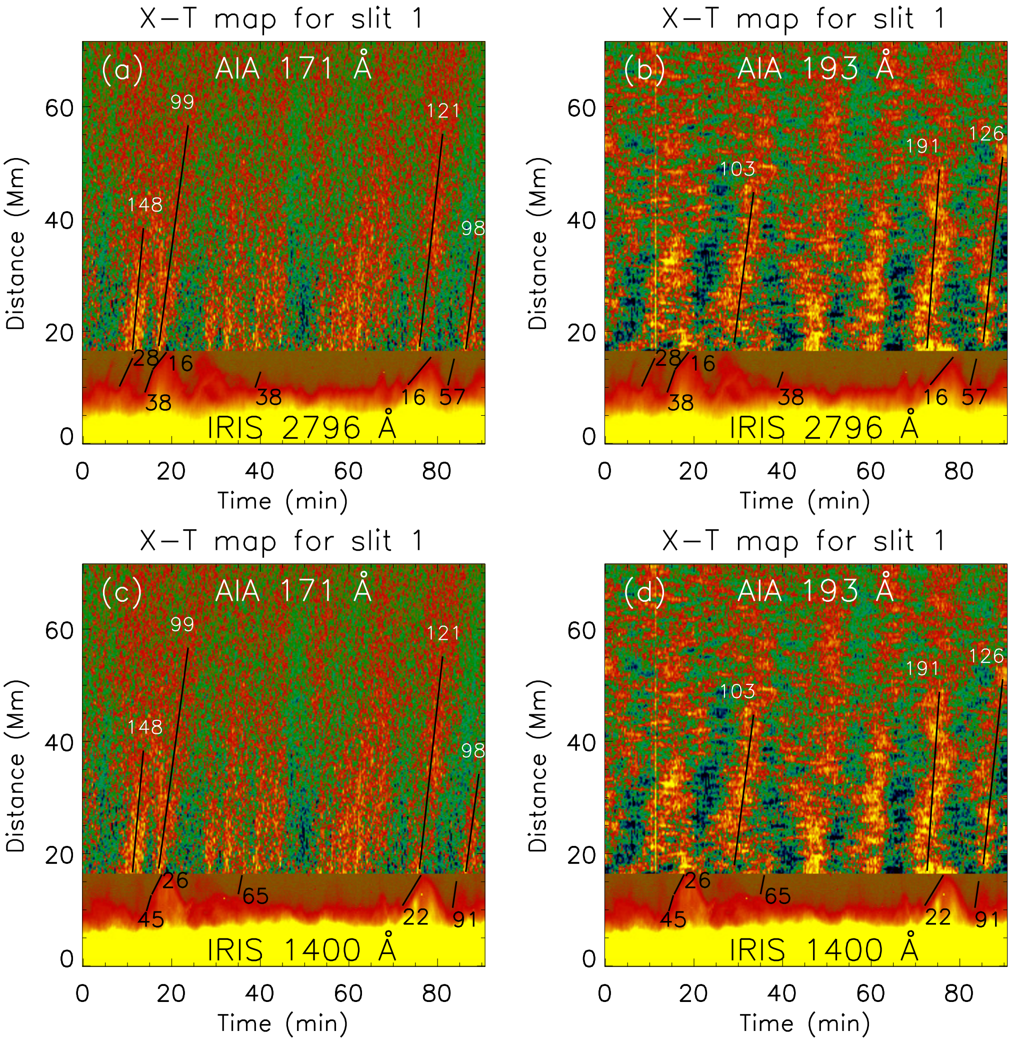

FIGURE 5.4: XT plots corresponding to slit location S1 (along a plume-like structure) showing connection between spicular activities as seen by IRIS channels (bottom) and PDs as seen by coronal AIA channels (top). The slanted black lines are used to measure the speeds. Measured speeds in km $s^{-1}$ are printed.

occurrence of the spicules. From this figure, we also fit the ridges manually using eye estimation and found the range of velocities from 98 - 148 km $s^{-1}$ in AIA 171 Å and 103 - 191 km $s^{-1}$ in AIA 193 Å. There is a large uncertainty in the measured speed, thus we cannot confirm if we observe different speeds in the two different channels. We find the speeds of spicules from 22 - 91 km $s^{-1}$ corresponding to IRIS 1400 Å images and 16 - 57 km $s^{-1}$ for IRIS 2796 Å images. Since the speeds are higher than sound speed at chromospheric levels, these spicules could be generated by reconnection at lower heights.

## 5.3 Conclusion

PDs are ubiquitous in the solar atmosphere and it has recently been suggested by Jiao *et al.* (2015) that spicules can trigger coronal PDs. From their study, using the AIA data alone, they provided a possible link between spicular activities and the generation of PDs. They used the AIA 304 Å channel to identify the spicules. Though, they did not comment on the nature of the PDs. We extended that work using the higher cadence and higher resolution IRIS spectral images to study the dynamical behavior of the spicular activity and, while combining AIA channels, we are able to confirm the link with a better confidence. We believe that a combination of chromospheric and transition region channels of IRIS and transition region and coronal channels of AIA is better suited for this kind of study. We also point out a possible connection between the small-scale, short-lived, cool spicular structures with the very-large-scale, long-lived, hot plume structures. We find that the start of trajectory of PDs is almost cotemporal with the time of the rise of the spicular envelope and the spicular material fall is cotemporal with brightenings followed by the generation of another PD in AIA 171 Å and 193 Å. The cotemporal generation of spicules and PDs suggests that they might have a common origin. We should point out here that there could be a projection effect and that we cannot rule out the possibility that the spicules and PDs may not be in the same position; however, statistically, we find cotemporal and cospatial matches in most of the cases studied. Figure 5.4 illustrates the quasi-periodic nature of the spicular activity as revealed by the IRIS spectral image sequences and its relation to coronal PDs as recorded by the coronal AIA channels. We propose that reconnection-like processes generate the spicules and waves simultaneously. The waves escape while the cool spicular material falls back. The PDs as seen have a mixed signature of waves and flows at lower heights while at the extended coronal heights the wave signature is dominant. There is also a signature of acceleration of these PDs as represented by the curved, red, dashed lines in the lower panels of Figures 5.2 and 5.3. The nature of PDs in our case is not always confirmatory, but the presence of alternating bright and dark ridges and reaching of accelerating PDs to higher heights in slit position S1 (see Figures 5.2 and 5.4) suggest a more wave-like nature while manual fitting of PDs to derive speeds is not accurate enough to confirm wave-like behavior. We should also point out that we did not have any CHs in the polar regions and thus the presence of plume-like structures were also not very clear at all locations. At slit position S2, we find that PDs are not going to higher heights. Thus, power is confined to lower heights close to the limb. The enhancement in power is due to repeated generation of cool spicular material seen as dark features in hot AIA channels. Due to almost straight ridges, poor signal to noise, we could not measure the speeds of these PDs convincingly and thus cannot comment on their nature. It is also possible that at the time of the generation of spicules (due to heating together with reconnection and/or driven by $p$-modes) the hot material can escape following the open magnetic field lines and thus cause intensity enhancements in the AIA 171 and 193 Å channels while spicular material falls back because it is denser and cooler than escaping hot material. With the existing spectral imaging data, the connection of spicules and PDs are subject to line-of-sight uncertainties. For further confirmation and a better understanding of the nature of the PDs, we need simultaneous chromospheric and coronal long spectral time sequences.

# Chapter 6

# Dynamics of subarcsecond bright dots in the transition region above sunspot and their relation to penumbral micro-jets[†]

## 6.1 Introduction

Sunspots are regions of concentrated strong magnetic fields comprising a dark central region of umbra surrounded by a less dark region called the penumbra. Penumbral micro-jets (PMJs) are one of the prominent fine-structure dynamical features observed in the sunspot at the chromospheric heights. Using the Solar Optical Telescope (SOT) Ca II H filter images, Katsukawa *et al.* (2007) first reported that these micro-jets occur ubiquitously above penumbra. They have lengths of 1

---

[†] Results of this work are published in Samanta *et al.* (2017).

All the animations that are referred to in this chapter are available at `https://doi.org/10.3847/2041-8213/835/2/L19`

- 4 Mm and lifetimes of up to a minute. They generally move very fast and have apparent speeds over 100 km $s^{-1}$. The magnetic field in the penumbral region consists of a combination of spines (more vertical fields) and interspines (more horizontal fields) (Lites *et al.* 1993; Bellot Rubio *et al.* 2004; Scharmer *et al.* 2011; Scharmer and Henriques 2012; Henriques and Kiselman 2013; Tiwari *et al.* 2013, 2015). Katsukawa *et al.* (2007) found that PMJs generally originate near the bright structures in between two dark penumbral filaments and propagate upward along the direction of the spine field. This, they proposed that PMJs could originate as a result of magnetic reconnection between the spine and interspine magnetic field.

Using the Interface Region Imaging Spectrograph (IRIS) observations, Tian *et al.* (2014b) found the presence of subarcsecond bright dots (BDs) above sunspot penumbra in the transition region (TR). They appear ubiquitously and most have a lifetime of less than a few minutes. They sometimes appear slightly elongated along the penumbral filaments and also move along the filaments with speeds of 10 - 40 km $s^{-1}$. They proposed that some of them could be due to impulsive reconnection in the TR and chromosphere at footpoints of coronal magnetic loops and others are probably due to falling plasma. It is still unclear how BDs are formed and if they show any signatures in the lower and upper atmosphere.

Vissers *et al.* (2015) studied the multi-wavelength signatures of PMJs and found that PMJs show a spatial offset from the chromosphere to the TR in the direction of the PMJ. Hence, they proposed that PMJs may progressively heat up to TR temperatures. Tiwari *et al.* (2016) could not find noticeable signature of normal PMJs in any Atmospheric Imaging Assembly (AIA) passbands, although a few strong and large PMJs show BD/BD-like signatures in the 1600 Å and High-resolution Coronal imager (Hi-C) 193 Å images. Alpert *et al.* (2016) found that BDs observed in Hi-C are slower on average, dimmer, larger in size, and longer-lived than IRIS penumbral BDs. They also found that most of the BDs observed in Hi-C 193 Å may correspond to TR. Deng *et al.* (2016) found that the locations of most of the penumbral BDs show downflow. Their statistical analysis shows that BDs do not have a consistent brightening response in the chromosphere. Following Tian *et al.* (2014b), they also suggested that TR penumbral BDs are a manifestation of falling plasma from coronal heights along more vertical and dense magnetic loops or small-scale impulsive magnetic reconnection at TR or higher heights. Kleint *et al.* (2014) and Chitta *et al.* (2016) observed heating events that are associated with the strong downflows in the TR and proposed a similar scenario. Bai *et al.* (2016) have studied small transient brightening events in the penumbra and found that they show redshifts in the Si IV 1402.77 Å line, an inward motion toward the umbra in IRIS 1400 Å images, and has a multi-thermal component. They proposed the triggering mechanism as magnetic reconnection at low coronal heights. A component of the plasma from the reconnection site may move downward and reach the TR, which is confirmed by the observed redshifts in the Si IV 1402.77 Å line and the inward motions as seen in the IRIS 1400 Å images. Finally, it reaches the chromosphere and appears as ribbon-like brightening.

In this work, while combining multi-wavelength observations covering the chromosphere and the TR/corona we try to find the source of the BDs and their relation to PMJs.

## 6.2 Data analysis and Results

### 6.2.1 Observation and Data Reduction

We use the data obtained from a coordinated observation taken on 19 March 2014, using the HINODE/SOT (HOP-250), IRIS (IRIS-3840007453), and the AIA. The coordinated observation between all the instruments was performed from 08:51 UT to 09:46 UT. We selected a FOV of 37″x50″ centered at 200″ and 317″. The FOV

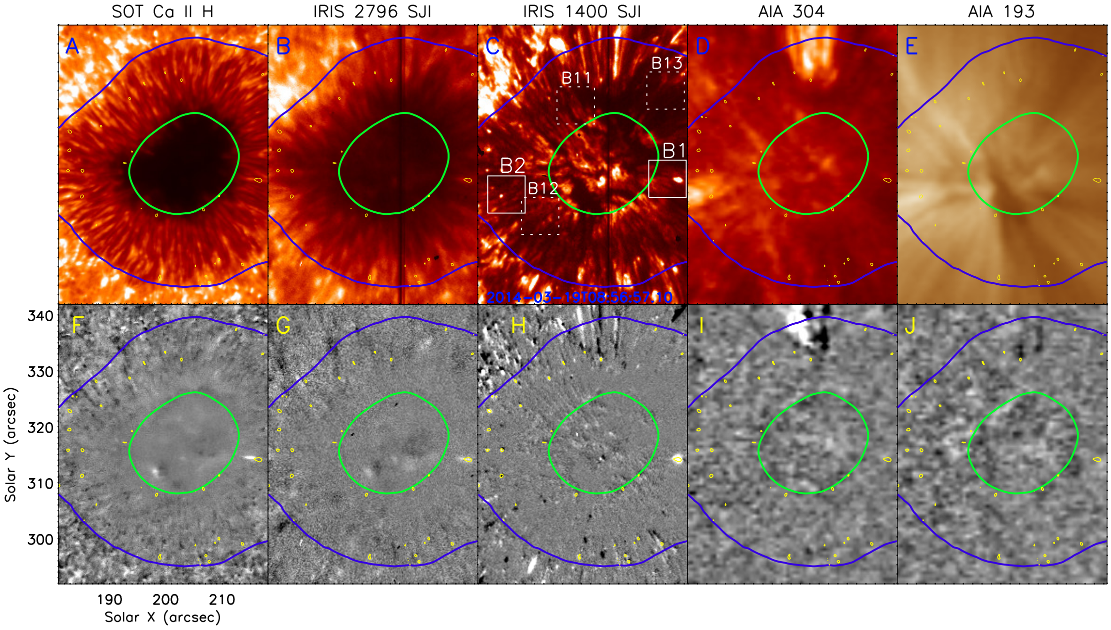

FIGURE 6.1: A-E: image of a sunspot as seen by the SOT, IRIS, and AIA around 08:57 UT on 19 March 2014. F-J: running difference images. The green and blue contours, derived from a time-averaged smoothed SOT image, represent the umbra and penumbra of the sunspot, respectively. The yellow contours mark the locations of bright dots (BDs). The evolutions of the BDs inside the boxes B1 and B2 (as marked in the 1400 Å) are shown in the Figure 6.2 (animated figures corresponding to B1, B2, and B11-B13 are available online.) An animation of this full figure is also available.

is limited due to the SOT observations. IRIS Slit-jaw images (SJIs) centered at 2796 Å and 1400 Å are dominated by the Mg II k and Si IV emission lines, respectively. The SOT filter is dominated by the Ca II H line, which forms at the lower chromosphere where the temperature is below $10^4$ K. The IRIS 2796 Å images are dominated by the emission from a plasma at temperatures of ∼10,000-15,000 K and represent the middle chromosphere. The IRIS 1400 Å passband is sensitive to TR ∼60,000-80,000 K. AIA filtergram images centered at 304 Å (sensitive to ∼0.05 MK) and 193 Å (∼1.25 MK) are dominated by He II and Fe XII emission lines, respectively. SOT Ca II H data was taken with 0.3 s exposure and 1.58 s cadence. IRIS SJIs were obtained with 4 s exposure and a cadence of 10.5 s. AIA 304 Å and 193 Å observations were taken with 2 s exposure and 12 s cadence. AIA data were then co-aligned and de-rotated to the start time (08:51 UT) of observation to compensate for the solar rotation. The pixel sizes of SOT, SJIs and AIA are $0.109''$, $0.166''$ and $0.6''$, respectively. We have interpolated SOT and AIA data in space and time to match the IRIS SJI cadence (10.50 s) and spatial resolution ($0.33''$ ). The IRIS SJIs and SOT images were co-aligned using IRIS 2796 Å and SOT Ca II H images. The time difference between the SOT and IRIS image is of the order of subseconds. After that IRIS and AIA were co-aligned using IRIS 1400 Å and AIA 1600 Å images (Samanta *et al.* 2015a).

Figure 6.1 shows the image of a sunspot, where the bottom rows (G-K) correspond to running difference images. The yellow contours show the location of BDs in the sunspot penumbra. These contours are obtained from the 1400 Å image after subtracting the same image with a 8×8 pixel smoothing. The evolution of two BDs inside the box B1 and B2 (as marked in 1400 Å) are shown in the Figure 6.2 (also in online movie). The BDs inside the box B1, including box B11, B12, and B13, are related to PMJs. The BD inside box B2 is not related to any visible dynamics in the SOT.

### 6.2.2 Temporal evolution of BDs and PMJs

Figure 6.2 depicts the temporal evolution of two BDs. (B1) shows the evolution of the BD inside the B1 box in the Figure 6.1. Panels A, C, and E show the evolution as seen in the IRIS 1400 Å, SOT Ca II H and IRIS 2796 Å images, whereas the B, D, and F correspond to running difference images. The clear presence of a BD is seen in the in the 1400 Å image. A jet-like feature is also seen in the Ca II H and 2796 Å images. Similarly, (B2) show the evolution of the B2 region as marked in the Figure 6.1. Here, we can clearly find the presence of a BD in the 1400 Å channel but no clear signature of intensity enhancement in the Ca II H . We have identified several BDs and performed a statistical analysis to compile the properties of these BDs and their signatures in the other channels. At first, we manually identify an isolated BD and look for the time frame where it shows maximum intensity

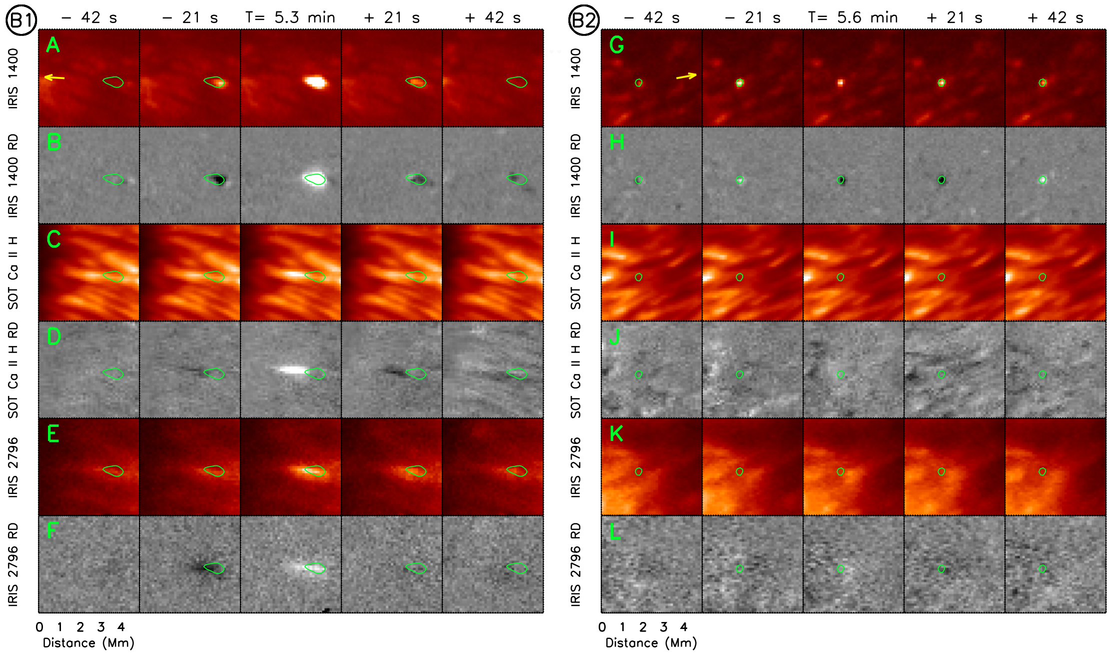

FIGURE 6.2: (B1) shows the temporal evolution of a BD and a PMJ inside the B1 region (as marked in the Figure 6.1) as seen in different filtergram images and their running difference images. The green contour is derived from the top middle panels to show the location of the BD. The yellow arrow indicates the direction of the sunspot center. Similarly, (B2) shows the temporal evolution of the B2 region (as marked in the Figure 6.1)

enhancement. We use that as our central frame and have created a video (see the Figure 6.2 animation, which covers a 5×5 Mm region for a duration of 210 s) to follow the BDs and their direction of propagation. The BDs often show apparent movements along the bright filamentary structures roughly in the radial direction of the sunspot.

To find the properties of the BDs, we follow a similar method as used by Tian *et al.* (2014b). Two examples of the analysis are shown in Figure 6.3 (B1) & (B2). We have studied 180 penumbral BDs and try to find if they have any signatures in the SOT Ca II H and IRIS 2796 Å channels. We use the central image to compute the intensity enhancement, length, and width of a BD, as shown in Figure 6.3 (B1). We plot the intensities along the green cut and red cut (panel A). The green cut is placed along the radial direction and the red cut is perpendicular to it. The intensity values are shown by red and green diamond symbols. A fitted Gaussian

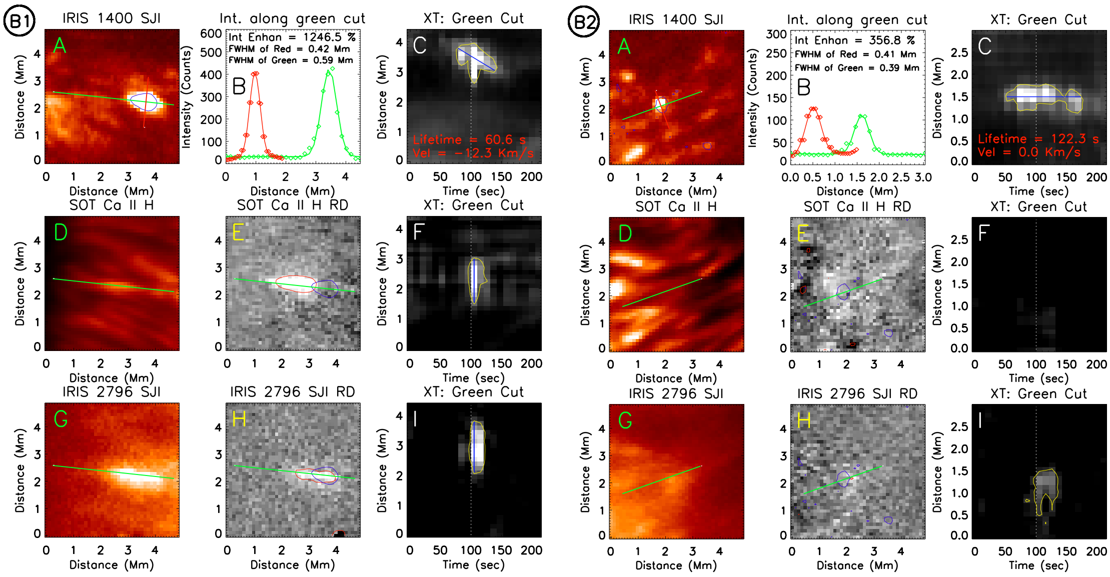

FIGURE 6.3: (B1) shows the procedure for determining the physical parameters of the BD and the PMJ inside the B1 region (as marked in the Figure 6.1). (A) shows the BD enclosed by the blue contour as seen in the 1400 Å. The green slit and red slit are placed along the radially outward direction and its perpendicular direction, respectively. (B) shows the intensity profile along the green and red slit with a diamond symbol. The solid line is a Gaussian fit to the profiles to determine the width and intensity enhancement of the BD. (C) shows the temporal evolution (XT plot) along the green cut. The yellow contour shows the region above $2\sigma$ intensity enhancement. The slop of the blue line is used to determine the plane of the sky velocity of the BD. (D) shows the Ca II H image. The green line is the slit to determine the XT plot. (E) shows the Ca II H image after subtracting the previous frame. The red contour shows the location of the PMJ. (F) shows the XT plot for the green cut of Ca II H images. (G) shows the 2796 Å image. (H)-(I) are similar to (E)-(F), respectively, but are for the 2796 Å channel. Similarly, (B2) shows for the BD inside B2 region (as marked in the Figure 6.1).

is also overplotted with the same color. The FWHM of the green profile provides an estimate of the length of the BD, whereas the red profile provides the width. The percentage of intensity enhancement is calculated from the peak intensity and the linear background of the fitted Gaussian. Of the two values, the lowest value (green and red) measures the intensity enhancement. We plot a space-time (XT) diagram (panel C) to study their temporal behavior and to measure their apparent speed. A $2\sigma$ intensity contour is drawn on the XT map. The inclined blue line is drawn inside the contour to measure the apparent velocity and lifetime of the BD. The starting time of the blue line is considered to be the initiation of the BD. The long intensity strip at the center of the XT map is due to high intensity enhancement at that particular time frame. We follow a similar method for the Ca II H and 2796 Å channels (D and G). The intensity enhancement in these channels is only a few percent and it is very difficult to find the location of the intensity enhancement. Thus, we use the running difference images to place our green and red cut (see E and H) on the original images.

The XT map is produced after removing a smoothed background from each image. An elongated bright structure is seen in the XT plot. These have been conventionally referred as penumbral micro-jets (PMJs) by Katsukawa *et al.* (2007). The lifetimes of these jets are very small. Most of them appear as sudden brightening in the XT plot and hence it is very difficult to determine their direction of propagation and the speed. In this work we do not focus on the speed of these jets. Using earlier conventions we have assumed that these brightenings are propagating outward from the sunspot, though it is not clearly established from our analysis that the bright structures are moving outward from the sunspot. We use a $2\sigma$ intensity contour to find the location and extent of the PMJ. The blue line is drawn along the direction of intensity enhancement. The starting time of the blue line is considered as the initiation and the length of the line is considered as the length of the PMJ. We can clearly see that the BD appears before the PMJ in this example.

Similarly, in Figure 6.3(B2), we study another BD. Following the same methodology we study the evolution of the BD. We could not find a clear signature of the BD in the Ca II H though a faint signature is seen in the 2796 Å channel. In the following subsection a statistical study is performed to find out if there are two types of BDs present in our data.

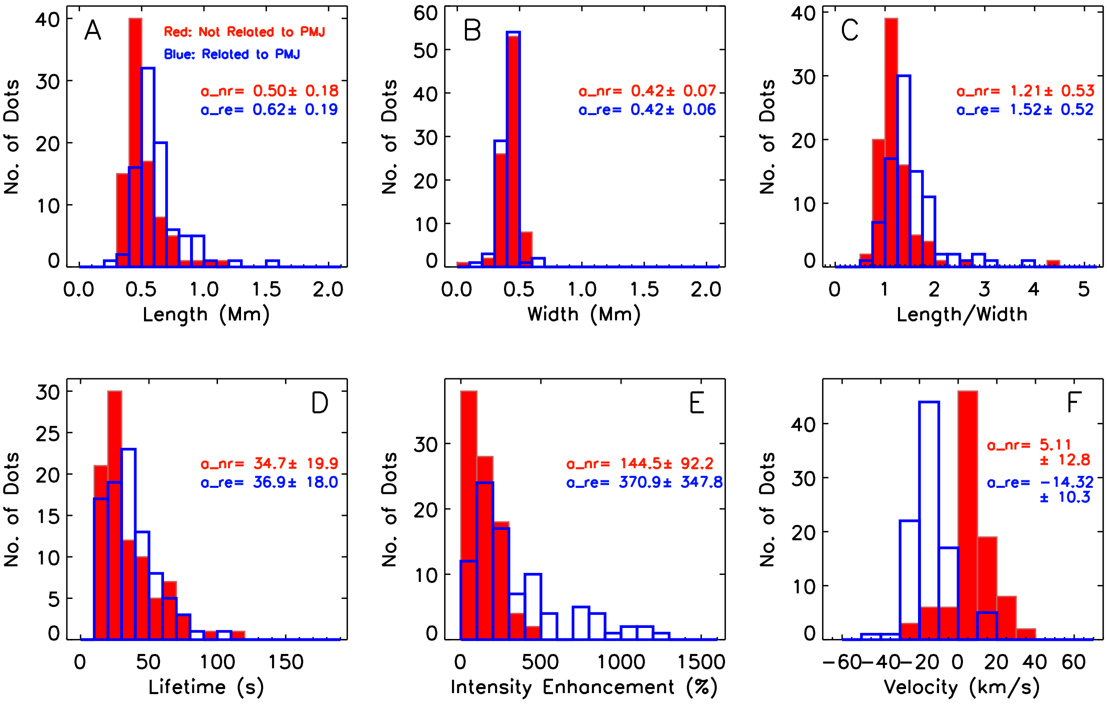

FIGURE 6.4: (A)-(F) show the distribution of different physical parameters of BDs. Red represents the BDs that do not have any connection to the PMJs, and blue represents those which are found on the top of the PMJs. (A) shows the of the length (FWHM of the intensity profiles along the green slit), (B) shows the width (FWHM of the intensity profiles along the red slit), (C) shows the ratio of length and width, (D) shows the lifetime, (E) shows the intensity enhancement, and (F) shows the plane of the sky speed of the BDs. The average value of each parameter and also its standard deviation are also provided (a_*nr* and *a_re*).

### 6.2.3 Statistical behavior of the BDs

We analyze the properties of many BDs and their signatures in the other channels. Out of 180 total events, 90 are identified as having a correlated signature in the Ca II H and 2796 Å channels, while the other 90 do not. We have separated these two classes so as to find out if they have any significant differences in their physical properties. Figure 6.4 (A)-(F) show the distributions of the observed parameters. The red color in the histograms represents the BDs that do not have a counterpart in the Ca II H images, whereas the blue represents the BDs that are related to the Ca II H PMJs. The mean value of each of the parameters for both types is also provided. We find that the BDs that are related to PMJs are generally longer and have higher intensity enhancements. They are also more elongated (the ratio between length and width is higher). One of the distinguishable features is that most of the BDs that are related to PMJs show negative velocities (drifts toward the center of the sunspot).

### 6.2.4 Statistical behavior of PMJs and their connection to BDs

We have also calculated a few physical parameters of PMJs. The positions and lengths of the PMJs are measured in both the 2796 Å and Ca II H channels. The starting point of the PMJs is considered to be the location close to the center of the sunspot. The locations of the PMJ as seen in the Ca II H and 2796 Åchannels are marked (yellow arrows) in Figures 6.5(A) and (B), respectively. The length of the arrow measures the length of the PMJs. The BDs that are related to these PMJs are also shown by the small dots. Red represents the dots that move inward and blue represents those that move outward from the sunspot center. The PMJs as seen in 2796 Å generally show a spatial offset from the Ca II H PMJs along the PMJ direction (outer penumbral side). In Figure 6.5(C), we show the location of the BDs that are not related to any PMJs. Figure 6.5(D) shows the distribution of the length of the PMJs as seen in the 2796 Å and Ca II H images. The PMJs in Ca II H have similar values, as reported by Katsukawa *et al.* (2007) though they appear to be a little longer in the 2796 Å images. Figure 6.5(E) shows the distribution of the length between the BDs and the footpoint of the PMJs and Figure 6.5(F) shows the time delay between the appearance of the BDs and PMJs. A negative value means that BDs appear earlier than the PMJs. We find that most of the BDs appear before the PMJs.

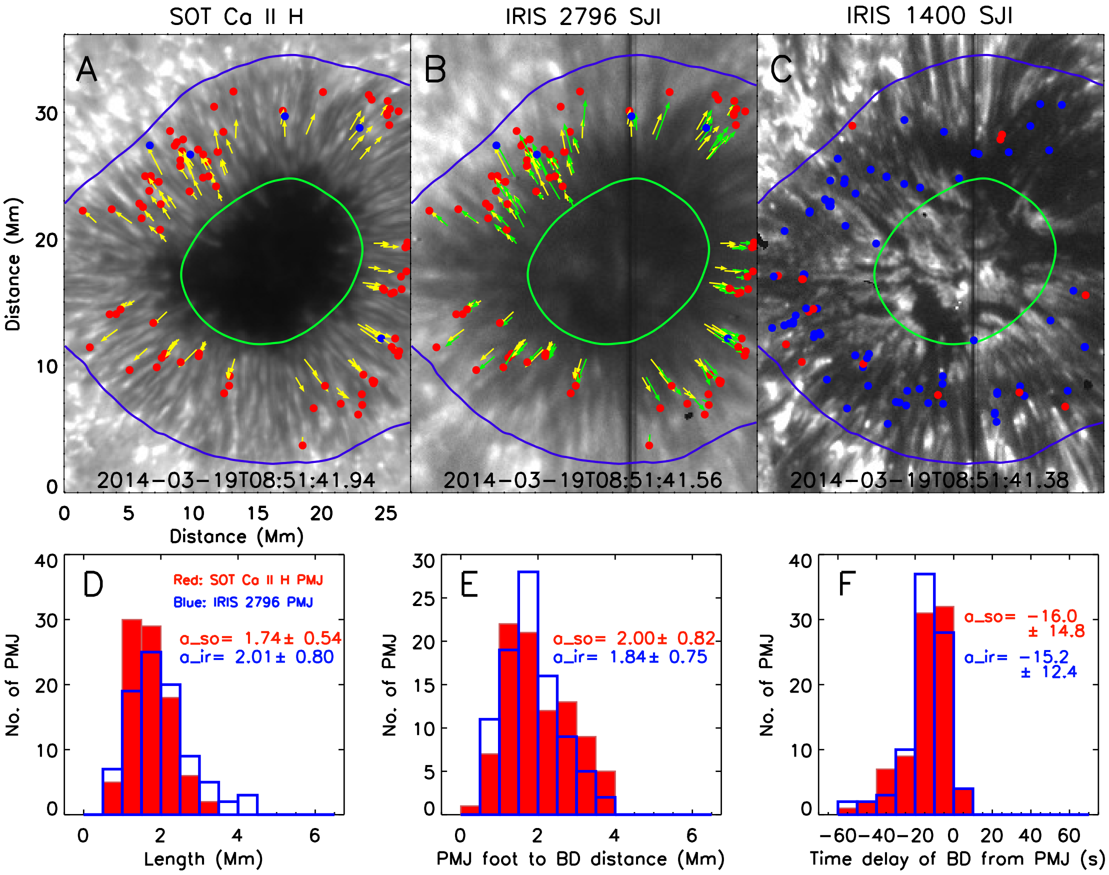

FIGURE 6.5: (A): The yellow arrows show the location of the PMJs as found in the Ca II H images and the dots (red/blue) show the location of the BDs as seen in the 1400 Å channels over the Ca II H image. Red dots represent the BDs that move in an inward direction (opposite of the PMJ's direction) and blue represents the BDs that move outward (along the direction of PMJs). (B): The yellow arrow and the dots (red/blue) show the location of Ca II H PMJs and 1400 Å BDs over the 2796 Å SJI. The green arrows represent the PMJs as observed in the 2796 Å images. (C): The BDs that do not have any visible counterparts in the Ca II H images are shown over the 1400 Å image. (D): The distribution of the length of the PMJs. (E): The distribution of the distance between the footpoint of the PMJs and starting location of the BDs. (F): The distribution of the time delay of the origination of BDs after PMJ. A negative value means that a BD originates earlier than a PMJ. All the PMJs and BDs are observed over the total observing window, whereas the background images are taken at t=0. The mean values of each parameter and also their standard deviations are printed. The *a_so* and *a_ir* represent the mean value as obtained from the SOT Ca II H and IRIS 2796 Å, respectively.

## 6.3 Summary

We have analyzed the properties of 180 BDs as seen in the 1400 Å images above a sunspot. Using our coordinated observations, we have also positively identified PMJs in the SOT Ca II H and IRIS 2796 Å images. We find that 90 BDs are related to PMJs, whereas others are not. A detailed analysis shows that the BDs that are related are generally longer and more elongated and have higher intensity enhancements. Most of these BDs show negative velocities (moves in an inward direction) and appear at the top of the PMJs. These BDs are found to be appear before the generation of the PMJs. These results may indicate that BDs could originate from a magnetic reconnection occurring at low coronal heights and/or be due to falling plasma. A component of the plasma from the reconnection site may move downward and reach the TR and show inward motion, as seen in the IRIS 1400 Å images. Finally, it reaches the chromosphere and appears as ribbon-like brightening (PMJ), which could explain the time delay in the appearance of the PMJs and their short lifetimes. Klimchuk (2006), Jiang *et al.* (2012), and Winebarger *et al.* (2013) proposed that this kind of small magnetic reconnection occurs in the low corona. This is in contrast to the reconnection model as proposed by Katsukawa *et al.* (2007). The progressive heating mechanism of the PMJs as proposed by Vissers *et al.* (2015) also may not explain the inward motions of the BDs, the appearance of BDs before PMJs, and the longer lifetime of the BDs. It is still unclear how the non-related BDs originate.

# Chapter 7

# Detection of high-frequency oscillations and thier damping in the corona[†]

## 7.1 Introduction

Since the first detection of coronal oscillations by Billings (1959) and their subsequent confirmation by Tsubaki (1977), there have been a number of observational pieces of evidence presented to verify the widespread existence of oscillations in the solar atmosphere. Using spectroscopic observation with a 40 cm coronagraph, Koutchmy *et al.* (1983) found velocity oscillations with periods of 300, 80, and 43 s, but no intensity oscillation in the green line (5303 Å). Rušin and Minarovjech (1994) reported intensity oscillations in the green line ranging from 5 s to 5 minute, which they proposed could result from the existence of waves or small-scale dynamic events like nano-flares. In the past, a number of researchers studied

---

[†] Results of this work are published in Samanta *et al.* (2016b).

the properties of high-frequency waves in the corona by taking images in the continuum, and green and red (6374 Å) emission lines during total eclipses (Singh *et al.* 1997; Pasachoff *et al.* 2002; Singh *et al.* 2009). Cowsik *et al.* (1999) detected intensity oscillations with frequencies in the range of 10 to 200 mHz during the 1998 total solar eclipse, while Sakurai *et al.* (2002) used spectroscopic data to detect Doppler velocity oscillation in the range of 1 to 3 mHz and 5 to 7 mHz in the localized regions, and they interpreted these variations as due to propagating waves and not to standing waves. Pasachoff *et al.* (2002) reported frequencies in the range of 0.75 to 1.0 Hz. Singh *et al.* (1997) found variations in the continuum intensity in six frequency components with periods 56.5, 19.5, 13.5, 8.0, 6.1, and 5.3 s. Shorter periodicities are also observed in the radio-band and in X-rays, particularly in the range of 0.5 to 10 s (Aschwanden 1987; Aschwanden *et al.* 2003). From space-based observation with EIS on Hinode, O'Shea and Doyle (2009) found oscillations over a broad range of frequencies (2 - 154 mHz) throughout an active region corona. They also noted that the higher frequency oscillations with frequency greater than 8 mHz, occur preferentially at the edges of bright loops. More recently, from a rocket experiment (Hi-C) that operated for several minutes, Morton and McLaughlin (2013) reported the detection of transverse waves with periods of 50 to 200 s.

Using the *Solar Eclipse Coronal Imaging System* (SECIS) instrument (Phillips *et al.* 2000) during the total solar eclipse in 1999, Williams *et al.* (2001, 2002) and Katsiyannis *et al.* (2003) reported propagating fast magnetoacoustic modes in coronal loops dominated by 6 s intensity oscillation. From the same instrument, Rudawy *et al.* (2010) found periodic fluctuations with periods in the range 0.1 to 17 s. Observational detection of these short-period waves using the SECIS instrument complements the theoretical work by Cooper *et al.* (2003). In their numerical work, Porter *et al.* (1994a,b) explored the processes of coronal heating by damping of the slow- and fast-mode high-frequency MHD waves. They concluded from simulation that MHD waves can deposit enough energy for heating under certain coronal conditions: the slow-mode waves with periods shorter than 300 s in the quiet regions and 100 s in active regions and fast-mode waves with periods shorter than 75 s in the quiet regions and 1 s in active regions can damp sufficiently fast to provide enough energy for balancing radiative losses. A year later, Laing and Edwin (1995a) showed that the Alfvénic-type waves with periods of a few seconds (2 - 10 s) only dissipate in weak magnetic fields ($<$ 15 G). In another article, Laing and Edwin (1995b) showed that acoustic-type waves can also dissipate if they have periods ranging from tens to hundreds of seconds (15 - 225 s). They achieved this range by varying plasma $\beta$, the ratio between gas pressure and magnetic pressure, in their model from 0 to 1, which is primarily dependent on the density, temperature, and magnetic field strength.

Several studies have been carried out during solar eclipses to detect high-frequency coronal waves using the visible emission lines, but their origin remains elusive. We still need to understand if they are present preferentially at specific times and locations, or if they are ubiquitous. To do this, it is important to study their temporal and spatial behavior, and more importantly, their damping because the damping of these oscillations alone can provide the requisite heating. We note that space-based EUV telescopes have a typical cadence of 10 s or longer, which makes it difficult to detect oscillations with periods shorter than 30 s. High-cadence observation of the corona can be achieved during total solar eclipses. The observations during total solar eclipses have the advantage that coronal emission line profiles are free from photospheric light scattered by the sky and provide ideal opportunities to study these variations. During the total solar eclipse on 11 July 2010, we have performed a spectroscopic observation of the corona with high cadence to study the high-frequency oscillations. The experimental set-up was similar to the experiment during 2009 solar eclipse as described in Singh *et al.* (2011). Instead of a single slit, this time we have used a multi-slit with a faster cadence to better understand high-frequency wave properties in the corona. The details of the experimental set-up are given in the 2.5. The slit locations are marked by the white lines on a broad-band image of the solar corona, as was obtained by Miloslav Druckmüller[*] form the Tatakoto Atoll, French Polynesia (Voulgaris *et al.* 2012; Habbal *et al.* 2011). The yellow portion marked on the first slit (S1) indicates the portion of the solar corona where the emission spectra was strong and where we were able to reliably analyze the data. The data reduction methods are described below.

## 7.2 Data Reduction

First, the coronal spectra and all the disk spectra were corrected for dark current by subtracting the respective dark signal. After this, the spectra from the four slits were divided into four spectral windows. The raw spectrum (first window) due to the first slit (S1) is shown in the Figure 7.2-(1). The use of narrow-band filters (IF2 and IF3) in front of CCD cameras (see the experiment setup in the 2.5) modified the continuum part of the spectra. We determined the transmission curve of each filter using the solar spectra at different parts of the corona inside our field of view (FOV). There was a small variation in the transmission curve of the filter as a function of the FOV, but it was possible to use the mean transmission curve of the filter for the observed solar corona. The intensity of the observed profile in the two wings of the spectrum away from the emission line was determined for each location on the slit, and then the transmission curve of the filter was normalized to match the observed intensity of the profile at these wavelengths. Then, the derived transmission curve was applied to the observed profile at each location on the slit to free the spectra from the effect of the transmission curve of the filter. The corrected spectrum after accounting for the transmission curve of the narrow-band interference filter is shown in Figure 7.2-(2).

---

[*] `http://www.zam.fme.vutbr.cz/~druck/eclipse/Ecl2010t/Tse2010t_1000mm_1/0-info.htm`

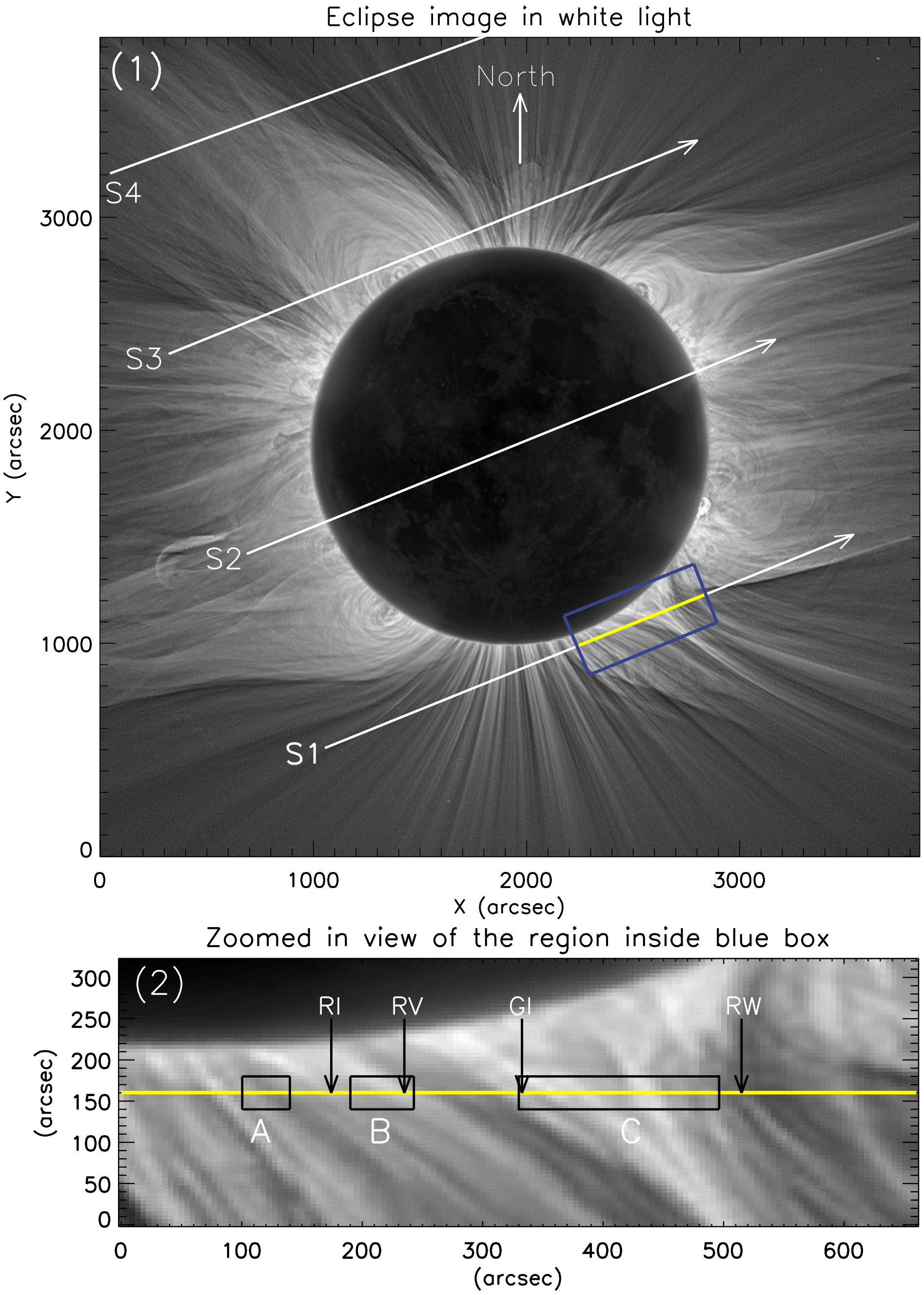

Figure 7.1: (1): White-light image of the corona taken during the total eclipse of 11 July 2010. This image was obtained by Miloslav Druckmüller form the Tatakoto Atoll, French Polynesia. The positions of the four slits (S1S4) from our spectroscopic experiment set-up are shown by the white lines. The yellow line (along S1) marks the region where the signal is good. This is our region of interest (ROI). The arrow indicates ascending pixel numbers along the length of the slit. The lower panel (2) shows a zoomed-in view of the blue box that is marked in the upper panel. The RI, RV, RW, and GI arrows marked on the slit show the locations where we performed wavelet analysis, and the results are shown in Figure 7.4, 7.5, 7.6 and 7.7. A, B, and C indicate three structures as identified from the intensity space-time plot of the red line (see Figure 7.8).

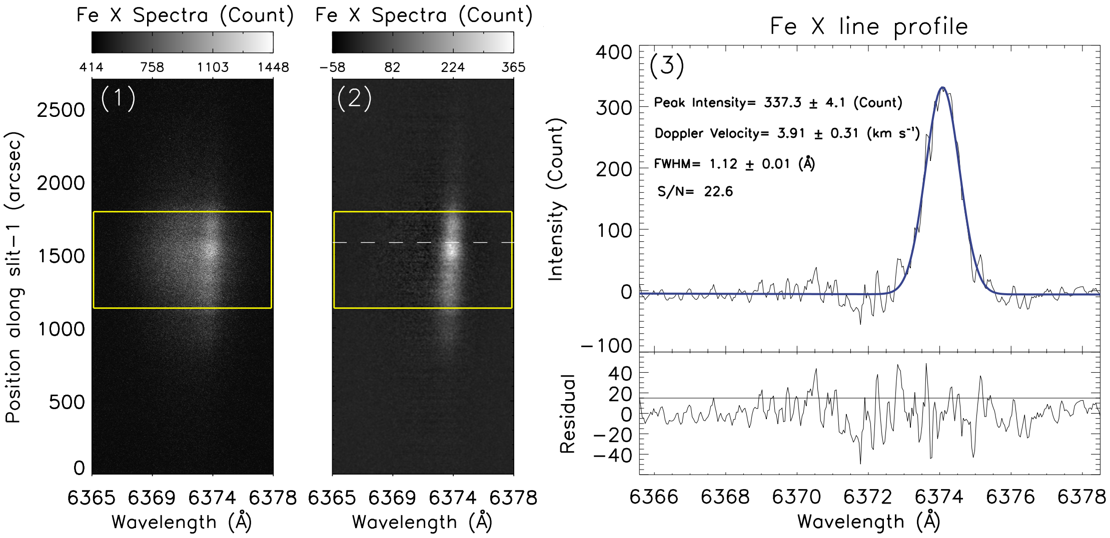

FIGURE 7.2: Panel (1) shows the raw red line spectrum taken with the first slit (S1) recorded during the total phase of the solar eclipse. Panel (2) shows the spectrum after accounting for dark current and the transmission curve of the narrow-band interference filter. The line profile along the white dashed line is shown in the right panel. The yellow rectangular box shows our ROI in the blue box shown in Figure 7.1. (3) The top panel shows the red line profile. The Gaussian fit to the profile is drawn in blue. Extracted line parameters from the line profile fitting are printed. The bottom panel shows the residual between the fitted curve and the original line profile. The horizontal line represents the absolute standard deviation of the residual.

Gaussian fits were applied to the line profiles at each pixel to derive the peak intensity, line width (FWHM), and Doppler shift of the emission lines centroid with respect to the reference wavelength. We averaged all the Gaussian peak positions to determine the reference wavelength of the lines. The averaged line centres are taken as 6374.4 Å and 5302.8 Å for the red and green line, respectively. The upper panel of Figure 7.2-(3) shows an example of the red line profile after correction for the dark current and the transmission curve of the narrow-band interference filter. The blue curve represents a Gaussian fit to the line profile. All the extracted line parameters and their fitting errors ($1\sigma$) in the measurements are printed in the same panel. The signal-to-noise ratio (S/N) is also given. After extracting the line parameters for each of the locations on slit 1 for each time frame, the temporal evolution along the slit is shown in the upper panel of Figure 7.3. The sky conditions were good, but sudden drops of intensity during the middle

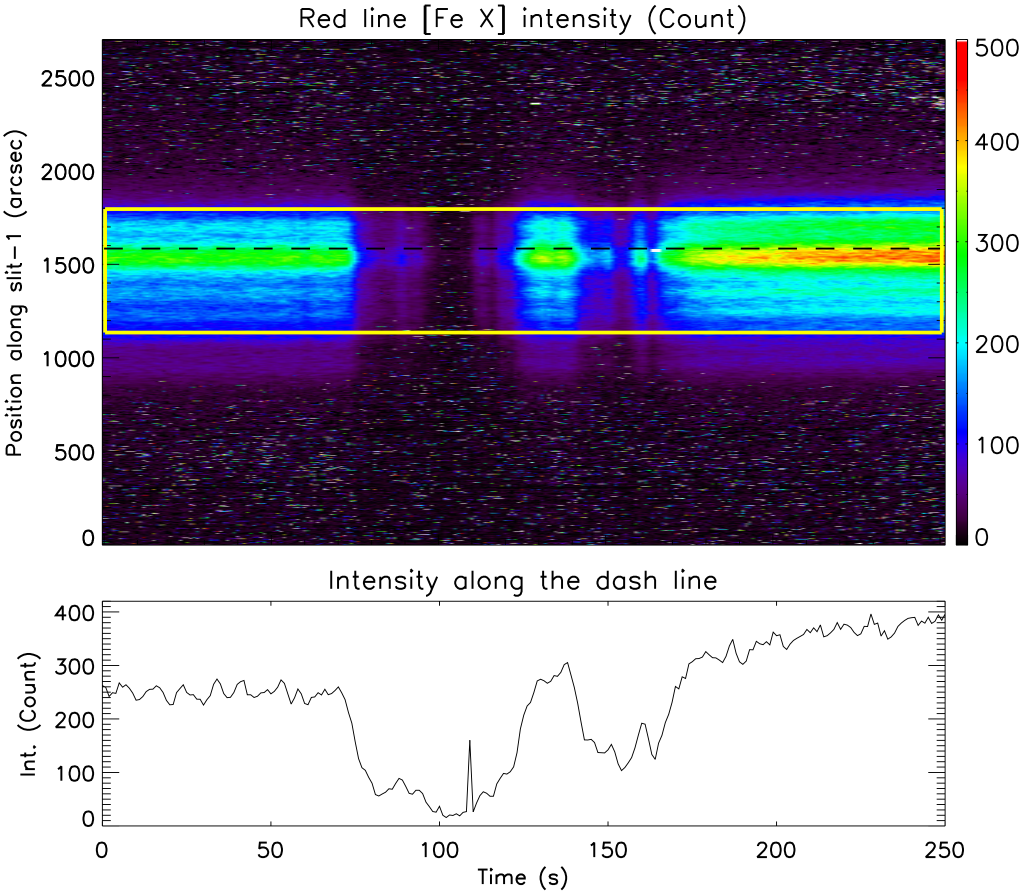

FIGURE 7.3: The upper panel shows the temporal evolution of the red line intensity at each pixel along slit 1. The origin of this plot is used as reference for selecting the time interval and choosing the spatial locations for all the further analysis. The bottom panel shows the intensity variations along the horizontal black dashed line. The sudden drops of intensity during the middle part of the totality are due to passing clouds that reduced the intensity. The yellow rectangular box shows the ROI as mentioned in Figure 7.1.

part of the totality indicate thin passing clouds that reduced the intensity at those times. The bottom panel shows the intensity variation at a typical location during our observation. The low signal during the passing of the cloud did not permit a good fit to the emission line. We therefore obtained good data in two time intervals, both of 70 s duration (the first and last 70 s of the totality). We separately analyzed these two data sets only in the region inside the ROI. The S/N in these two intervals varies from 8 to 29.

## 7.3 Results

### 7.3.1 Detection of oscillations

We applied the wavelet technique (Torrence and Compo 1998) for the time series analysis at each location inside the ROI and for each line parameter (peak intensity, FWHM, and Doppler velocity). We used a Morlet function, which is a complex sine wave modulated by a Gaussian, for convolution with the time series in the wavelet transform. Figure 7.4 shows a typical example of the result from the wavelet analysis. In the top panel, the variation of intensity with time (I) and the background trend ($\mathrm{I}_{bg}$) are shown. The middle panel shows relative intensity variations ($I_R$) with respect to the background trend ($I_R = [I - I_{bg}] * {I_{bg}}^{-1} * 100~\%$). The cross-hatched region in the wavelet power spectrum, called cone of influence (COI), is the region where the power is not reliable, and it is caused by the finite length of the time series. The bottom right panel shows the global wavelet power, which is the time-averaged wavelet power at each period scale. The dotted line above the global wavelet power plot shows the significance level of 99.99 % calculated by assuming white noise (Torrence and Compo 1998). The white noise is a random distribution about the mean of the original time series, which has a flat Fourier spectrum. If a peak in the wavelet power spectrum is significantly above this background white-noise spectrum, then it is assumed to be a real feature with a certain percentage of confidence (see Torrence and Compo (1998) for details). Because the total duration of the time series is 70 s, the COI effect restricts us to measuring the significant period only up to 25 s. Keeping this in view, we subtracted a 30-point running average (the background trend) from the original time series to suppress variations above 30 s from the time series. The final result of the analysis shows that an oscillation with 14 s periodicity is present in the intensity variation throughout the observing period of 70 s. Similarly, Figures 7.5 and 7.6 show that 16 and 15 s periodicities are present in the Doppler velocity and

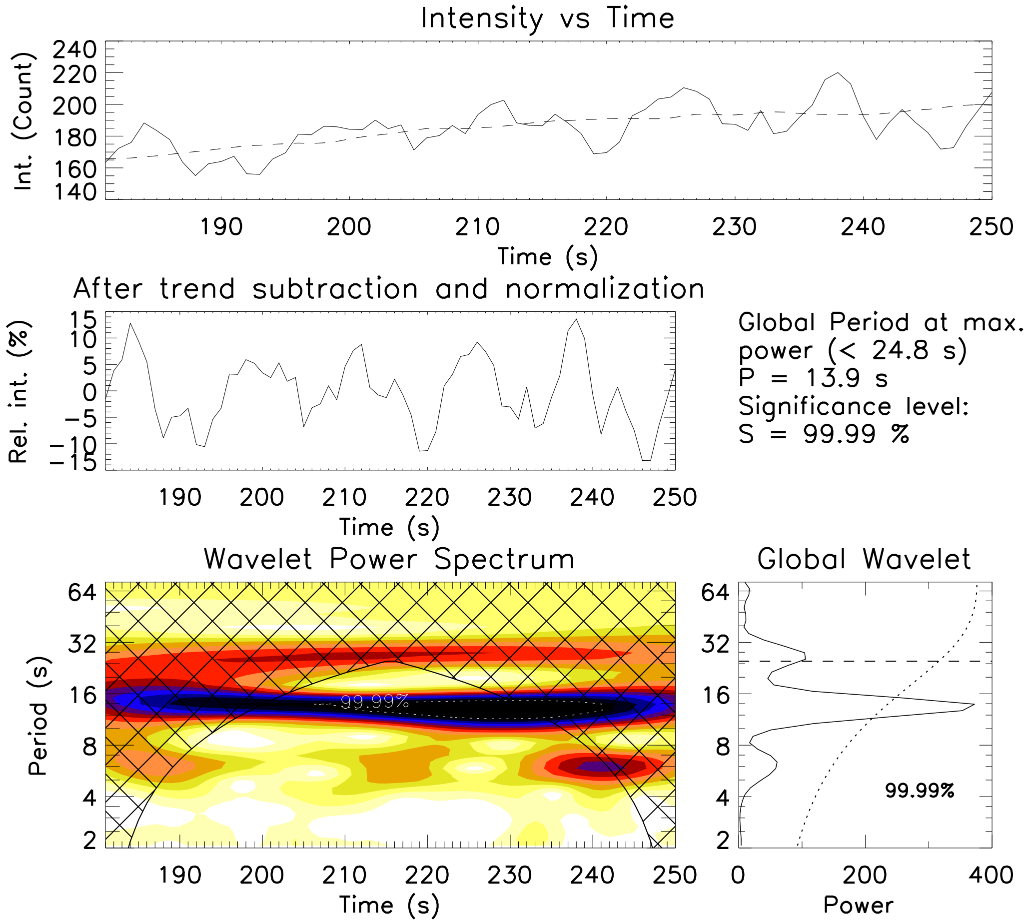

FIGURE 7.4: A typical example of wavelet results for the location RI (marked in Figure 7.1) and in the red line. In the top panel the variation of intensity with time is represented by a solid line. The dashed line represents a background trend. The middle panel shows the normalized intensity variation. The bottom left panel shows the wavelet power spectrum of the normalized time series. Overplotted cross-hatched region above the wavelet power spectrum shows the cone of influence (COI). The location of power above 99.99 % significance level is indicated by the region overplotted with dotted white lines. Note that darker colour represents higher power. The bottom right panel shows the global wavelet power. The longest measurable period is 24.8 s (due to the COI), which is shown by a horizontal dashed line. The dotted line above the global wavelet power plot shows the significance level of 99.99  The significant periods as measured from the global wavelet power are shown at the top of the global wavelet power plot. Note that the power is unitless because the wavelet transformation is applied to normalized time series.

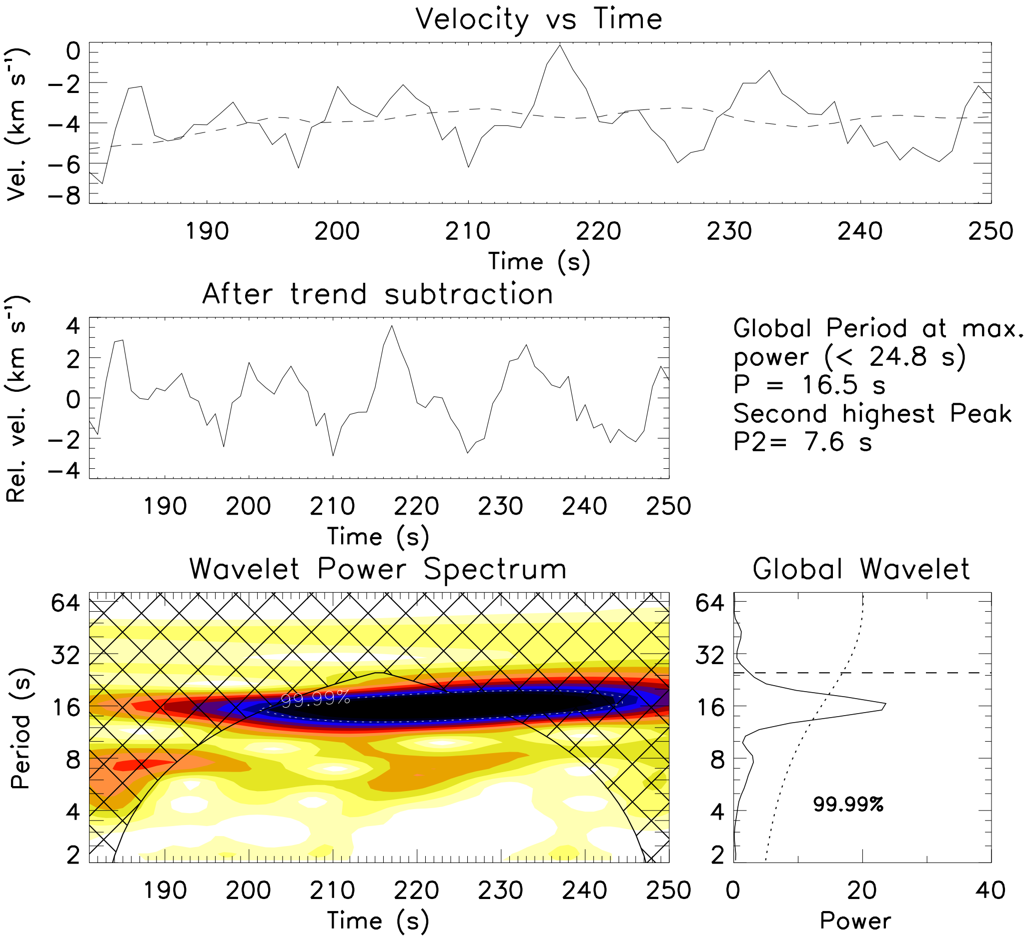

FIGURE 7.5: A typical example of the Doppler velocity variations of the red line and their wavelet analysis for the location RV indicated in Figure 7.1. The panels are the same as in Figure 7.4.

FWHM variations, respectively.

A typical example of the wavelet analysis for the green line intensity oscillation is shown in Figure 7.7. The green line spectra were taken with a different camera with a lower cadence of 3.64 s. We had fewer data points for the green line than for the red line, whose cadence was 1.013 s, therefore the confidence level for the detection is not as good as for the red line. We studied the oscillations in all the green line parameters. The result shows that oscillations are detectable for all the line parameters with periods ranging from 1025 s, but we have used a lower significance threshold of 99 % for detection. Hereafter, we concentrated on red line data because they have more data points and provide a reliable confidence level.

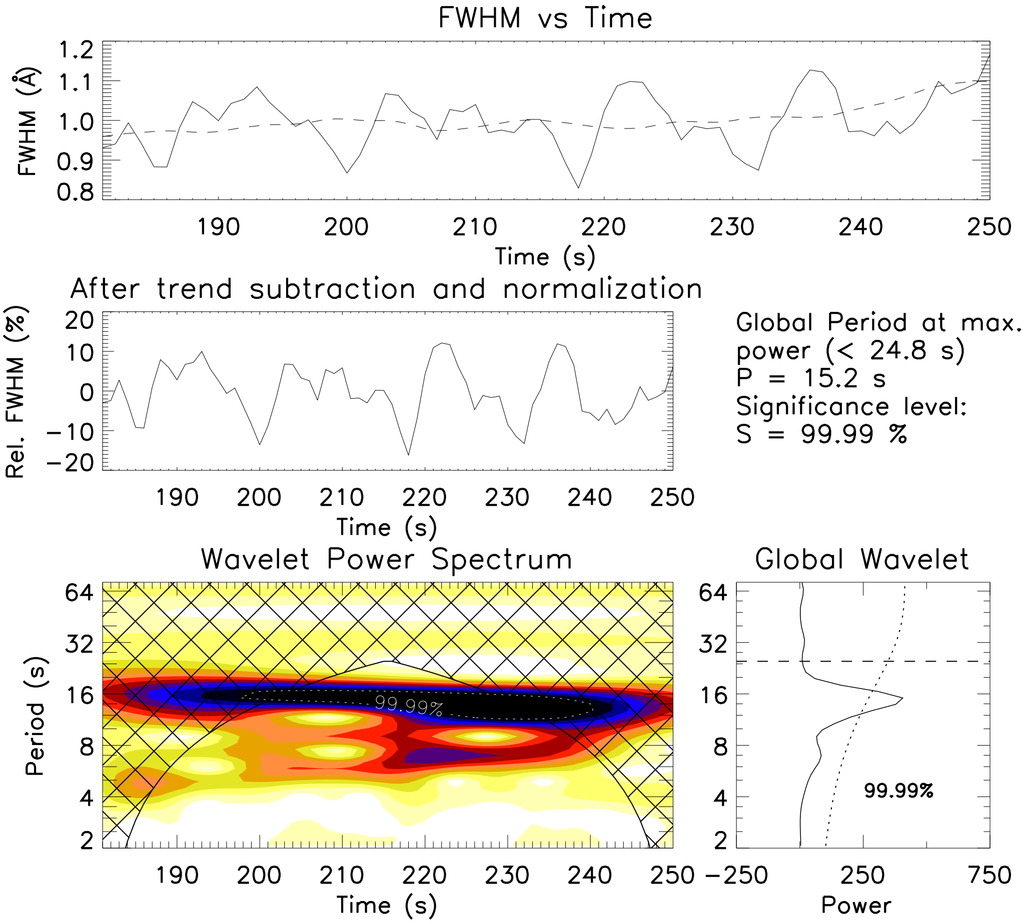

FIGURE 7.6: A typical example of the FWHM variations of the red line and their wavelet analysis for the location RW indicated in Figure 7.1.The panels are as in Figure 7.4.

In this section we have shown that we detected significant oscillations at isolated points, but for a proper diagnostics of the wave modes that might be responsible for these oscillations, we need a more statistical approach. We address this in the following subsection.

### 7.3.2 Statistical behavior of the oscillations

In this subsection, we study the statistical properties of the oscillations and whether these oscillations are preferentially located within some structures or near the boundaries. To do this, we produced a space-time (XT) map from the red line

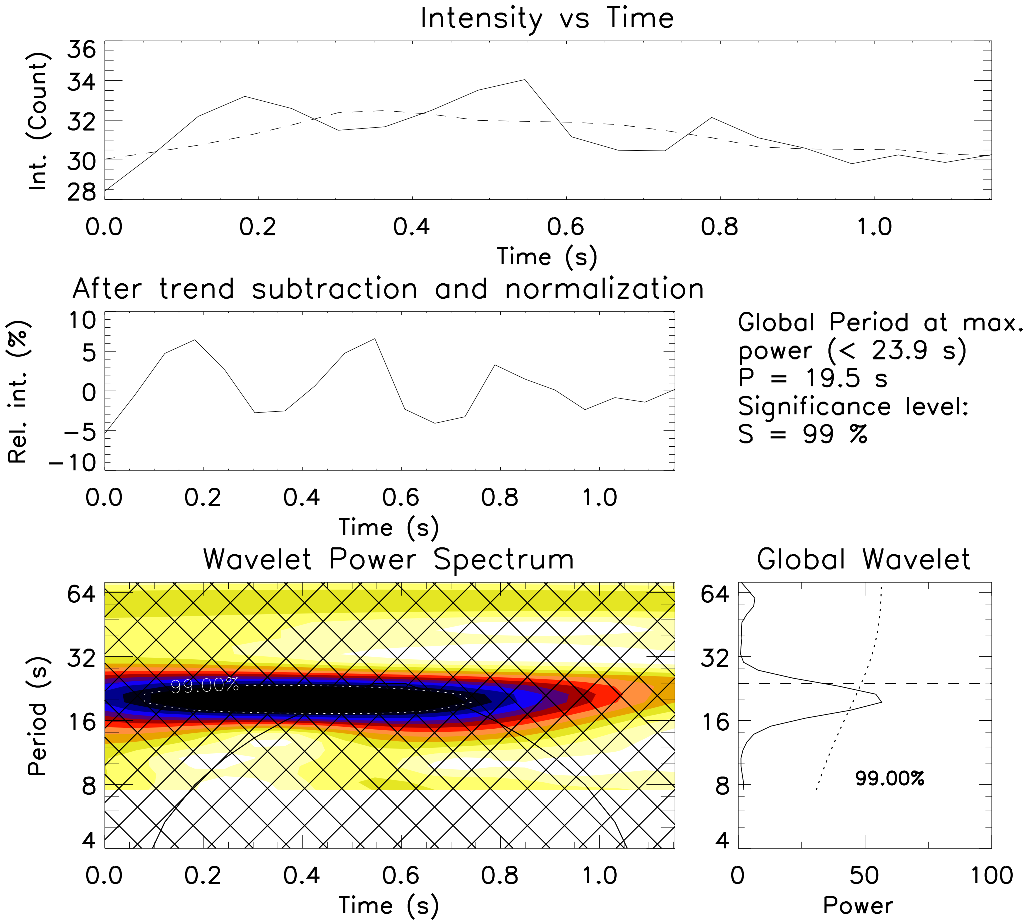

FIGURE 7.7: A representative example of intensity variations as recorded from the green line spectra and their wavelet analysis results for the location GI indicated in Figure 7.1. The panels are same as in Figure 7.4.

intensity within the ROI. The first panel (from the left) of Figure 7.8 shows the temporal evolution of intensity along the slit (intensity XT map) for the final 70 s of totality. The time-averaged intensity profile along the slit (S1) is shown in the second panel. Its variations along the slit indicate that the slit crosses some structures; this is also clear from the context white-light eclipse image (Figure 7.1). From the intensity variation along the slit, we identified three structures A, B, and C. We should point out that determining the exact boundary is not possible from our sit-and-stare observation. We do not have simultaneous imaging observations from the same location, and hence we can only indicate the approximate boundary from the intensity variation along the slit. Furthermore, the red line emission profile (variation along the slit) may not exactly match what we see in

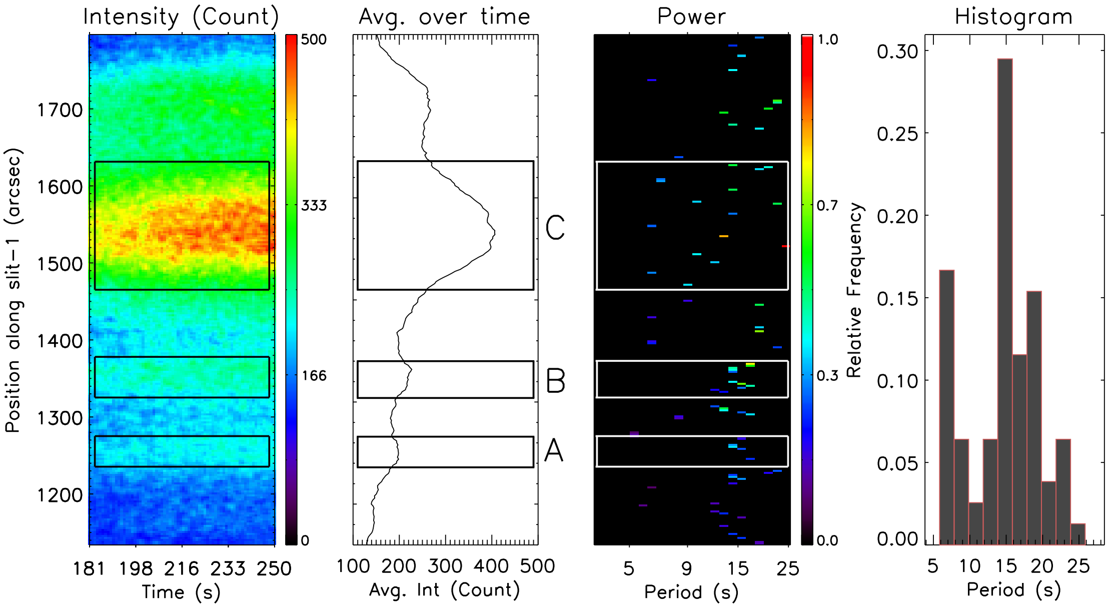

FIGURE 7.8: *Left to right:* The first panel shows the temporal evolution of the red line intensity along slit 1. This is similar to Figure 7.3, but for a region inside the ROI and for the last 70 s time interval of totality. The second panel shows the time-averaged intensity variation along the slit. The third panel shows the dominant periods of oscillation above the 99.99 % significance level. Color indicates the amplitude of the power (normalized). The last panel shows a distribution histogram the significant periods.

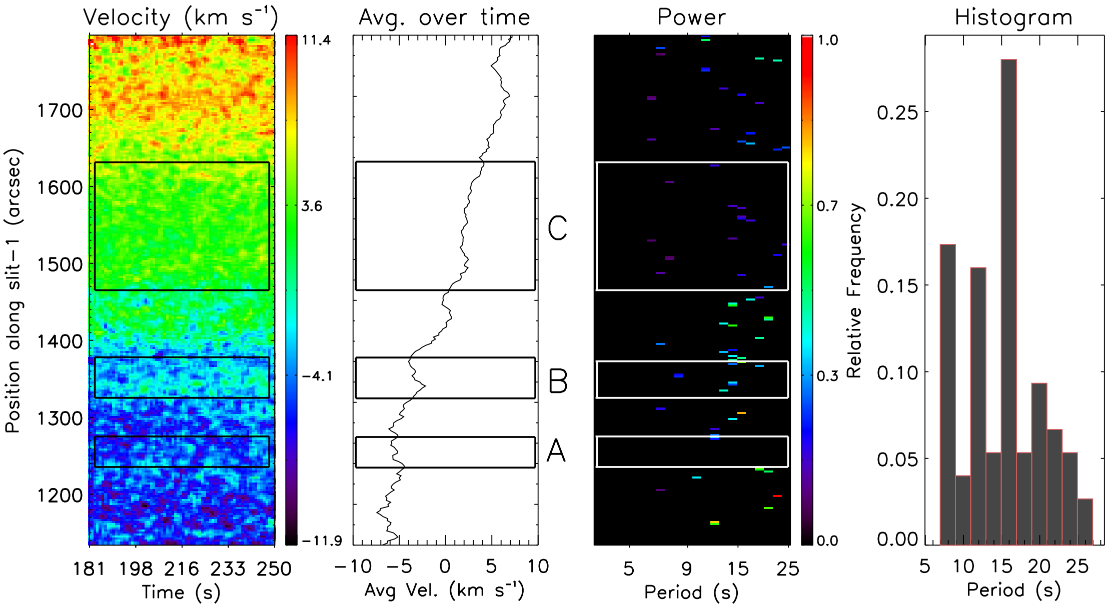

FIGURE 7.9: Similar to Figure 7.8, this shows the temporal variations of the Doppler velocity along the slit and the statistical behavior of the oscillations.

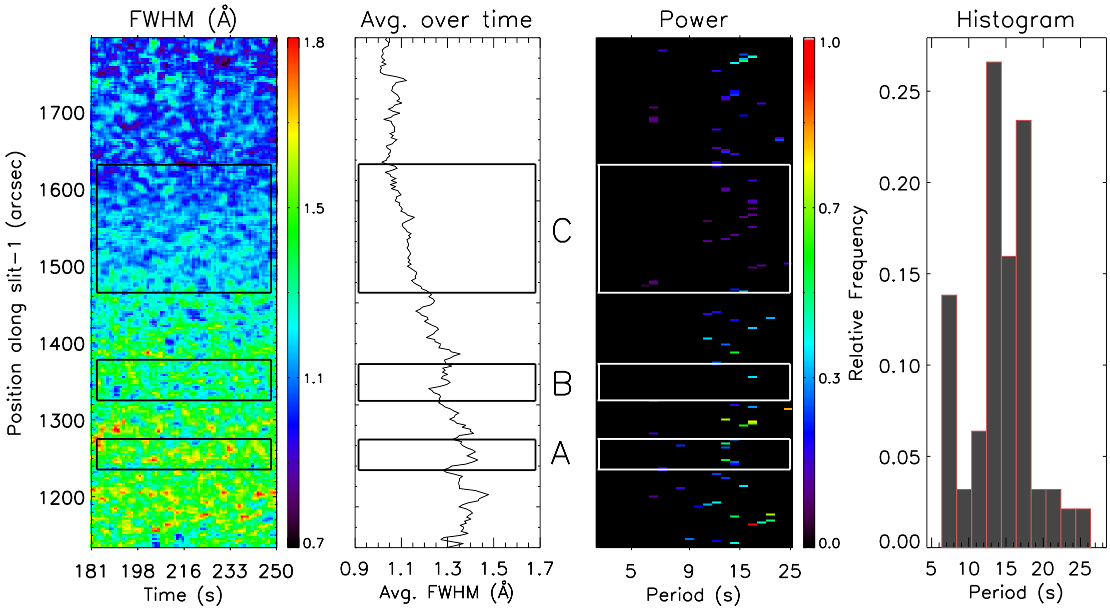

Figure 7.10: Similar to Figure 7.8, this shows the temporal variations of FWHM along the slit and the statistical behavior of the oscillations.

white-light images. In Figures 7.8, 7.9 7.10 and 7.14 the rectangular boxes from bottom to top represent structures A, B, and C, respectively. Structure C is wider and may have more than one overlapping structure.

We performed a wavelet analysis to locate oscillation signatures at each pixel along the slit within the ROI to determine the distribution of the period of oscillations and their power. First, we calculated a global wavelet power spectrum at each pixel and then determined the power map by the pixels where the global power exceeds the significance level. The third panel of Figure 7.8 shows the power map for the intensity variations. This figure provides an overview of the power distribution at different locations along with significant periodicities. The third panels of Figures 7.9 and 7.10 show the spatial distribution of power for Doppler velocity and width oscillations, similar to the power distribution for intensity shown in the third panel of Figure 7.8. The power map of intensity variations shows that the intensity oscillations have a slight preference to occur in the thinner structure A and B, but not in the wider structure C, while the FWHM and Doppler velocity power maps show that they have a slight tendency to occur close to the boundaries of the structures where the intensity gradient is relatively high. The result is only based on a comparison of three coronal structures. Hence we are unable to conclude further on the statistics. We also note that the oscillations at periods shorter than 12 s are barely present in A and B, but are more frequent in the extended structure C. It has been pointed out (O'Shea *et al.* 2001; Singh *et al.* 2009; O'Shea and Doyle 2009; Rudawy *et al.* 2010) that the intensity oscillations are significantly prevalent at the edges of bright coronal loops.

To find the distribution of the time periods, we made a histogram plot with a 2 s binning in the time period domain. The histograms for the intensity, Doppler velocity, and width oscillations are shown in the last panels of Figures 7.8, 7.9 and 7.10 respectively. They provide an estimate on which periodicity is statistically most prevalent. They mostly show two peaks, one around 14 to 20 s, and the other around 6 - 8 s. Williams *et al.* (2001) reported a peak around 6 s in the intensity oscillation data.

### 7.3.3 Damping signature of the oscillations

One of the possible coronal heating sources is the damping of MHD waves. To search for the damping signature in the data, each time series at each location was inspected visually. Damped temporal samples were fitted with a damped sine function (Equation 7.1) using the MPFIT programme in IDL. Here $A_0$ is the mean, A is the amplitude at time zero, D is the total duration, P is the period of oscillation, $\phi$ is the phase at time zero and $t_d$ is the damping time. The average trend was subtracted before fitting. Figure 7.11 and 7.12 show that the intensity oscillations and Doppler velocity oscillations damps significantly at a few locations. The locations of the damping are shown in Figure 7.13. We did not

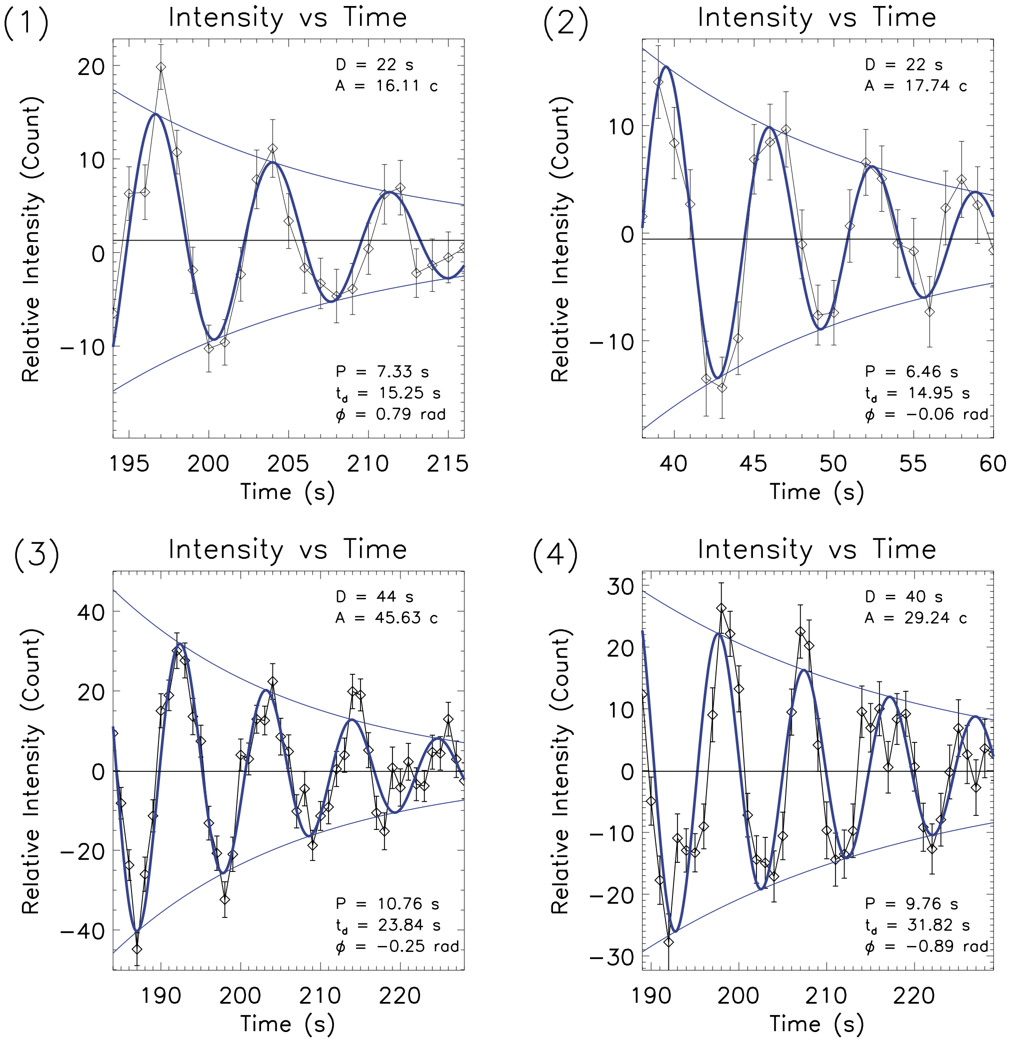

FIGURE 7.11: Examples of damped intensity oscillations. The locations of the occurrences (1-4) are shown by the arrow marks I1, I2, I3, and I4 in Figure 7.13. The data points (diamonds) are fitted with damped sine functions (see Equation 7.1) represented by thick blue curves. The error bars calculated from Gaussian fitting are also shown. The damping parameters from the fitting are shown in each panel.

find any damping signature of FWHM variations.

$$f(x) = A_0 + ASin(\frac{2\pi}{P} + \phi)e^{-\frac{t}{t_d}} \tag{7.1}$$

It is likely that damping signature of oscillations is due to MHD wave damping within coronal structures, and they can play an important role in coronal heating.

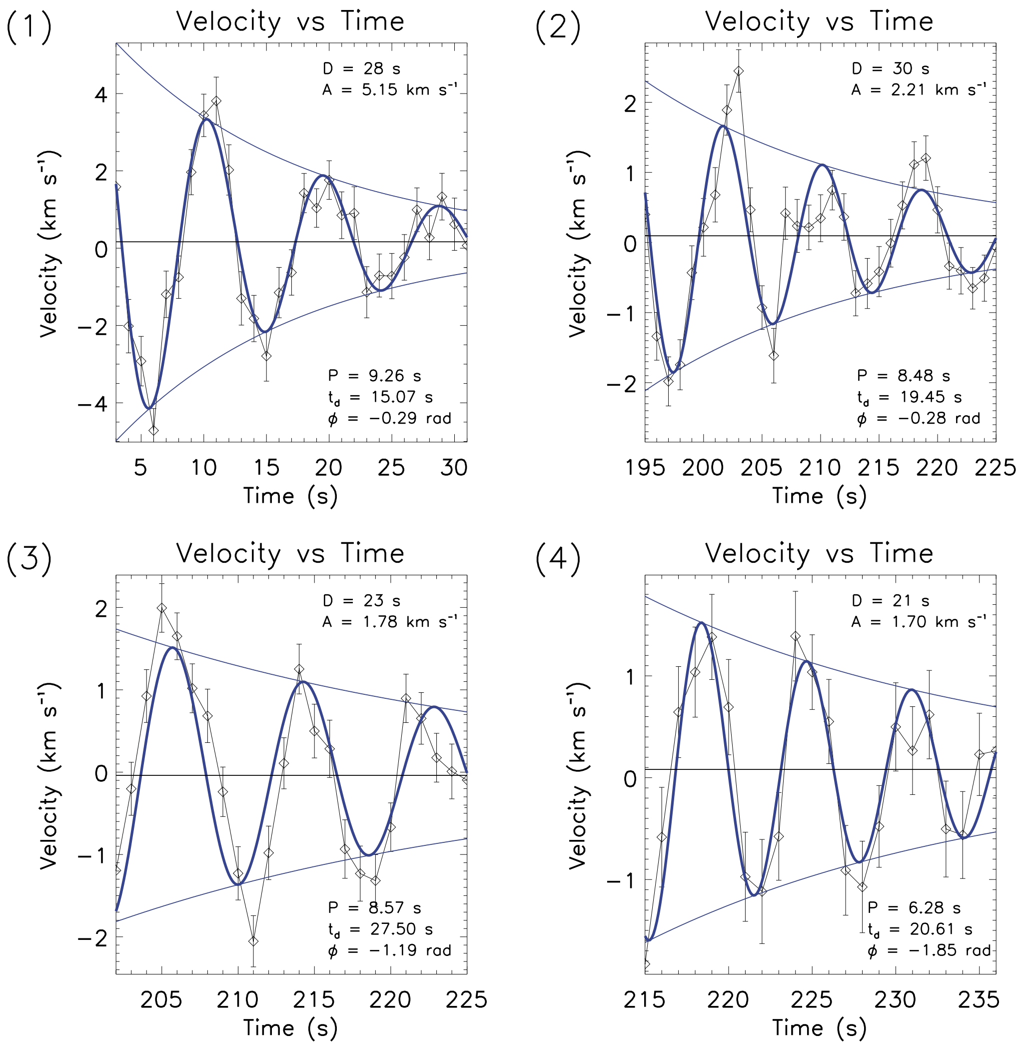

FIGURE 7.12: Four events show that Doppler velocity oscillations are damping significantly with time. The locations of events (1-4) are shown by the arrow V1, V2, V3, and V4 in Figure 7.13. The panels are similar to those in Figure 7.11.

The damping parameters and the quality factor (the ratio of damping time over the oscillation period) are given in Table 7.1. Damping parameters can provide valuable information about physical parameters such as the electron density and filling factors etc (Aschwanden 2006). Figure 7.13 shows that the damping of the intensity and Doppler velocity oscillations are generally occur at locations with high intensity gradients. It may be resonant damping that is induced by the higher density gradient (Aschwanden *et al.* 2003).

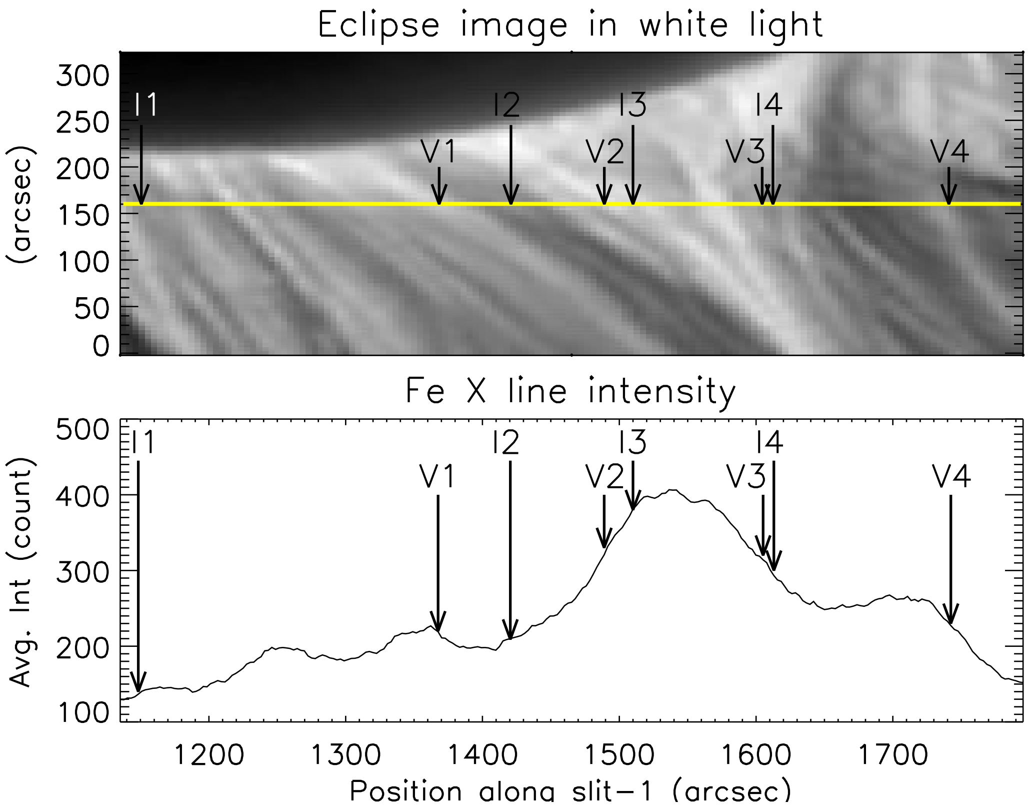

FIGURE 7.13: The top and bottom panels are enlarged parts of Figures 7.1 and 7.8, respectively, used to indicate the locations of the damping events shown in Figures 7.11 and 7.12. Arrows I1 to I4 show the locations of four intensity damping events (1-4), as shown in Figure 7.11. Arrows V1 to V4 show the locations of four Doppler velocity damping events (1-4) presented in Figure 7.12. The damping parameters are listed in Table 7.1.

TABLE 7.1: Damping properties. Locations of the events are shown in Figure 7.13.

| Parameter | Loaction | Periods | Damping time | Quality factor |
|---|---|---|---|---|
| Intensity | I1 | 7 | 15 | 2.14 |
| | I2 | 6 | 15 | 2.5 |
| | I3 | 11 | 24 | 2.18 |
| | I4 | 10 | 32 | 3.2 |
| Doppler | V1 | 9 | 15 | 1.66 |
| Velocity | V2 | 9 | 19 | 2.11 |
| | V3 | 9 | 28 | 3.11 |
| | V4 | 6 | 21 | 3.5 |

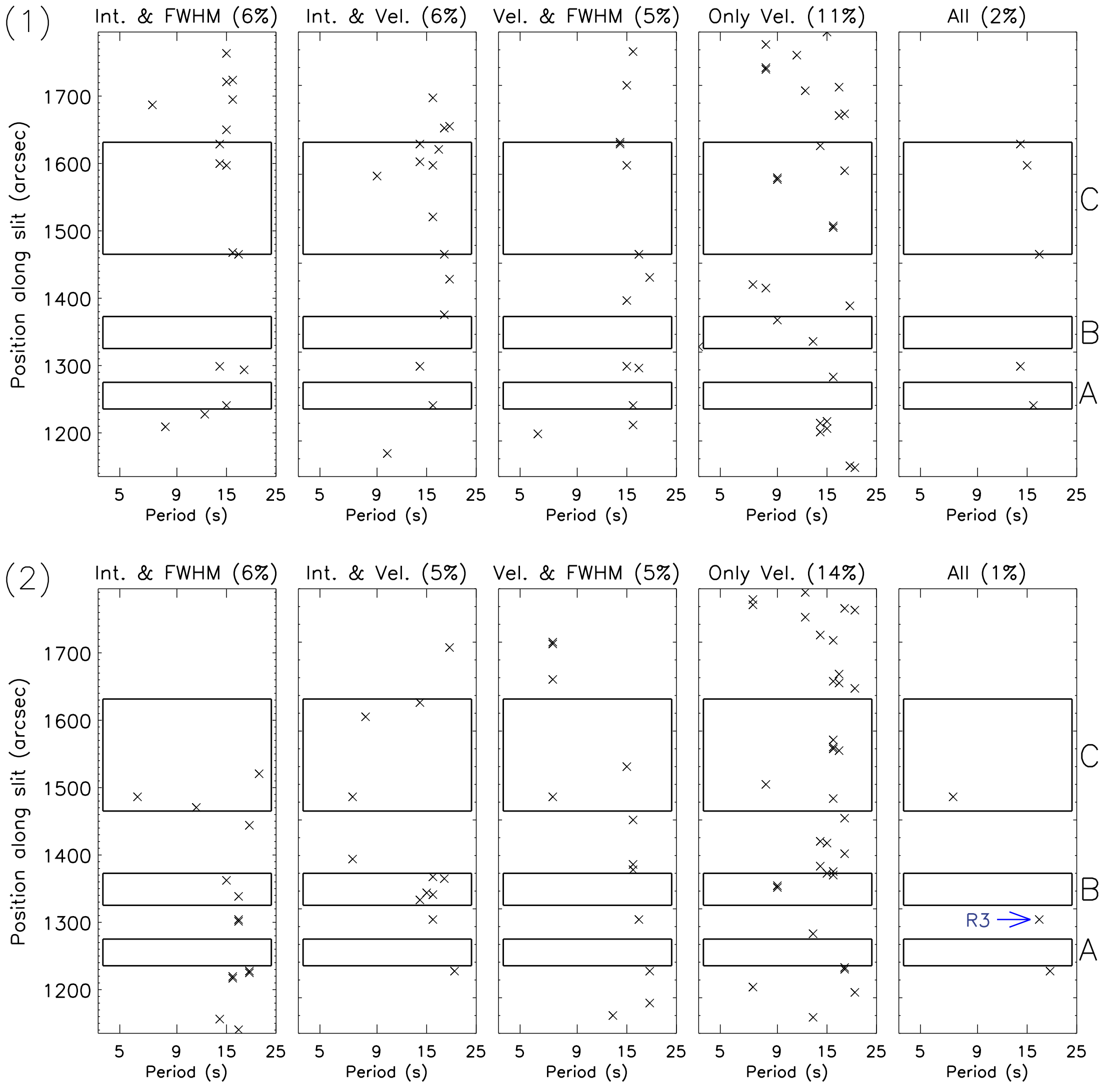

Figure 7.14: The top row (1) corresponds to the analysis result for the first 70 seconds of totality, the bottom row (2) corresponds to 181 to 250 s of totality. From left to right: the locations where both the intensity and width oscillations are present with identical periods, the second panel showing the locations where both intensity and Doppler velocity oscillations are present with identical periods, the third panel showing the locations where both width and Doppler velocity oscillations are present with identical periods, the fourth panel shows the locations where only Doppler velocity is present, and the last panel shows the locations where oscillations are present with identical periods in all the parameters. The numbers in parentheses at top of each panel represent the percentage of pixels where we detect significant oscillation.

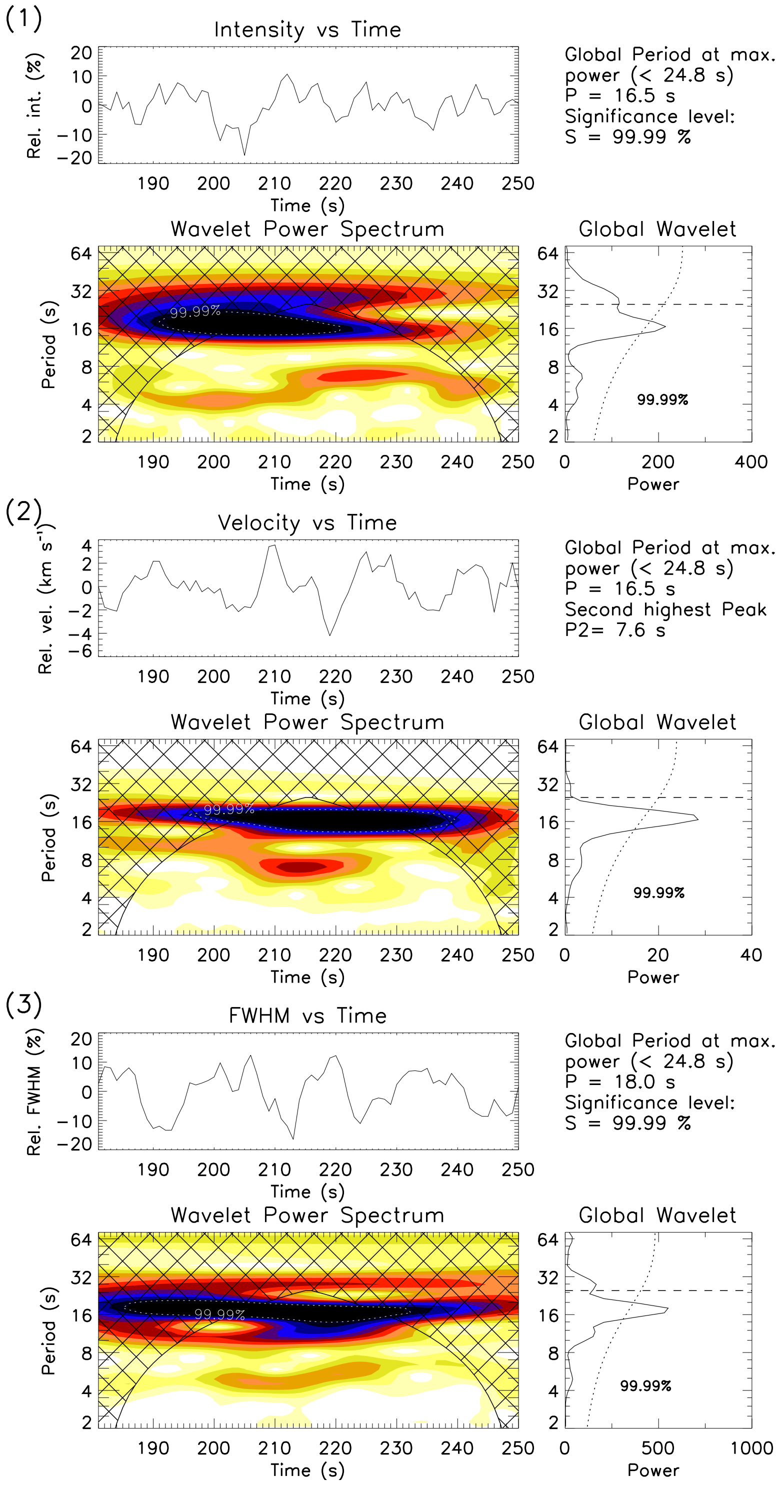

FIGURE 7.15: Panel (1) shows the result from the wavelet analysis of the intensity variations similar to Figure 7.4. Similarly, panel (2) shows the result from Doppler velocity variations and panel (3) those from FWHM variations. All the light curves of different line parameters are shown from a particular location that is shown by the arrow R3 in Figure 7.14 (2). The analysis shows that oscillations with identical periods are present in all the line parameters.

### 7.3.4 Oscillation in different line parameters with identical periods

Coronal structures can support different MHD wave modes (Nakariakov and Verwichte 2005). The observational signatures are different for each wave mode (Kitagawa *et al.* 2010). To identify MHD wave modes, we compared the time periods of the significant oscillations of the parameters at each pixel location inside the ROI. In this case, we assumed that while determining the periods of the significant oscillations there can be a scatter error, and we assumed this to be the nearest period (resolution) in the wavelet period spectrum. The periods that correspond to detections in individual parameters and their combinations are plotted against the period and slit coordinate in Figure 7.14. According to the MHD wave theory (Nakariakov and Verwichte 2005),generally, intensity and FWHM oscillations are associated with the fast sausage mode, intensity and Doppler velocity oscillations are associated with the slow acoustic mode, Doppler velocity shift and FWHM oscillations are associated with the torsional Alfvén mode, and only Doppler velocity shift oscillations are associated with the kink mode.

In the rightmost panel of Figure 7.14 (2), we show the locations where we find oscillations in all the three line parameters with identical periods. A representative example is shown in Figure 7.15: there are similar periodicities in different parameters. The correlation analysis shows that the intensity and velocity oscillations are in phase (correlation coefficient (C.C.) = 0.42), and intensity and FWHM oscillations are in opposite phase (C.C.= -0.52), and velocity and FWHM are in opposite phase (C.C.= -0.64) as well, which might indicate a common origin of these oscillations. The correlated oscillations between all the parameters seem to be located close to the boundaries of the streamer structure.

## 7.4 Discussion

From a total solar eclipse expedition and using a multi-slit spectrograph, we have studied the oscillation properties of the coronal plasma. We found that the intensity, Doppler velocity, and width show significant oscillations with periods ranging from 6 - 25 s at many locations in the red line. The green line parameters also show periodic oscillations between 10 - 25 s at different locations. These oscillations can be interpreted as magnetohydrodynamic waves in the corona. Our statistical analysis shows that the intensity and Doppler velocity oscillations are more frequent around 15 and 6 s, but less frequent around the 10 s periods. Maybe the periods around 10 s are damped more effectively, making them difficult to be observed.

The power and period distributions of intensity, Doppler velocity, and width variations (Figure 7.8, 7.9 and 7.10) reveal that they have a slight tendency to occur preferentially close to the boundaries of the structures where intensity gradients are relatively high. This result confirms earlier observations (O'Shea *et al.* 2001; Singh *et al.* 2009; O'Shea and Doyle 2009; Rudawy *et al.* 2010), although they were limited to intensity only. O'Shea and Doyle (2009) reported a variation of wave mode with frequency and location. The wave mode was found to change from slow magnetoacoustic waves in the plage regions to fast magnetoacoustic waves at structure boundaries. Their analysis also showed that higher frequency oscillations greater than 8 mHz occur preferentially at the edges of moss areas, which they interpreted as due to resonant absorption. We point out that if there are multiple finer structures along the line of sight as well as across it, wave detections may be difficult because signals are out of phase and polarised in different directions, and the resulting oscillation signatures may cancel out. At the edges of a large structure, where the line of sight passes through fewer substructures, however, the wave signature is retained and will be easier to detect. While performing a numerical experiment, De Moortel and Pascoe (2012) have demonstrated this effect.

This means that the absence of the wave signature within structures can also be due to a line-of-sight effect.

High-resolution spectroscopy and sufficiently high cadence have enabled us to find evidence of strong damping. To our knowledge, we detected the damping of high-frequency oscillations with periods around 10 s for the first time. These results therefore provide additional evidence in favour of high-frequency wave damping in the corona, which has been demonstrated by Porter *et al.* (1994a,b) and Laing and Edwin (1995a,b) to be a necessary condition for waves to heat the solar corona. We find that only the intensity and Doppler velocity oscillations are damping significantly at a few locations. The observed intensity oscillations can be due to either the fast magnetoacoustic mode (Cooper *et al.* 2003) or to the fast kink mode (Van Doorsselaere *et al.* 2008) if the oscillating plasma moves in and out of observing pixel position. The Doppler velocity oscillations are more likely due to the fast kink mode. The fast magnetoacoustic mode can be damped by shocks (Nakariakov and Roberts 1995). Our analysis also shows that the damping events are generally located where intensity gradients are high. It is possible that the kink waves are damped by resonant absorption that is due to the higher density gradient (Ruderman and Roberts 2002; Goossens *et al.* 2002; Aschwanden *et al.* 2003). The kink mode generally oscillates in transverse direction (Aschwanden *et al.* 1999), although a clear signature of oscillation in vertical direction was also found (Wang and Solanki 2004). Hence, they have a different plane of oscillation (different polarization) and can cancel out the signal from the bright overlapping loops. This effect also can contribute to the detection of damping close to the boundaries where the line-of-sight signal passes through fewer substructures, while inside the bright structure it passes through multiple loops.

The periods and damping times of MHD modes are dependent on the plasma densities inside and on the surroundings of the oscillating structures. Damping parameters provide information about physical parameters such as the electron density and filling factors (Roberts 2000; Aschwanden 2006). As the fast kink mode has relatively short damping times and hence is rarely detectable. The ratio between periods and damping times, the quality factor, of these waves can help to understand the damping mechanism (Ofman and Aschwanden 2002; Aschwanden *et al.* 2003). It also gives an idea about the relative strength of the damping. Although a quality factor greater than 0.5 signifies damping, statistical observational studies have reported that it varies from 0.6 to 5.4 (Verwichte *et al.* (2013) and references therein). In our observation, the quality factor varies from 1.6 to 3.5, which means that our observed damping oscillations lie in the under-damped regime. Hence, it could be an energy source for heating. Because only limited data were available, we were unable to detect damping at several locations. To detect damping of shorter periodicities, very high cadence observations are required.

We also tried to characterize the nature of the wave modes. The oscillations in intensity and velocity can be interpreted as due to compressional waves, whereas oscillations with a shared period in intensity and FWHM can be due to the propagation of the fast sausage mode. The Doppler velocity and FWHM oscillations can be associated with torsional Alfvén mode, whereas the existence of a Doppler velocity oscillation alone can be attributed to the fast kink mode (see Nakariakov and Verwichte (2005); Aschwanden (2006)).

One may also interpret the correlated oscillations between intensity, Doppler velocity, and line width as shown in Figure 7.15 as due to quasi-periodic flows (De Pontieu and McIntosh 2010; Tian *et al.* 2011a, 2012). Close to the streamer boundaries we do see such coherent oscillations and the scenario that flows are present cannot be ruled out, although numerical simulation of Verwichte *et al.* (2010) demonstrated that due to the in-phase behaviour of velocity and density perturbations, upward propagating waves can cause similar effects.

If the selected locations correspond to several wave guides supporting different wave modes, it may not be possible to isolate and identify them. Thus it is not surprising that we see different signatures at different locations. Statistically speaking, the key questions are (i) which the significant modes are and (ii) what role they play in coronal heating.

# Chapter 8

# Concluding remarks

The solar atmosphere is made up of hot plasma where many complex structures are formed in the presence of the magnetic fields. A wide range of these magnetic structures in the solar atmosphere is being observed with several modern space and ground-based instruments. Most of the observed atmospheric structures are generally associated with the magnetic flux at the photosphere. Observations of the different atmospheric layers including magnetogram at the photosphere show the connection of the coronal and chromospheric structures with the photospheric magnetic fields. It is now believed that the solar atmospheric structures are magnetically coupled from the photosphere through the chromosphere, transition region (TR) up to the upper atmosphere, the corona. The atmosphere is also very inhomogeneous at different spatial scales and highly dynamic over a long timescale. The dynamical interaction of magnetic fields sometimes produces the large-scale event, e.g., flares, filaments events, CMEs whereas, at the same time very small-scale events, e.g., small-scale jets, sudden brightenings, high-frequency waves also take place within these structures. The large-scale structures are being studied for a longer time, and it is understood that they are coupled throughout the solar atmosphere, particularly, the link of the photospheric connection to the structure formation in the chromosphere/corona are well established. But, the spatial and temporal resolution was always a limitation to studying the small-scale events or high-frequency dynamics. With the advancement of new instruments with increasing spatial, temporal and spectral resolutions, are shedding light into our understanding of these very small-scale events and their dynamics. At the same time, these new results puzzling us with more and more new problems. The main aim of this thesis was to understand/improve our knowledge on a few such issues using imaging and spectroscopic data from instruments both ground- and space-based. High-cadence multi-wavelength observations allowed us to study dynamics inside the large structure, e.g. coronal bright points, plumes, etc. and their association/coupling different layers throughout the solar atmosphere. Significant results presented in the thesis is summarized below along with their future directions.

## 8.1 Major Results & Future Directions

At the beginning of the thesis, we tried to understand the interaction of the waves with the magnetic fields in the lower solar atmosphere. Powermaps of the upper photosphere and the lower chromosphere show two distinct features: i) magnetic shadows: region of suppressed power surrounding the magnetic network elements in the chromosphere and ii) power halos: region of enhanced power close to the photosphere. The interaction between acoustic waves and inclined magnetic fields is generally believed to be responsible for these two effects. It was also believed that highly inclined magnetic fields significantly increase the cut-off period and create magneto-acoustic portals for the propagation of long-period waves in the chromosphere. This is commonly referred to as leakage of photospheric oscillations into the chromosphere. With our recent high-resolution and high-cadence data and the subsequent analysis, we have proposed an alternative scenario. The high cadence is the key to the understanding of the dynamics. With the new high-resolution data and high-cadence data, we just begin to see highly dynamic transients like Rapid Blueshifted Excursions (RBEs) and Rapid Redshifted Excursions (RREs) prominently. The high-cadence (1.34 s) observation enabled us to identify and study their dynamics which was not possible earlier with lower cadence (Using DOT H-alpha observations with a cadence of 30 s, (Kontogiannis *et al.* 2010b)). In this study, we explored whether small-scale transients can influence the distribution of power at different heights. We show that the presence of transients, like mottles, RBEs, and RREs, can strongly influence the powermaps. The short and finite lifetime of these events strongly affects all powermaps, potentially influencing the observed power distribution. We show that Doppler-shifted transients like RBEs and RREs that occur ubiquitously can have a dominant effect on the formation of the power halos in the quiet-Sun. For magnetic shadows around the 3-minute band, the mode conversion seems to be most effective, whereas the power at longer periods is highly influenced by the presence of mottles. Our methodology and presentation showed that this subject of power halos in the photosphere and the observed long-period in the chromosphere could be interpreted in an alternative way and all previous studies might have provided an incomplete description of the energy propagation and distribution in the chromosphere. Thus these new results open up an entirely new alternative approach how we treat the chromospheric dynamics. The high-cadence observations reveal that flows, waves, and shocks manifest in the presence of magnetic fields to form a nonlinear magnetohydrodynamic system. The transverse oscillations in the mottles in a rosette may also play a role in enhancing or reducing the power in the powermaps which remain to be explored. The real source of chromospheric power distribution is dependent on different wave modes and transients which need to be quantified. The present study used mostly imaging and limited spectral data. We propose to perform simultaneous imaging and spectral observations of the chromosphere with sufficient high cadence to shed more light into the dynamics.

Quasi-periodic brightenings are frequently observed within coronal bright points (BPs). Some researcher thought that these oscillations are caused by the leakage of $p$-modes, which propagate along the magnetic flux tubes whereas others believed that oscillations are due to repeated magnetic reconnections. We studied the dynamics of a BP seen in a coronal hole using the Atmospheric Imaging Assembly (AIA) images, the Helioseismic and Magnetic Imager (HMI) magnetogram, and spectroscopic data from the Interface Region Imaging Spectrograph (IRIS). With the highest possible spectral and spatial resolution of IRIS, we attempted to identify the sources of these oscillations. We recorded enhanced line profile asymmetry, enhanced line width, intensity enhancements, and large Doppler shift in the IRIS Si IV line profiles at specific instances at the foot point of a BP. We proposed that transition region explosive events originating from small-scale reconnections and the reconnection outflows are affecting the line profiles. We showed that these EEs are closely related to the brightening in BPs and magnetic flux cancellation. The correlation between all these parameters is consistent with the repetitive reconnection scenario and could explain the quasi-periodic nature of the brightening. The contribution of waves if any and/or repeated reconnection in controlling the oscillations in the BPs, need to be quantified in future work.

Propagating intensity Disturbances (PDs) which are often observed in coronal open structures. The nature of these PDs is still not yet fully understood, whether the waves or flows could be responsible for the observed PDs. We observed PDs in the polar off-limb region coronal plumes. From the IRIS and AIA imaging observations, we tried to explore the sources of these coronal PDs as well as the nature of these PDs. We showed that the spicules and the PDs originate through a common process (probably reconnections or $p$-modes). These findings provide a new explanation for the source of coronal PDs and deserve a further in-depth study. The work related to PDs and their sources can be extended using IRIS spectroscopic observations to find statistically if Type I or Type II spicules are equally responsible for generating the PDs.

Fine-scale dynamics and their coupling in the strong magnetic concentrated regions above sunspots are being studied with a greater interest in the recent decades. With the launch of the IRIS observations, a new feature known as the Bright Dots (BDs) is reported recently. They are subarcsecond in size and appear ubiquitously in the transition region above sunspot penumbra. The presence of Penumbral Micro-Jets (PMJs) in the chromosphere are also reported earlier. Using simultaneous observations of the chromosphere from the Solar Optical Telescope (SOT) and the transition region from the IRIS we studied the dynamics of the BDs and their relation with the PMJs. We performed statistical analysis and reported two types of BDs, one which is related to PMJs and others which are not and have different properties. The BDs which are related to PMJs always appear at the top of the PMJs, the vast majority of which show inward motion and originate before the generation of the PMJs. These results may indicate that the reconnection occurs at the lower coronal/TR height and initiates PMJs at the chromosphere. This formation mechanism is in contrast to the earlier believed formation of PMJs by reconnection in the (upper) photosphere between differently inclined fields. We proposed a new scenario to explain this puzzling behavior. A subsequent extensive study can be made using spectroscopy to understand this fine-scale coupling entirely.

Our multi-slit spectroscopic observation of coronal spectral lines conducted during a total solar eclipse shed new lights in the understanding of the high-frequency waves phenomena. We studied the high-frequency oscillation using wavelet analysis and line width variations in large coronal loops. We characterized the nature of the observed oscillations. For the first time, we detected the damping of these high-frequency oscillations (periods $\sim$10 s), which may play a significant role in coronal heating as predicted long back. This work can be extended with better quality data to estimate the energy loss due to damping and to evaluate how significant they are for coronal heating. This type of high-cadence coronal data are available during a short period of time during total solar eclipses. Thus only very limited data is available for such analysis. In future, the Visible Emission Line Coronagraph on board Indian ADITYA-L1 mission will have capabilities of observing coronal emissions at very high spatial and temporal resolutions. Thus, the high-frequency oscillations in the higher coronal structures can be observed with these instruments.

# Bibliography

Alissandrakis, C. E., 1981, "On the computation of constant alpha force-free magnetic field", *Astron. Astrophys.*, **100**, 197–200. [ADS]

Alpert, S. E., Tiwari, S. K., Moore, R. L., Winebarger, A. R. and Savage, S. L., 2016, "Hi-C Observations of Sunspot Penumbral Bright Dots", *Astrophys. J.*, **822**, 35. [DOI], [ADS], [arXiv:1603.04968 [astro-ph.SR]]

Aschwanden, M. J., 1987, "Theory of radio pulsations in coronal loops", *Solar Phys.*, **111**, 113–136. [DOI], [ADS]

Aschwanden, M. J., 2006, "Coronal magnetohydrodynamic waves and oscillations: observations and quests", *Roy. Soc. London Phil. Trans. Ser. A*, **364**, 417–432. [DOI], [ADS]

Aschwanden, M. J., Fletcher, L., Schrijver, C. J. and Alexander, D., 1999, "Coronal Loop Oscillations Observed with the Transition Region and Coronal Explorer", *Astrophys. J.*, **520**, 880–894. [DOI], [ADS]

Aschwanden, M. J., Nightingale, R. W., Andries, J., Goossens, M. and Van Doorsselaere, T., 2003, "Observational Tests of Damping by Resonant Absorption in Coronal Loop Oscillations", *Astrophys. J.*, **598**, 1375–1386. [DOI], [ADS], [astro-ph/0309470]

Bai, X. Y., Su, J. T., Cao, W. D., Liu, S. Q., Deng, Y. Y. and Priya, T. G., 2016, "Multi-wavelength Observations of a Subarcsecond Penumbral Transient Brightening Event", *Astrophys. J.*, **823**, 60. [DOI], [ADS]

Banerjee, D. and Krishna Prasad, S., 2015, "MHD Waves in the coronal holes", *ArXiv e-prints*. [ADS], [arXiv:1505.04475 [astro-ph.SR]]

Banerjee, D., O'Shea, E. and Doyle, J. G., 2000, "Long-Period Oscillations in Polar Plumes as Observed by cds on Soho", *Solar Phys.*, **196**, 63–78. [ADS]

Banerjee, D., Erdélyi, R., Oliver, R. and O'Shea, E., 2007, "Present and Future Observing Trends in Atmospheric Magnetoseismology", *Solar Phys.*, **246**, 3–29. [DOI], [ADS]

Banerjee, D., Teriaca, L., Gupta, G. R., Imada, S., Stenborg, G. and Solanki, S. K., 2009, "Propagating waves in polar coronal holes as seen by SUMER & EIS", *Astron. Astrophys.*, **499**, L29–L32. [DOI], [ADS], [arXiv:0905.1013 [astro-ph.SR]]

Banerjee, D., Gupta, G. R. and Teriaca, L., 2011, "Propagating MHD Waves in Coronal Holes", *Space Sci. Rev.*, **158**, 267–288. [DOI], [ADS], [arXiv:1009.2980 [astro-ph.SR]]

Bellot Rubio, L. R., Balthasar, H. and Collados, M., 2004, "Two magnetic components in sunspot penumbrae", *Astron. Astrophys.*, **427**, 319–334. [DOI], [ADS]

Billings, D. E., 1959, "Velocity Fields in a Coronal Region with a Possible Hydromagnetic Interpretation.", *Astrophys. J.*, **130**, 215. [DOI], [ADS]

Bocchialini, K., Vial, J.-C. and Koutchmy, S., 1994, "Dynamical properties of the chromosphere in and out of the solar magnetic network", *Astrophys. J. Lett.*, **423**, L67–L70. [DOI], [ADS]

Boerner, P., Edwards, C., Lemen, J., Rausch, A., Schrijver, C., Shine, R., Shing, L., Stern, R., Tarbell, T., Title, A., Wolfson, C. J., Soufli, R., Spiller, E., Gullikson, E., McKenzie, D., Windt, D., Golub, L., Podgorski, W., Testa, P. and Weber, M., 2012, "Initial Calibration of the Atmospheric Imaging Assembly (AIA) on the Solar Dynamics Observatory (SDO)", *Solar Phys.*, **275**, 41–66. [DOI], [ADS]

Bogdan, T. J., Carlsson, M., Hansteen, V. H., McMurry, A., Rosenthal, C. S., Johnson, M., Petty-Powell, S., Zita, E. J., Stein, R. F., McIntosh, S. W. and Nordlund, Å., 2003, "Waves in the Magnetized Solar Atmosphere. II. Waves from Localized Sources in Magnetic Flux Concentrations", *Astrophys. J.*, **599**, 626–660. [DOI], [ADS]

Bostancı, Z. F., Gültekin, A. and Al, N., 2014, "Oscillatory behaviour of chromospheric fine structures in a network and a semi-active region", *Mon. Not. Roy. Astron. Soc.*, **443**, 1267–1273. [DOI], [ADS], [arXiv:1406.4507 [astro-ph.SR]]

Brueckner, G. E. and Bartoe, J.-D. F., 1983, "Observations of high-energy jets in the corona above the quiet sun, the heating of the corona, and the acceleration of the solar wind", *Astrophys. J.*, **272**, 329–348. [DOI], [ADS]

Carlsson, M. and Bogdan, T. J., 2006, "Numerical modelling of MHD waves in the solar chromosphere", *Royal Society of London Philosophical Transactions Series A*, **364**, 395–404. [DOI], [ADS]

Carlsson, M. and Stein, R. F., 1992, "Non-LTE radiating acoustic shocks and CA II K2V bright points", *Astrophys. J. Lett.*, **397**, L59–L62. [DOI], [ADS]

Carlsson, M. and Stein, R. F., 1997, "Formation of Solar Calcium H and K Bright Grains", *Astrophys. J.*, **481**, 500–514. [ADS]

Cauzzi, G., Falchi, A. and Falciani, R., 2000, "Network and internetwork: a compared multiwavelength analysis", *Astron. Astrophys.*, **357**, 1093–1104. [ADS], [astro-ph/0004082]

Centeno, R., Collados, M. and Trujillo Bueno, J., 2006, "Spectropolarimetric Investigation of the Propagation of Magnetoacoustic Waves and Shock Formation in Sunspot Atmospheres", *Astrophys. J.*, **640**, 1153–1162. [DOI], [ADS], [astro-ph/0512096]

Chae, J., Wang, H., Lee, C.-Y., Goode, P. R. and Schühle, U., 1998, “Photospheric Magnetic Field Changes Associated with Transition Region Explosive Events”, *Astrophys. J. Lett.*, **497**, L109–L112. [DOI], [ADS]

Chandrashekhar, K., Krishna Prasad, S., Banerjee, D., Ravindra, B. and Seaton, D. B., 2013, “Dynamics of Coronal Bright Points as Seen by Sun Watcher Using Active Pixel System Detector and Image Processing (SWAP), Atmospheric Imaging Assembly (AIA), and Helioseismic and Magnetic Imager (HMI)”, *Solar Phys.*, **286**, 125–142. [DOI], [ADS], [arXiv:1206.0095 [astro-ph.SR]]

Chitta, L. P., Peter, H. and Young, P. R., 2016, “A closer look at a coronal loop rooted in a sunspot umbra”, *Astron. Astrophys.*, **587**, A20. [DOI], [ADS], [arXiv:1512.03831 [astro-ph.SR]]

Christopoulou, E. B., Georgakilas, A. A. and Koutchmy, S., 2001, “Fine Structure of the Magnetic Chromosphere: Near-Limb Imaging, Data Processing and Analysis of Spicules and Mottles”, *Solar Phys.*, **199**, 61–80. [DOI], [ADS]

Cooper, F. C., Nakariakov, V. M. and Williams, D. R., 2003, “Short period fast waves in solar coronal loops”, *Astron. Astrophys.*, **409**, 325–330. [DOI], [ADS]

Cowsik, R., Singh, J., Saxena, A. K., Srinivasan, R. and Raveendran, A. V., 1999, “Short-period intensity oscillations in the solar corona observed during the total solar eclipse of 26 February 1998”, *Solar Phys.*, **188**, 89–98. [ADS]

Dame, L., Gouttebroze, P. and Malherbe, J.-M., 1984, “Observation and analysis of intensity oscillations in the solar K-line”, *Astron. Astrophys.*, **130**, 331–340. [ADS]

de la Cruz Rodríguez, J., Löfdahl, M. G., Sütterlin, P., Hillberg, T. and Rouppe van der Voort, L., 2015, “CRISPRED: A data pipeline for the CRISP imaging spectropolarimeter”, *Astron. Astrophys.*, **573**, A40. [DOI], [ADS], [arXiv:1406.0202 [astro-ph.SR]]

De Moortel, I. and Nakariakov, V. M., 2012, "Magnetohydrodynamic waves and coronal seismology: an overview of recent results", *Royal Society of London Philosophical Transactions Series A*, **370**, 3193–3216. [DOI], [ADS], [arXiv:1202.1944 [astro-ph.SR]]

De Moortel, I. and Pascoe, D. J., 2012, "The Effects of Line-of-sight Integration on Multistrand Coronal Loop Oscillations", *Astrophys. J.*, **746**, 31. [DOI], [ADS]

De Pontieu, B. and McIntosh, S. W., 2010, "Quasi-periodic Propagating Signals in the Solar Corona: The Signature of Magnetoacoustic Waves or High-velocity Upflows?", *Astrophys. J.*, **722**, 1013–1029. [DOI], [ADS], [arXiv:1008.5300 [astro-ph.SR]]

De Pontieu, B., Erdélyi, R. and James, S. P., 2004, "Solar chromospheric spicules from the leakage of photospheric oscillations and flows", *Nature*, **430**, 536–539. [DOI], [ADS]

De Pontieu, B., Hansteen, V. H., Rouppe van der Voort, L., van Noort, M. and Carlsson, M., 2007, "High-Resolution Observations and Numerical Simulations of Chromospheric Fibrils and Mottles", in *The Physics of Chromospheric Plasmas*, (Eds.) Heinzel, P., Dorotovič, I., Rutten, R. J., Astronomical Society of the Pacific Conference Series, 368, [ADS]

De Pontieu, B., McIntosh, S. W., Hansteen, V. H. and Schrijver, C. J., 2009, "Observing the Roots of Solar Coronal Heating–in the Chromosphere", *Astrophys. J. Lett.*, **701**, L1–L6. [DOI], [ADS], [arXiv:0906.5434 [astro-ph.SR]]

De Pontieu, B., McIntosh, S. W., Carlsson, M., Hansteen, V. H., Tarbell, T. D., Boerner, P., Martinez-Sykora, J., Schrijver, C. J. and Title, A. M., 2011, "The Origins of Hot Plasma in the Solar Corona", *Science*, **331**, 55–. [DOI], [ADS]

De Pontieu, B., Title, A. M., Lemen, J. R., Kushner, G. D., Akin, D. J., Allard, B., Berger, T., Boerner, P., Cheung, M., Chou, C., Drake, J. F., Duncan, D. W., Freeland, S., Heyman, G. F., Hoffman, C., Hurlburt, N. E., Lindgren,

R. W., Mathur, D., Rehse, R., Sabolish, D., Seguin, R., Schrijver, C. J., Tarbell, T. D., Wülser, J.-P., Wolfson, C. J., Yanari, C., Mudge, J., Nguyen-Phuc, N., Timmons, R., van Bezooijen, R., Weingrod, I., Brookner, R., Butcher, G., Dougherty, B., Eder, J., Knagenhjelm, V., Larsen, S., Mansir, D., Phan, L., Boyle, P., Cheimets, P. N., DeLuca, E. E., Golub, L., Gates, R., Hertz, E., McKillop, S., Park, S., Perry, T., Podgorski, W. A., Reeves, K., Saar, S., Testa, P., Tian, H., Weber, M., Dunn, C., Eccles, S., Jaeggli, S. A., Kankelborg, C. C., Mashburn, K., Pust, N., Springer, L., Carvalho, R., Kleint, L., Marmie, J., Mazmanian, E., Pereira, T. M. D., Sawyer, S., Strong, J., Worden, S. P., Carlsson, M., Hansteen, V. H., Leenaarts, J., Wiesmann, M., Aloise, J., Chu, K.-C., Bush, R. I., Scherrer, P. H., Brekke, P., Martinez-Sykora, J., Lites, B. W., McIntosh, S. W., Uitenbroek, H., Okamoto, T. J., Gummin, M. A., Auker, G., Jerram, P., Pool, P. and Waltham, N., 2014, “The Interface Region Imaging Spectrograph (IRIS)”, *Solar Phys.*, **289**, 2733–2779. [DOI], [ADS], [arXiv:1401.2491 [astro-ph.SR]]

Deforest, C. E. and Gurman, J. B., 1998, “Observation of Quasi-periodic Compressive Waves in Solar Polar Plumes”, *Astrophys. J. Lett.*, **501**, L217. [DOI], [ADS]

Deforest, C. E., Hoeksema, J. T., Gurman, J. B., Thompson, B. J., Plunkett, S. P., Howard, R., Harrison, R. C. and Hassler, D. M., 1997, “Polar Plume Anatomy: Results of a Coordinated Observation”, *Solar Phys.*, **175**, 393–410. [DOI], [ADS]

Deng, N., Yurchyshyn, V., Tian, H., Kleint, L., Liu, C., Xu, Y. and Wang, H., 2016, “Multi-wavelength Study of Transition Region Penumbral Subarcsecond Bright Dots Using IRIS and NST”, *Astrophys. J.*, **829**, 103. [DOI], [ADS], [arXiv:1607.00306 [astro-ph.SR]]

Dere, K. P., Bartoe, J.-D. F., Brueckner, G. E. and Recely, F., 1989, “Transition zone flows observed in a coronal hole on the solar disk”, *Astrophys. J. Lett.*, **345**, L95–L97. [DOI], [ADS]

Deubner, F.-L. and Fleck, B., 1990, “Dynamics of the solar atmosphere. III - Cell-network distinctions of chromospheric oscillations”, *Astron. Astrophys.*, **228**, 506–512. [ADS]

Doyle, J. G., Popescu, M. D. and Taroyan, Y., 2006, “Repetitive occurrence of explosive events at a coronal hole boundary”, *Astron. Astrophys.*, **446**, 327–331. [DOI], [ADS]

Golub, L., Krieger, A. S., Silk, J. K., Timothy, A. F. and Vaiana, G. S., 1974, “Solar X-Ray Bright Points”, *Astrophys. J. Lett.*, **189**, L93+. [ADS]

Golub, L., Krieger, A. S. and Vaiana, G. S., 1976a, “Distribution of lifetimes for coronal soft X-ray bright points”, *Solar Phys.*, **49**, 79–90. [DOI], [ADS]

Golub, L., Krieger, A. S. and Vaiana, G. S., 1976b, “Observation of spatial and temporal variations in X-ray bright point emergence patterns”, *Solar Phys.*, **50**, 311–327. [DOI], [ADS]

Goossens, M., Andries, J. and Aschwanden, M. J., 2002, “Coronal loop oscillations. An interpretation in terms of resonant absorption of quasi-mode kink oscillations”, *Astron. Astrophys.*, **394**, L39–L42. [DOI], [ADS]

Gupta, G. R., 2014, “Observations of dissipation of slow magneto-acoustic waves in a polar coronal hole”, *Astron. Astrophys.*, **568**, A96. [DOI], [ADS], [arXiv:1407.1017 [astro-ph.SR]]

Gupta, G. R., Teriaca, L., Marsch, E., Solanki, S. K. and Banerjee, D., 2012, “Spectroscopic observations of propagating disturbances in a polar coronal hole: evidence of slow magneto-acoustic waves”, *Astron. Astrophys.*, **546**, A93. [DOI], [ADS], [arXiv:1209.3524 [astro-ph.SR]]

Gupta, G. R., Subramanian, S., Banerjee, D., Madjarska, M. S. and Doyle, J. G., 2013, “Nature of Quiet Sun Oscillations Using Data from the Hinode, TRACE, and SOHO Spacecraft”, *Solar Phys.*, **282**, 67–86. [DOI], [ADS], [arXiv:1209.5252 [astro-ph.SR]]

Habbal, S. R. and Withbroe, G. L., 1981, “Spatial and temporal variations of EUV coronal bright points”, *Solar Phys.*, **69**, 77–97. [ADS]

Habbal, S. R., Druckmüller, M., Morgan, H., Ding, A., Johnson, J., Druckmüllerová, H., Daw, A., Arndt, M. B., Dietzel, M. and Saken, J., 2011, “Thermodynamics of the Solar Corona and Evolution of the Solar Magnetic Field as Inferred from the Total Solar Eclipse Observations of 2010 July 11”, *Astrophys. J.*, **734**, 120. [DOI], [ADS]

Handy, B. N. and Schrijver, C. J., 2001, “On the Evolution of the Solar Photospheric and Coronal Magnetic Field”, *Astrophys. J.*, **547**, 1100–1108. [DOI], [ADS]

Heggland, L., Hansteen, V. H., De Pontieu, B. and Carlsson, M., 2011, “Wave Propagation and Jet Formation in the Chromosphere”, *Astrophys. J.*, **743**, 142. [DOI], [ADS], [arXiv:1112.0037 [astro-ph.SR]]

Henriques, V. M. J., 2012, “Three-dimensional temperature mapping of solar photospheric fine structure using Ca ii H filtergrams”, *Astron. Astrophys.*, **548**, A114. [DOI], [ADS], [arXiv:1210.4168 [astro-ph.SR]]

Henriques, V. M. J. and Kiselman, D., 2013, “Ca II H sunspot tomography from the photosphere to the chromosphere”, *Astron. Astrophys.*, **557**, A5. [DOI], [ADS]

Henriques, V. M. J., Kuridze, D., Mathioudakis, M. and Keenan, F. P., 2016, “Quiet Sun H\alpha\ Transients and Corresponding Small-Scale Transition Region and Coronal Heating”, *ArXiv e-prints*. [ADS], [arXiv:1602.04820 [astro-ph.SR]]

Huang, Z., Madjarska, M. S., Xia, L., Doyle, J. G., Galsgaard, K. and Fu, H., 2014, “Explosive Events on a Subarcsecond Scale in IRIS Observations: A Case Study”, *Astrophys. J.*, **797**, 88. [DOI], [ADS], [arXiv:1409.6425 [astro-ph.SR]]

Innes, D. E., Inhester, B., Axford, W. I. and Wilhelm, K., 1997, “Bi-directional plasma jets produced by magnetic reconnection on the Sun”, *Nature*, **386**, 811–813. [DOI], [ADS]

Jefferies, S. M., McIntosh, S. W., Armstrong, J. D., Bogdan, T. J., Cacciani, A. and Fleck, B., 2006, “Magnetoacoustic Portals and the Basal Heating of the Solar Chromosphere”, *Astrophys. J. Lett.*, **648**, L151–L155. [DOI], [ADS]

Jess, D. B., Mathioudakis, M., Christian, D. J., Crockett, P. J. and Keenan, F. P., 2010, “A Study of Magnetic Bright Points in the Na I $D_1$ Line”, *Astrophys. J. Lett.*, **719**, L134–L139. [DOI], [ADS], [arXiv:1007.2515 [astro-ph.SR]]

Jess, D. B., Reznikova, V. E., Van Doorsselaere, T., Keys, P. H. and Mackay, D. H., 2013, “The Influence of the Magnetic Field on Running Penumbral Waves in the Solar Chromosphere”, *Astrophys. J.*, **779**, 168. [DOI], [ADS], [arXiv:1310.7939 [astro-ph.SR]]

Jess, D. B., Morton, R. J., Verth, G., Fedun, V., Grant, S. D. T. and Giagkiozis, I., 2015, “Multiwavelength Studies of MHD Waves in the Solar Chromosphere. An Overview of Recent Results”, *Space Sci. Rev.*, **190**, 103–161. [DOI], [ADS], [arXiv:1503.01769 [astro-ph.SR]]

Jiang, R.-L., Fang, C. and Chen, P.-F., 2012, “Numerical Simulation of Solar Microflares in a Canopy-type Magnetic Configuration”, *Astrophys. J.*, **751**, 152. [DOI], [ADS], [arXiv:1204.5847 [astro-ph.SR]]

Jiao, F., Xia, L., Li, B., Huang, Z., Li, X., Chandrashekhar, K., Mou, C. and Fu, H., 2015, “Sources of Quasi-periodic Propagating Disturbances above a Solar Polar Coronal Hole”, *Astrophys. J. Lett.*, **809**, L17. [DOI], [ADS], [arXiv:1507.08440 [astro-ph.SR]]

Judge, P. G., Tarbell, T. D. and Wilhelm, K., 2001, “A Study of Chromospheric Oscillations Using the SOHO and TRACE Spacecraft”, *Astrophys. J.*, **554**, 424–444. [DOI], [ADS]

Kariyappa, R., Deluca, E. E., Saar, S. H., Golub, L., Damé, L., Pevtsov, A. A. and Varghese, B. A., 2011, "Temperature variability in X-ray bright points observed with Hinode/XRT", *Astron. Astrophys.*, **526**, A78. [DOI], [ADS]

Katsiyannis, A. C., Williams, D. R., McAteer, R. T. J., Gallagher, P. T., Keenan, F. P. and Murtagh, F., 2003, "Eclipse observations of high-frequency oscillations in active region coronal loops", *Astron. Astrophys.*, **406**, 709–714. [DOI], [ADS], [arXiv:astro-ph/0305225]

Katsukawa, Y., Berger, T. E., Ichimoto, K., Lites, B. W., Nagata, S., Shimizu, T., Shine, R. A., Suematsu, Y., Tarbell, T. D., Title, A. M. and Tsuneta, S., 2007, "Small-Scale Jetlike Features in Penumbral Chromospheres", *Science*, **318**, 1594. [DOI], [ADS]

Khomenko, E. and Collados, M., 2006, "Numerical Modeling of Magnetohydrodynamic Wave Propagation and Refraction in Sunspots", *Astrophys. J.*, **653**, 739–755. [DOI], [ADS]

Khomenko, E., Centeno, R., Collados, M. and Trujillo Bueno, J., 2008, "Channeling 5 Minute Photospheric Oscillations into the Solar Outer Atmosphere through Small-Scale Vertical Magnetic Flux Tubes", *Astrophys. J. Lett.*, **676**, L85–L88. [DOI], [ADS], [arXiv:0802.0938]

Kitagawa, N., Yokoyama, T., Imada, S. and Hara, H., 2010, "Mode Identification of MHD Waves in an Active Region Observed with Hinode/EIS", *Astrophys. J.*, **721**, 744–749. [DOI], [ADS], [arXiv:1008.1823 [astro-ph.SR]]

Kleint, L., Antolin, P., Tian, H., Judge, P., Testa, P., De Pontieu, B., Martínez-Sykora, J., Reeves, K. K., Wuelser, J. P., McKillop, S., Saar, S., Carlsson, M., Boerner, P., Hurlburt, N., Lemen, J., Tarbell, T. D., Title, A., Golub, L., Hansteen, V., Jaeggli, S. and Kankelborg, C., 2014, "Detection of Supersonic Downflows and Associated Heating Events in the Transition Region above Sunspots", *Astrophys. J. Lett.*, **789**, L42. [DOI], [ADS], [arXiv:1406.6816 [astro-ph.SR]]

Klimchuk, J. A., 2006, “On Solving the Coronal Heating Problem”, *Solar Phys.*, **234**, 41–77. [DOI], [ADS], [arXiv:astro-ph/0511841]

Kontogiannis, I., Tsiropoula, G. and Tziotziou, K., 2010a, “Power halo and magnetic shadow in a solar quiet region observed in the H$\alpha$ line”, *Astron. Astrophys.*, **510**, A41. [DOI], [ADS]

Kontogiannis, I., Tsiropoula, G., Tziotziou, K. and Georgoulis, M. K., 2010b, “Oscillations in a network region observed in the H$\alpha$ line and their relation to the magnetic field”, *Astron. Astrophys.*, **524**, A12. [DOI], [ADS]

Kontogiannis, I., Tsiropoula, G. and Tziotziou, K., 2014, “Transmission and conversion of magnetoacoustic waves on the magnetic canopy in a quiet Sun region”, *Astron. Astrophys.*, **567**, A62. [DOI], [ADS], [arXiv:1406.5066 [astro-ph.SR]]

Kosugi, T., Matsuzaki, K., Sakao, T., Shimizu, T., Sone, Y., Tachikawa, S., Hashimoto, T., Minesugi, K., Ohnishi, A., Yamada, T., Tsuneta, S., Hara, H., Ichimoto, K., Suematsu, Y., Shimojo, M., Watanabe, T., Shimada, S., Davis, J. M., Hill, L. D., Owens, J. K., Title, A. M., Culhane, J. L., Harra, L. K., Doschek, G. A. and Golub, L., 2007, “The Hinode (Solar-B) Mission: An Overview”, *Solar Phys.*, **243**, 3–17. [DOI], [ADS]

Koutchmy, S., Zhugzhda, I. D. and Locans, V., 1983, “Short period coronal oscillations - Observation and interpretation”, *Astron. Astrophys.*, **120**, 185–191. [ADS]

Krijger, J. M., Rutten, R. J., Lites, B. W., Straus, T., Shine, R. A. and Tarbell, T. D., 2001, “Dynamics of the solar chromosphere. III. Ultraviolet brightness oscillations from TRACE”, *Astron. Astrophys.*, **379**, 1052–1082. [DOI], [ADS]

Krishna Prasad, S., Banerjee, D. and Gupta, G. R., 2011, “Propagating intensity disturbances in polar corona as seen from AIA/SDO”, *Astron. Astrophys.*, **528**, L4. [DOI], [ADS], [arXiv:1102.2979 [astro-ph.SR]]

Kumar, M., Srivastava, A. K. and Dwivedi, B. N., 2011, "Observation of intensity oscillations above X-ray bright points from the Hinode/XRT: signature of magnetohydrodynamic oscillations in the solar corona", *Mon. Not. Roy. Astron. Soc.*, **415**, 1419–1425. [DOI], [ADS]

Kuridze, D., Zaqarashvili, T. V., Shergelashvili, B. M. and Poedts, S., 2008, "Acoustic oscillations in a field-free cavity under solar small-scale bipolar magnetic canopy", *Annales Geophysicae*, **26**, 2983–2989. [DOI], [ADS], [arXiv:0801.2877]

Kuridze, D., Henriques, V., Mathioudakis, M., Erdélyi, R., Zaqarashvili, T. V., Shelyag, S., Keys, P. H. and Keenan, F. P., 2015, "The Dynamics of Rapid Redshifted and Blueshifted Excursions in the Solar H$\alpha$ Line", *Astrophys. J.*, **802**, 26. [DOI], [ADS], [arXiv:1501.06205 [astro-ph.SR]]

Laing, G. B. and Edwin, P. M., 1995a, "Dissipating waves in a hot, compressible, magnetic, structured atmosphere", *Solar Phys.*, **157**, 103–119. [DOI], [ADS]

Laing, G. B. and Edwin, P. M., 1995b, "Dissipating the Energy of Magnetoacoustic Waves in a Structured Atmosphere", *Solar Phys.*, **161**, 269–287. [DOI], [ADS]

Langangen, Ø., De Pontieu, B., Carlsson, M., Hansteen, V. H., Cauzzi, G. and Reardon, K., 2008, "Search for High Velocities in the Disk Counterpart of Type II Spicules", *Astrophys. J. Lett.*, **679**, L167–L170. [DOI], [ADS], [arXiv:0804.3256]

Leenaarts, J., Rutten, R. J., Sütterlin, P., Carlsson, M. and Uitenbroek, H., 2006, "DOT tomography of the solar atmosphere. VI. Magnetic elements as bright points in the blue wing of H$\alpha$", *Astron. Astrophys.*, **449**, 1209–1218. [DOI], [ADS]

Leenaarts, J., Carlsson, M. and Rouppe van der Voort, L., 2012, "The Formation of the H$\alpha$ Line in the Solar Chromosphere", *Astrophys. J.*, **749**, 136. [DOI], [ADS], [arXiv:1202.1926 [astro-ph.SR]]

Lemen, J. R., Title, A. M., Akin, D. J., Boerner, P. F., Chou, C., Drake, J. F., Duncan, D. W., Edwards, C. G., Friedlaender, F. M., Heyman, G. F., Hurlburt, N. E., Katz, N. L., Kushner, G. D., Levay, M., Lindgren, R. W., Mathur, D. P., McFeaters, E. L., Mitchell, S., Rehse, R. A., Schrijver, C. J., Springer, L. A., Stern, R. A., Tarbell, T. D., Wuelser, J.-P., Wolfson, C. J., Yanari, C., Bookbinder, J. A., Cheimets, P. N., Caldwell, D., Deluca, E. E., Gates, R., Golub, L., Park, S., Podgorski, W. A., Bush, R. I., Scherrer, P. H., Gummin, M. A., Smith, P., Auker, G., Jerram, P., Pool, P., Soufli, R., Windt, D. L., Beardsley, S., Clapp, M., Lang, J. and Waltham, N., 2012, "The Atmospheric Imaging Assembly (AIA) on the Solar Dynamics Observatory (SDO)", *Solar Phys.*, **275**, 17–40. [DOI], [ADS]

Li, D., Ning, Z. J. and Wang, J. F., 2013, "Statistical study of UV bright points and magnetic elements from SDO observations", *New Astronomy*, **23**, 19–26. [DOI], [ADS]

Lites, B. W., Elmore, D. F., Seagraves, P. and Skumanich, A. P., 1993, "Stokes Profile Analysis and Vector Magnetic Fields. VI. Fine Scale Structure of a Sunspot", *Astrophys. J.*, **418**, 928. [DOI], [ADS]

Löfdahl, M. G., 2002, "Multi-frame blind deconvolution with linear equality constraints", in *Society of Photo-Optical Instrumentation Engineers (SPIE) Conference Series*, (Ed.) P. J. Bones, M. A. Fiddy, & R. P. Millane, Presented at the Society of Photo-Optical Instrumentation Engineers (SPIE) Conference, 4792, [DOI], [ADS], [arXiv:physics/0209004]

Madjarska, M. S., Doyle, J. G., Teriaca, L. and Banerjee, D., 2003, "An EUV Bright Point as seen by SUMER, CDS, MDI and EIT on-board SoHO", *Astron. Astrophys.*, **398**, 775–784. [DOI], [ADS]

Mandal, S., Samanta, T., Banerjee, D., Krishna Prasad, S. and Teriaca, L., 2015, “Propagating disturbances along fan-like coronal loops in an active region”, *Research in Astronomy and Astrophysics*, **15**, 1832. [DOI], [ADS], [arXiv:1505.04710 [astro-ph.SR]]

Martínez-Sykora, J., De Pontieu, B., Hansteen, V. and McIntosh, S. W., 2011, “What do Spectral Line Profile Asymmetries Tell us About the Solar Atmosphere?”, *Astrophys. J.*, **732**, 84. [DOI], [ADS]

McIntosh, S. W., Fleck, B. and Judge, P. G., 2003, “Investigating the role of plasma topography on chromospheric oscillations observed by TRACE”, *Astron. Astrophys.*, **405**, 769–777. [DOI], [ADS]

McIntosh, S. W., Innes, D. E., de Pontieu, B. and Leamon, R. J., 2010, “STEREO observations of quasi-periodically driven high velocity outflows in polar plumes”, *Astron. Astrophys.*, **510**, L2. [DOI], [ADS], [arXiv:1001.3377 [astro-ph.SR]]

McIntosh, S. W., Wang, X., Leamon, R. J. and Scherrer, P. H., 2014, “Identifying Potential Markers of the Sun’s Giant Convective Scale”, *Astrophys. J. Lett.*, **784**, L32. [DOI], [ADS], [arXiv:1403.0692 [astro-ph.SR]]

Moretti, P. F., Jefferies, S. M., Armstrong, J. D. and McIntosh, S. W., 2007, “Observational signatures of the interaction between acoustic waves and the solar magnetic canopy”, *Astron. Astrophys.*, **471**, 961–965. [DOI], [ADS]

Morton, R. J. and McLaughlin, J. A., 2013, “Hi-C and AIA observations of transverse magnetohydrodynamic waves in active regions”, *Astron. Astrophys.*, **553**, L10. [DOI], [ADS], [arXiv:1305.0140 [astro-ph.SR]]

Nakagawa, Y. and Raadu, M. A., 1972, “On Practical Representation of Magnetic Field”, *Solar Phys.*, **25**, 127–135. [DOI], [ADS]

Nakariakov, V. M. and Roberts, B., 1995, “On Fast Magnetosonic Coronal Pulsations”, *Solar Phys.*, **159**, 399–402. [DOI], [ADS]

Nakariakov, V. M. and Verwichte, E., 2005, "Coronal Waves and Oscillations", *Living Reviews in Solar Physics*, **2**, 3–+. [ADS]

Nolte, J. T., Solodyna, C. V. and Gerassimenko, M., 1979, "Short-term temporal variations of X-ray bright points", *Solar Phys.*, **63**, 113–118. [DOI], [ADS]

Nordlund, Å., Stein, R. F. and Asplund, M., 2009, "Solar Surface Convection", *Living Reviews in Solar Physics*, **6**, 2. [DOI], [ADS]

Nutto, C., Steiner, O. and Roth, M., 2010, "Magneto-acoustic wave propagation and mode conversion in a magnetic solar atmosphere: Comparing results from the CO$^5$BOLD code with ray theory", *Astronomische Nachrichten*, **331**, 915. [DOI], [ADS], [arXiv:1009.5586 [astro-ph.SR]]

Nutto, C., Steiner, O. and Roth, M., 2012a, "Revealing the nature of magnetic shadows with numerical 3D-MHD simulations", *Astron. Astrophys.*, **542**, L30. [DOI], [ADS], [arXiv:1205.5308 [astro-ph.SR]]

Nutto, C., Steiner, O., Schaffenberger, W. and Roth, M., 2012b, "Modification of wave propagation and wave travel-time by the presence of magnetic fields in the solar network atmosphere", *Astron. Astrophys.*, **538**, A79. [DOI], [ADS]

Ofman, L. and Aschwanden, M. J., 2002, "Damping Time Scaling of Coronal Loop Oscillations Deduced from Transition Region and Coronal Explorer Observations", *Astrophys. J. Lett.*, **576**, L153–L156. [DOI], [ADS]

Ofman, L., Nakariakov, V. M. and Deforest, C. E., 1999, "Slow Magnetosonic Waves in Coronal Plumes", *Astrophys. J.*, **514**, 441–447. [DOI], [ADS]

Ofman, L., Nakariakov, V. M. and Sehgal, N., 2000, "Dissipation of Slow Magnetosonic Waves in Coronal Plumes", *Astrophys. J.*, **533**, 1071–1083. [DOI], [ADS]

O'Shea, E. and Doyle, J. G., 2009, "On oscillations found in an active region with EIS on Hinode", *Astron. Astrophys.*, **494**, 355–360. [DOI], [ADS]

O'Shea, E., Banerjee, D., Doyle, J. G., Fleck, B. and Murtagh, F., 2001, "Active region oscillations", *Astron. Astrophys.*, **368**, 1095–1107. [DOI], [ADS]

O'Shea, E., Banerjee, D. and Doyle, J. G., 2007, "A statistical study of wave propagation in coronal holes", *Astron. Astrophys.*, **463**, 713–725. [DOI], [ADS]

Pant, V., Dolla, L., Mazumder, R., Banerjee, D., Krishna Prasad, S. and Panditi, V., 2015, "Dynamics of On-disk Plumes as Observed with the Interface Region Imaging Spectrograph, the Atmospheric Imaging Assembly, and the Helioseismic and Magnetic Imager", *Astrophys. J.*, **807**, 71. [DOI], [ADS], [arXiv:1505.04473 [astro-ph.SR]]

Parnell, C. E., Priest, E. R. and Golub, L., 1994, "The three-dimensional structures of X-ray bright points", *Solar Phys.*, **151**, 57–74. [DOI], [ADS]

Pasachoff, J. M., Babcock, B. A., Russell, K. D. and Seaton, D. B., 2002, "Short-Period Waves That Heat the Corona Detected at the 1999 Eclipse", *Solar Phys.*, **207**, 241–257. [ADS], [arXiv:astro-ph/0202237]

Pereira, T. M. D., De Pontieu, B. and Carlsson, M., 2012, "Quantifying Spicules", *Astrophys. J.*, **759**, 18. [DOI], [ADS], [arXiv:1208.4404 [astro-ph.SR]]

Pereira, T. M. D., De Pontieu, B., Carlsson, M., Hansteen, V., Tarbell, T. D., Lemen, J., Title, A., Boerner, P., Hurlburt, N., Wülser, J. P., Martínez-Sykora, J., Kleint, L., Golub, L., McKillop, S., Reeves, K. K., Saar, S., Testa, P., Tian, H., Jaeggli, S. and Kankelborg, C., 2014, "An Interface Region Imaging Spectrograph First View on Solar Spicules", *Astrophys. J. Lett.*, **792**, L15. [DOI], [ADS], [arXiv:1407.6360 [astro-ph.SR]]

Pérez-Suárez, D., Maclean, R. C., Doyle, J. G. and Madjarska, M. S., 2008, "The structure and dynamics of a bright point as seen with Hinode, SoHO and TRACE", *Astron. Astrophys.*, **492**, 575–583. [DOI], [ADS], [arXiv:0810.1020]

Pesnell, W. D., Thompson, B. J. and Chamberlin, P. C., 2012, "The Solar Dynamics Observatory (SDO)", *Solar Phys.*, **275**, 3–15. [DOI], [ADS]

Phillips, K. J. H., Read, P. D., Gallagher, P. T., Keenan, F. P., Rudawy, P., Rompolt, B., Berlicki, A., Buczylko, A., Diego, F., Barnsley, R., Smartt, R. N., Pasachoff, J. M. and Babcock, B. A., 2000, "SECIS: The Solar Eclipse Coronal Eclipse Imaging System", *Solar Phys.*, **193**, 259–271. [ADS]

Porter, L. J., Klimchuk, J. A. and Sturrock, P. A., 1994a, "The possible role of MHD waves in heating the solar corona", *Astrophys. J.*, **435**, 482–501. [DOI], [ADS]

Porter, L. J., Klimchuk, J. A. and Sturrock, P. A., 1994b, "The possible role of high-frequency waves in heating solar coronal loops", *Astrophys. J.*, **435**, 502–514. [DOI], [ADS]

Preś , P. and Phillips, K. H. J., 1999, "The Magnetic Association of Coronal Bright Points", *Astrophys. J. Lett.*, **510**, L73–L76. [DOI], [ADS], [astro-ph/9810451]

Priest, E. R., Parnell, C. E. and Martin, S. F., 1994, "A converging flux model of an X-ray bright point and an associated canceling magnetic feature", *Astrophys. J.*, **427**, 459–474. [DOI], [ADS]

Pucci, S., Poletto, G., Sterling, A. C. and Romoli, M., 2014, "Birth, Life, and Death of a Solar Coronal Plume", *Astrophys. J.*, **793**, 86. [DOI], [ADS]

Rees, D. E. and Semel, M. D., 1979, "Line formation in an unresolved magnetic element - A test of the centre of gravity method", *Astron. Astrophys.*, **74**, 1–5. [ADS]

Rijs, C., Rajaguru, S. P., Przybylski, D., Moradi, H., Cally, P. S. and Shelyag, S., 2016, "3D Simulations of Realistic Power Halos in Magnetohydrostatic Sunspot Atmospheres: Linking Theory and Observation", *Astrophys. J.*, **817**, 45. [DOI], [ADS], [arXiv:1512.01297 [astro-ph.SR]]

Roberts, B., 1983, "Wave propagation in intense flux tubes", *Solar Phys.*, **87**, 77–93. [DOI], [ADS]

Roberts, B., 2000, “Waves and Oscillations in the Corona - (Invited Review)”, *Solar Phys.*, **193**, 139–152. [DOI], [ADS]

Rosenthal, C. S., Bogdan, T. J., Carlsson, M., Dorch, S. B. F., Hansteen, V., McIntosh, S. W., McMurry, A., Nordlund, Å. and Stein, R. F., 2002, “Waves in the Magnetized Solar Atmosphere. I. Basic Processes and Internetwork Oscillations”, *Astrophys. J.*, **564**, 508–524. [DOI], [ADS]

Rouppe van der Voort, L., Leenaarts, J., de Pontieu, B., Carlsson, M. and Vissers, G., 2009, “On-disk Counterparts of Type II Spicules in the Ca II 854.2 nm and H$\alpha$ Lines”, *Astrophys. J.*, **705**, 272–284. [DOI], [ADS], [arXiv:0909.2115 [astro-ph.SR]]

Rouppe van der Voort, L., De Pontieu, B., Pereira, T. M. D., Carlsson, M. and Hansteen, V., 2015, “Heating Signatures in the Disk Counterparts of Solar Spicules in Interface Region Imaging Spectrograph Observations”, *Astrophys. J. Lett.*, **799**, L3. [DOI], [ADS], [arXiv:1412.4531 [astro-ph.SR]]

Rudawy, P., Phillips, K. J. H., Buczylko, A., Williams, D. R. and Keenan, F. P., 2010, “Search for Rapid Changes in the Visible-Light Corona during the 21 June 2001 Total Solar Eclipse”, *Solar Phys.*, **267**, 305–327. [DOI], [ADS], [arXiv:1009.5205 [astro-ph.SR]]

Ruderman, M. S. and Roberts, B., 2002, “The Damping of Coronal Loop Oscillations”, *Astrophys. J.*, **577**, 475–486. [DOI], [ADS]

Rutten, R. J., 2012, “The quiet-Sun photosphere and chromosphere”, *Royal Society of London Philosophical Transactions Series A*, **370**, 3129–3150. [DOI], [ADS], [arXiv:1110.6606 [astro-ph.SR]]

Rušin, V. and Minarovjech, M., 1994, “Detection of small-scale dynamics in the emission corona.”, in *Solar Coronal Structures, IAU Colloq.* **144**, (Ed.) Rušin, V., Heinzel, P., Vial, J.-C., [ADS]

Saito, K., 1958, “Polar Rays of the Solar Corona”, *Pub. Astron. Soc. Japan*, **10**, 49. [ADS]

Saito, K., 1965, “Polar Rays of the Solar Corona, II.”, *Pub. Astron. Soc. Japan*, **17**, 1. [ADS]

Sakurai, T., Ichimoto, K., Raju, K. P. and Singh, J., 2002, “Spectroscopic Observation of Coronal Waves”, *Solar Phys.*, **209**, 265–286. [DOI], [ADS]

Samanta, T., Banerjee, D. and Tian, H., 2015a, “Quasi-periodic Oscillation of a Coronal Bright Point”, *Astrophys. J.*, **806**, 172. [DOI], [ADS], [arXiv:1505.00587 [astro-ph.SR]]

Samanta, T., Pant, V. and Banerjee, D., 2015b, “Propagating Disturbances in the Solar Corona and Spicular Connection”, *Astrophys. J. Lett.*, **815**, L16. [DOI], [ADS], [arXiv:1511.07354 [astro-ph.SR]]

Samanta, T., Henriques, V. M. J., Banerjee, D., Krishna Prasad, S., Mathioudakis, M., Jess, D. and Pant, V., 2016a, “The Effects of Transients on Photospheric and Chromospheric Power Distributions”, *Astrophys. J.*, **828**, 23. [DOI], [ADS], [arXiv:1604.06289 [astro-ph.SR]]

Samanta, T., Singh, J., Sindhuja, G. and Banerjee, D., 2016b, “Detection of High-Frequency Oscillations and Damping from Multi-slit Spectroscopic Observations of the Corona”, *Solar Phys.*, **291**, 155–174. [DOI], [ADS], [arXiv:1511.07160 [astro-ph.SR]]

Samanta, T., Tian, H., Banerjee, D. and Schanche, N., 2017, “Dynamics of subarcsecond bright dots in the transition region above sunspot and their relation to penumbral micro-jets”, *Astrophys. J. Lett.*, **835**, L19. [DOI], [ADS], [arXiv:1701.02531 [astro-ph.SR]]

Scharmer, G. B., 2006, “Comments on the optimization of high resolution Fabry-Pérot filtergraphs”, *Astron. Astrophys.*, **447**, 1111–1120. [DOI], [ADS]

Scharmer, G. B. and Henriques, V. M. J., 2012, “SST/CRISP observations of convective flows in a sunspot penumbra”, *Astron. Astrophys.*, **540**, A19. [DOI], [ADS], [arXiv:1109.1301 [astro-ph.SR]]

Scharmer, G. B., Bjelksjo, K., Korhonen, T. K., Lindberg, B. and Petterson, B., 2003a, “The 1-meter Swedish solar telescope”, in *Society of Photo-Optical Instrumentation Engineers (SPIE) Conference Series*, (Ed.) S. L. Keil & S. V. Avakyan, Society of Photo-Optical Instrumentation Engineers (SPIE) Conference Series, 4853, [ADS]

Scharmer, G. B., Dettori, P. M., Lofdahl, M. G. and Shand, M., 2003b, “Adaptive optics system for the new Swedish solar telescope”, in *Society of Photo-Optical Instrumentation Engineers (SPIE) Conference Series*, (Eds.) Keil, S. L., Avakyan, S. V., Society of Photo-Optical Instrumentation Engineers (SPIE) Conference Series, 4853, [ADS]

Scharmer, G. B., Narayan, G., Hillberg, T., de la Cruz Rodriguez, J., Löfdahl, M. G., Kiselman, D., Sütterlin, P., van Noort, M. and Lagg, A., 2008, “CRISP Spectropolarimetric Imaging of Penumbral Fine Structure”, *Astrophys. J. Lett.*, **689**, L69–L72. [DOI], [ADS], [arXiv:0806.1638]

Scharmer, G. B., Henriques, V. M. J., Kiselman, D. and de la Cruz Rodríguez, J., 2011, “Detection of Convective Downflows in a Sunspot Penumbra”, *Science*, **333**, 316. [DOI], [ADS]

Schou, J., Scherrer, P. H., Bush, R. I., Wachter, R., Couvidat, S., Rabello-Soares, M. C., Bogart, R. S., Hoeksema, J. T., Liu, Y., Duvall, T. L., Akin, D. J., Allard, B. A., Miles, J. W., Rairden, R., Shine, R. A., Tarbell, T. D., Title, A. M., Wolfson, C. J., Elmore, D. F., Norton, A. A. and Tomczyk, S., 2012, “Design and Ground Calibration of the Helioseismic and Magnetic Imager (HMI) Instrument on the Solar Dynamics Observatory (SDO)”, *Solar Phys.*, **275**, 229–259. [DOI], [ADS]

Schunker, H. and Cally, P. S., 2006, “Magnetic field inclination and atmospheric oscillations above solar active regions”, *Mon. Not. Roy. Astron. Soc.*, **372**, 551–564. [DOI], [ADS]

Sekse, D. H., Rouppe van der Voort, L. and De Pontieu, B., 2013, “On the Temporal Evolution of the Disk Counterpart of Type II Spicules in the Quiet Sun”, *Astrophys. J.*, **764**, 164. [DOI], [ADS], [arXiv:1212.4988 [astro-ph.SR]]

Sheeley, N. R. and Golub, L., 1979, “Rapid changes in the fine structure of a coronal 'bright point' and a small coronal 'active region'”, *Solar Phys.*, **63**, 119–126. [ADS]

Shine, R. A., Title, A. M., Tarbell, T. D., Smith, K., Frank, Z. A. and Scharmer, G., 1994, “High-resolution observations of the Evershed effect in sunspots”, *Astrophys. J.*, **430**, 413–424. [DOI], [ADS]

Singh, J., Cowsik, R., Raveendran, A. V., Bagare, S. P., Saxena, A. K., Sundararaman, K., Krishan, V., Naidu, N., Samson, J. P. A. and Gabriel, F., 1997, “Detection of Short-Period Coronal Oscillations during the Total Solar Eclipse of 24 October, 1995”, *Solar Phys.*, **170**, 235–252. [ADS]

Singh, J., Hasan, S. S., Gupta, G. R., Banerjee, D., Muneer, S., Raju, K. P., Bagare, S. P. and Srinivasan, R., 2009, “Intensity Oscillation in the Corona as Observed during the Total Solar Eclipse of 29 March 2006”, *Solar Phys.*, **260**, 125–134. [DOI], [ADS]

Singh, J., Hasan, S. S., Gupta, G. R., Nagaraju, K. and Banerjee, D., 2011, “Spectroscopic Observation of Oscillations in the Corona During the Total Solar Eclipse of 22 July 2009”, *Solar Phys.*, **270**, 213–233. [DOI], [ADS]

Skogsrud, H., Rouppe van der Voort, L., De Pontieu, B. and Pereira, T. M. D., 2015, “On the Temporal Evolution of Spicules Observed with IRIS, SDO, and Hinode”, *Astrophys. J.*, **806**, 170. [DOI], [ADS], [arXiv:1505.02525 [astro-ph.SR]]

Srivastava, A. K. and Dwivedi, B. N., 2010, "Observations from Hinode/EIS of intensity oscillations above a bright point: signature of the leakage of acoustic oscillations in the inner corona", *Mon. Not. Roy. Astron. Soc.*, **405**, 2317–2326. [DOI], [ADS]

Strong, K. T., Harvey, K., Hirayama, T., Nitta, N., Shimizu, T. and Tsuneta, S., 1992, "Observations of the variability of coronal bright points by the Soft X-ray Telescope on YOHKOH", *Pub. Astron. Soc. Japan*, **44**, L161–L166. [ADS]

Su, J. T., 2014, "Statistical Detection of Slow-mode Waves in Solar Polar Regions with SDO/AIA", *Astrophys. J.*, **793**, 117. [DOI], [ADS]

Teriaca, L., Banerjee, D., Falchi, A., Doyle, J. G. and Madjarska, M. S., 2004, "Transition region small-scale dynamics as seen by SUMER on SOHO", *Astron. Astrophys.*, **427**, 1065–1074. [DOI], [ADS]

Tian, H., Curdt, W., Marsch, E. and He, J., 2008a, "Cool and Hot Components of a Coronal Bright Point", *Astrophys. J. Lett.*, **681**, L121–L124. [DOI], [ADS], [arXiv:0906.3005 [astro-ph.SR]]

Tian, H., Xia, L.-D. and Li, S., 2008b, "Long-period oscillations in solar coronal bright points", *Astron. Astrophys.*, **489**, 741–745. [DOI], [ADS]

Tian, H., McIntosh, S. W. and De Pontieu, B., 2011a, "The Spectroscopic Signature of Quasi-periodic Upflows in Active Region Timeseries", *Astrophys. J. Lett.*, **727**, L37. [DOI], [ADS], [arXiv:1012.5112 [astro-ph.SR]]

Tian, H., McIntosh, S. W., De Pontieu, B., Martínez-Sykora, J., Sechler, M. and Wang, X., 2011b, "Two Components of the Solar Coronal Emission Revealed by Extreme-ultraviolet Spectroscopic Observations", *Astrophys. J.*, **738**, 18. [DOI], [ADS], [arXiv:1106.1141 [astro-ph.SR]]

Tian, H., McIntosh, S. W., Habbal, S. R. and He, J., 2011c, "Observation of High-speed Outflow on Plume-like Structures of the Quiet Sun and Coronal Holes with Solar Dynamics Observatory/Atmospheric Imaging Assembly", *Astrophys. J.*, **736**, 130. [DOI], [ADS], [arXiv:1105.3119 [astro-ph.SR]]

Tian, H., McIntosh, S. W., Wang, T., Ofman, L., De Pontieu, B., Innes, D. E. and Peter, H., 2012, "Persistent Doppler Shift Oscillations Observed with Hinode/EIS in the Solar Corona: Spectroscopic Signatures of Alfvénic Waves and Recurring Upflows", *Astrophys. J.*, **759**, 144. [DOI], [ADS], [arXiv:1209.5286 [astro-ph.SR]]

Tian, H., DeLuca, E. E., Cranmer, S. R., De Pontieu, B., Peter, H., Martínez-Sykora, J., Golub, L., McKillop, S., Reeves, K. K., Miralles, M. P., McCauley, P., Saar, S., Testa, P., Weber, M., Murphy, N., Lemen, J., Title, A., Boerner, P., Hurlburt, N., Tarbell, T. D., Wuelser, J. P., Kleint, L., Kankelborg, C., Jaeggli, S., Carlsson, M., Hansteen, V. and McIntosh, S. W., 2014a, "Prevalence of small-scale jets from the networks of the solar transition region and chromosphere", *Science*, **346**(27), 1255711. [DOI], [ADS], [arXiv:1410.6143 [astro-ph.SR]]

Tian, H., Kleint, L., Peter, H., Weber, M., Testa, P., DeLuca, E., Golub, L. and Schanche, N., 2014b, "Observations of Subarcsecond Bright Dots in the Transition Region above Sunspots with the Interface Region Imaging Spectrograph", *Astrophys. J. Lett.*, **790**, L29. [DOI], [ADS], [arXiv:1407.1060 [astro-ph.SR]]

Tiwari, S. K., van Noort, M., Lagg, A. and Solanki, S. K., 2013, "Structure of sunspot penumbral filaments: a remarkable uniformity of properties", *Astron. Astrophys.*, **557**, A25. [DOI], [ADS], [arXiv:1307.3668 [astro-ph.SR]]

Tiwari, S. K., van Noort, M., Solanki, S. K. and Lagg, A., 2015, "Depth-dependent global properties of a sunspot observed by Hinode using the Solar Optical Telescope/Spectropolarimeter", *Astron. Astrophys.*, **583**, A119. [DOI], [ADS], [arXiv:1508.04830 [astro-ph.SR]]

Tiwari, S. K., Moore, R. L., Winebarger, A. R. and Alpert, S. E., 2016, "Transition-region/Coronal Signatures and Magnetic Setting of Sunspot Penumbral Jets: Hinode (SOT/FG), Hi-C, and SDO/AIA Observations", *Astrophys. J.*, **816**, 92. [DOI], [ADS], [arXiv:1511.07900 [astro-ph.SR]]

Torrence, Christopher and Compo, Gilbert P., 1998, "A Practical Guide to Wavelet Analysis", *Bulletin of the American Meteorological Society*, **79**, 61–78

Tsiropoula, G. and Schmieder, B., 1997, "Determination of physical parameters in dark mottles.", *Astron. Astrophys.*, **324**, 1183–1189. [ADS]

Tsiropoula, G., Alissandrakis, C. E. and Schmieder, B., 1994a, "Time evolution of fine structures in the solar chromosphere.", *Astron. Astrophys.*, **290**, 285–294. [ADS]

Tsiropoula, G., Schmieder, B. and Alissandrakis, C. E., 1994b, "Dynamical fine structures of the chromosphere", *Space Sci. Rev.*, **70**, 65–68. [DOI], [ADS]

Tsiropoula, G., Tziotziou, K., Schwartz, P. and Heinzel, P., 2009, "Multiwavelength analysis of a solar quiet region", *Astron. Astrophys.*, **493**, 217–225. [DOI], [ADS]

Tsiropoula, G., Tziotziou, K., Kontogiannis, I., Madjarska, M. S., Doyle, J. G. and Suematsu, Y., 2012, "Solar Fine-Scale Structures. I. Spicules and Other Small-Scale, Jet-Like Events at the Chromospheric Level: Observations and Physical Parameters", *Space Sci. Rev.*, **169**, 181–244. [DOI], [ADS], [arXiv:1207.3956 [astro-ph.SR]]

Tsubaki, T., 1977, "Periodic oscillations found in coronal velocity fields", *Solar Phys.*, **51**, 121–130. [DOI], [ADS]

Tsuneta, S., Ichimoto, K., Katsukawa, Y., Nagata, S., Otsubo, M., Shimizu, T., Suematsu, Y., Nakagiri, M., Noguchi, M., Tarbell, T., Title, A., Shine, R., Rosenberg, W., Hoffmann, C., Jurcevich, B., Kushner, G., Levay, M., Lites, B., Elmore, D., Matsushita, T., Kawaguchi, N., Saito, H., Mikami, I., Hill, L. D.

and Owens, J. K., 2008, "The Solar Optical Telescope for the Hinode Mission: An Overview", *Solar Phys.*, **249**, 167–196. [DOI], [ADS], [arXiv:0711.1715]

Tziotziou, K., Tsiropoula, G. and Mein, P., 2003, "On the nature of the chromospheric fine structure. I. Dynamics of dark mottles and grains", *Astron. Astrophys.*, **402**, 361–372. [DOI], [ADS]

Ugarte-Urra, I., Doyle, J. G., Madjarska, M. S. and O'Shea, E., 2004, "Signature of oscillations in coronal bright points", *Astron. Astrophys.*, **418**, 313–324. [DOI], [ADS]

Uitenbroek, H., 2003, "The Accuracy of the Center-of-Gravity Method for Measuring Velocity and Magnetic Field Strength in the Solar Photosphere", *Astrophys. J.*, **592**, 1225–1233. [DOI], [ADS]

Vaiana, G. S., Davis, J. M., Giacconi, R., Krieger, A. S., Silk, J. K., Timothy, A. F. and Zombeck, M., 1973, "X-Ray Observations of Characteristic Structures and Time Variations from the Solar Corona: Preliminary Results from SKYLAB", *Astrophys. J. Lett.*, **185**, L47. [DOI], [ADS]

van de Hulst, H. C., 1950, "On the polar rays of the corona (Errata: 11 VIII)", *Bulletin of the Astronomical Institutes of the Netherlands*, **11**, 150. [ADS]

Van Doorsselaere, T., Nakariakov, V. M. and Verwichte, E., 2008, "Detection of Waves in the Solar Corona: Kink or Alfvén?", *Astrophys. J. Lett.*, **676**, L73–L75. [DOI], [ADS]

van Noort, M., Rouppe van der Voort, L. and Löfdahl, M. G., 2005, "Solar Image Restoration By Use Of Multi-frame Blind De-convolution With Multiple Objects And Phase Diversity", *Solar Phys.*, **228**, 191–215. [DOI], [ADS]

Vecchio, A., Cauzzi, G., Reardon, K. P., Janssen, K. and Rimmele, T., 2007, "Solar atmospheric oscillations and the chromospheric magnetic topology", *Astron. Astrophys.*, **461**, L1–L4. [DOI], [ADS], [astro-ph/0611206]

Vernazza, J. E., Avrett, E. H. and Loeser, R., 1981, "Structure of the solar chromosphere. III - Models of the EUV brightness components of the quiet-sun", *Astrophys. J. Suppl.*, **45**, 635–725. [DOI], [ADS]

Verwichte, E., Marsh, M., Foullon, C., Van Doorsselaere, T., De Moortel, I., Hood, A. W. and Nakariakov, V. M., 2010, "Periodic Spectral Line Asymmetries in Solar Coronal Structures from Slow Magnetoacoustic Waves", *Astrophys. J. Lett.*, **724**, L194–L198. [DOI], [ADS]

Verwichte, E., Van Doorsselaere, T., White, R. S. and Antolin, P., 2013, "Statistical seismology of transverse waves in the solar corona", *Astron. Astrophys.*, **552**, A138. [DOI], [ADS]

Vissers, G. J. M., Rouppe van der Voort, L. H. M. and Carlsson, M., 2015, "Evidence for a Transition Region Response to Penumbral Microjets in Sunspots", *Astrophys. J. Lett.*, **811**, L33. [DOI], [ADS], [arXiv:1509.01402 [astro-ph.SR]]

Voulgaris, A. G., Gaintatzis, P. S., Seiradakis, J. H., Pasachoff, J. M. and Economou, T. E., 2012, "Spectroscopic Coronal Observations During the Total Solar Eclipse of 11 July 2010", *Solar Phys.*, **278**, 187–202. [DOI], [ADS], [arXiv:1202.1535 [astro-ph.SR]]

Wang, J. and Shi, Z., 1993, "The flare-associated magnetic changes in an active region. II - Flux emergence and cancellation", *Solar Phys.*, **143**, 119–139. [DOI], [ADS]

Wang, T., 2011, "Standing Slow-Mode Waves in Hot Coronal Loops: Observations, Modeling, and Coronal Seismology", *Space Sci. Rev.*, **158**, 397–419. [DOI], [ADS], [arXiv:1011.2483 [astro-ph.SR]]

Wang, T. J. and Solanki, S. K., 2004, "Vertical oscillations of a coronal loop observed by TRACE", *Astron. Astrophys.*, **421**, L33–L36. [DOI], [ADS]

Williams, D. R., Phillips, K. J. H., Rudawy, P., Mathioudakis, M., Gallagher, P. T., O'Shea, E., Keenan, F. P., Read, P. and Rompolt, B., 2001, "High-frequency oscillations in a solar active region coronal loop", *Mon. Not. Roy. Astron. Soc.*, **326**, 428–436. [DOI], [ADS]

Williams, D. R., Mathioudakis, M., Gallagher, P. T., Phillips, K. J. H., McAteer, R. T. J., Keenan, F. P., Rudawy, P. and Katsiyannis, A. C., 2002, "An observational study of a magneto-acoustic wave in the solar corona", *Mon. Not. Roy. Astron. Soc.*, **336**, 747–752. [DOI], [ADS]

Winebarger, A. R., Walsh, R. W., Moore, R., De Pontieu, B., Hansteen, V., Cirtain, J., Golub, L., Kobayashi, K., Korreck, K., DeForest, C., Weber, M., Title, A. and Kuzin, S., 2013, "Detecting Nanoflare Heating Events in Subarcsecond Inter-moss Loops Using Hi-C", *Astrophys. J.*, **771**, 21. [DOI], [ADS]

Zaqarashvili, T. V. and Erdélyi, R., 2009, "Oscillations and Waves in Solar Spicules", *Space Sci. Rev.*, **149**, 355–388. [DOI], [ADS], [arXiv:0906.1783 [astro-ph.SR]]

Zhang, J., Kundu, M. R. and White, S. M., 2001, "Spatial Distribution and Temporal Evolution of Coronal Bright Points", *Solar Phys.*, **198**, 347–365. [DOI], [ADS]

Zhang, Q. M., Chen, P. F., Guo, Y., Fang, C. and Ding, M. D., 2012, "Two Types of Magnetic Reconnection in Coronal Bright Points and the Corresponding Magnetic Configuration", *Astrophys. J.*, **746**, 19. [DOI], [ADS]

Zhang, Q. M., Chen, P. F., Ding, M. D. and Ji, H. S., 2014, "Reciprocatory magnetic reconnection in a coronal bright point", *Astron. Astrophys.*, **568**, A30. [DOI], [ADS], [arXiv:1406.5328 [astro-ph.SR]]